

# **Determination of the Electron Energy Distribution Function of a Low Temperature Plasma from Optical Emission Spectroscopy**

Inauguraldissertation

zur

Erlangung des akademischen Grades

doctor rerum naturalium (Dr. rer. nat.)

an der Mathematisch-Naturwissenschaftlichen Fakultät

der

Ernst-Moritz-Arndt-Universität Greifswald

vorgelegt von  
Dirk Hilar Dodt  
geboren am  
2.3.1979  
in Iserlohn

Greifswald, den 5.1.2009



Dekan: Prof. Dr. Klaus Fesser

1. Gutachter: PD Dr. Dinklage

2. Gutachter: Prof. Dr. Soltwisch

Tag der Promotion: 17.4.2009



# Contents

<b>1. Introduction</b>	<b>1</b>
1.1. Motivation and Scope of Work . . . . .	1
1.2. Existing Approaches for the Interpretation of Spectroscopic Data . . . . .	2
1.3. Proof of Principle using a Stable dc Discharge in Neon . . . . .	2
<b>2. Low Temperature Plasmas</b>	<b>3</b>
2.1. Introduction . . . . .	3
2.1.1. Plasma Physics . . . . .	3
2.1.2. A Brief History of Plasma Physics . . . . .	3
2.1.3. Characteristical Parameters of Plasmas . . . . .	4
2.1.4. Kinetic Description of Plasmas . . . . .	5
2.1.5. Electron Energy Distribution Functions . . . . .	8
2.2. Properties of Glow Discharges . . . . .	8
2.2.1. Qualitative Picture of Processes in Gas Discharges . . . . .	9
Similarity Laws . . . . .	10
Elementary Processes . . . . .	10
Radiation Transport . . . . .	12
2.2.2. Kinetic Modelling of Gas Discharges . . . . .	13
2.2.3. Electronic Excitation . . . . .	15
2.2.4. Resonance Radiation . . . . .	15
2.3. Determination of Excitation Cross-Sections . . . . .	15
2.3.1. Theoretical Calculations of Cross-Sections . . . . .	15
The Scattering Problem, Scattering Amplitude and Cross-Section . . . . .	16
Born Series . . . . .	17
Distorted-Wave Method . . . . .	18
The Close Coupling Expansion . . . . .	19
2.3.2. Rates of Direct and Reverse Processes . . . . .	20
2.4. Atomic physics in the Discharge in Neon . . . . .	20
2.4.1. Notation of the Excited States. . . . .	21
<b>3. Concepts of Probabilistic Data Analysis</b>	<b>23</b>
3.1. Probability Theory . . . . .	23
3.1.1. Plausible Reasoning and Data Analysis . . . . .	24
3.1.2. Likelihood . . . . .	25
3.1.3. Updating Plausibilities: Prior and Posterior . . . . .	26
3.1.4. Marginalization . . . . .	26
3.1.5. Entropy and the Maximum Entropy Principle . . . . .	27
3.1.6. Maximum Entropy Priors . . . . .	28
3.1.7. The Implementation of a Data Analysis . . . . .	29

3.1.8.	Monte Carlo methods . . . . .	30
	Markov Chain Monte Carlo Methods . . . . .	32
	The Metropolis Hastings Algorithm . . . . .	33
	Convergence of Markov Chain Monte-Carlo . . . . .	34
<b>4.</b>	<b>Experiment</b>	<b>37</b>
4.1.	Setup . . . . .	37
4.1.1.	Optical Setup . . . . .	37
4.1.2.	Spectrometer . . . . .	37
4.2.	Calibration with the Standard Light Source . . . . .	38
4.2.1.	Uncertainty of the Spectral Measurement . . . . .	38
<b>5.</b>	<b>Data Model</b>	<b>41</b>
5.1.	Overview . . . . .	41
5.2.	Collisional Radiative Model of the Neon Discharge . . . . .	42
5.3.	Spatial Dependence of the Plasma Model . . . . .	43
5.3.1.	Coordinate System . . . . .	43
5.3.2.	Line Averaging of the EEDF . . . . .	44
5.4.	Parameterizations of the EEDF . . . . .	45
5.5.	Optical Depth of Resonance Transitions . . . . .	45
5.6.	Optical Depth of Transitions to Metastable States. . . . .	47
5.7.	Line-of-Sight Integration. . . . .	49
5.8.	Apparatus Function . . . . .	50
	Determination of the Apparatus function . . . . .	50
5.9.	Calibration of the Spectrometer. . . . .	53
<b>6.</b>	<b>Analysis of Spectroscopic Data</b>	<b>55</b>
6.1.	Problem Statement . . . . .	55
6.2.	Likelihood . . . . .	55
	Effective Width of the Likelihood $\sigma_{\text{eff},i}$ . . . . .	55
6.3.	Priors . . . . .	55
6.3.1.	Parameters of interest . . . . .	56
6.3.2.	Atomic Data . . . . .	56
6.3.3.	Escape Factors to Metastable States . . . . .	57
6.3.4.	Population Densities of Unmodeled Levels . . . . .	58
6.3.5.	Prior Distributions of the Radial Profile Integrals . . . . .	58
6.3.6.	Priors of the Wavelength Calibration . . . . .	58
6.3.7.	Priors of the Absolute Intensity Calibration . . . . .	58
6.3.8.	Priors of the Apparatus Function . . . . .	59
6.4.	Focusing: Marginal Posterior Probability Distributions . . . . .	59
<b>7.</b>	<b>Results</b>	<b>61</b>
7.1.	Validation of the Data Analysis Procedure . . . . .	61
7.1.1.	Result of the Forward Model . . . . .	63
7.1.2.	Reconstruction of Simulated Spectral Data . . . . .	63
	Validation of Atomic Data . . . . .	65
	Discussion . . . . .	67
7.1.3.	Robustness of Reconstruction Against Different Model-Assumptions . . . . .	70

7.1.4.	Convergence of the Monte-Carlo Sampling . . . . .	73
7.1.5.	Influence of the Parameterization of the EEDF . . . . .	77
	Energy Dependence of the Elementary Processes. . . . .	80
7.2.	Results Obtained from the Emission Spectra of the Neon Discharge . . . . .	81
7.2.1.	Reconstruction of the EEDF . . . . .	81
	Axially Resolved Measurements . . . . .	83
	Anode . . . . .	84
	Cathode . . . . .	87
7.2.2.	Validation of Atomic Data . . . . .	89
	Influence of Continuum-Coupling . . . . .	90
	Einstein Coefficients . . . . .	92
<b>8.</b>	<b>Summary</b>	<b>97</b>
<b>A.</b>	<b>Uncertainty of Transfer Function</b>	<b>101</b>
	Data Model . . . . .	101
	Likelihood . . . . .	101
	Priors . . . . .	101
	Posterior . . . . .	101
	Summary . . . . .	102
<b>B.</b>	<b>Autocorrelation</b>	<b>103</b>
	B.1. Non-Linear Least Squares Fit of the Autocorrelation Function . . . . .	103
<b>C.</b>	<b>Refraction in the Glass Tube</b>	<b>105</b>
	C.1. Formulae for the Line-of-Sight Integration . . . . .	106
<b>D.</b>	<b>Additional Figures</b>	<b>109</b>
<b>E.</b>	<b>Labelling of Neon States</b>	<b>115</b>
	<b>Bibliography</b>	<b>117</b>
<b>F.</b>	<b>Curriculum Vitae</b>	<b>123</b>
<b>G.</b>	<b>Publication List</b>	<b>125</b>





# 1. Introduction

## 1.1. Motivation and Scope of Work

Low temperature plasmas are nowadays a well established tool with a diverse field of technical applications. Beyond the already traditional usage for the purpose of lighting, as active media in lasers, for plasma cutting and welding, and as electrical conductor, new applications can be found like anisotropic etching, large scale plasma displays, or the field of surface modification in industrial production. The control and optimization of low temperature plasmas is a field of ongoing research. New methods for the characterization of low temperature plasmas, allowing feedback for the control of plasmas and the comparison to theoretical models are strongly desirable.

In physical research, dc gas discharges serve as a non-equilibrium kinetic system, which is well reproducible and easy to handle. Discharges are used, e.g. to study the physics of phase transitions or the evolution of chaotic behavior. The investigations of simply structured glow discharges allow to gain insights into the physical processes in low temperature plasmas, which form the necessary basis for future exploration of processes in complex plasmas. As a consequence, the properties of glow discharges and their experimental operation are well documented in literature, enabling the validation of results obtained with new methods.

The electron energy distribution function (EEDF) plays a major role in the characterization of low-temperature plasmas. It reflects the balance between the heating and the release of energy in form of heat, light or fast particles. Therefore knowledge about the EEDF is desired in many of the practical applications mentioned above. Conventionally the EEDF is usually obtained by measuring the current voltage characteristic of an electrical probe in contact with the plasma. In the present work, a spectroscopic approach for the determination of the EEDF is demonstrated. This non-invasive approach offers an interesting alternative to probe-measurements. It can be applied in the presence of magnetic fields and strong gradients of the plasma parameters. In contrast to probe measurements it doesn't suffer from degradation by reactive plasmas and does not disturb the plasma under investigation. Other optical methods for the measurement of the EEDF, like Thomson scattering of irradiated laser light, need high experimental effort, especially for low electron densities. In comparison, the experimental setup for emission spectroscopy is simple and cheap. The measurements for the present work were performed using a simple overview spectrometer, which is commercially available.

The interpretation of the spectroscopic data requires a detailed modelling of the elementary processes in the plasma and the spectroscopic measurement. A large number of cross-sections, lifetimes of excited states and branching ratios is needed to accomplish this. Advances in the availability of these data, provided by the numerical solution of quantum mechanical models of the atoms and ions in the plasma, open up new possibilities in the interpretation of spectroscopic data. The aim of the present work is to show the potential of the currently available data in combination with with state-of-the-art probabilistic data analysis method<sup>1,2</sup>. The probabilistic approach is needed for a consistent interpretation in the presence of deviations between model and the measured data, which are the effect of unavoidable inaccuracies in the large set of input quantities.

## 1.2. Existing Approaches for the Interpretation of Spectroscopic Data

The idea to use emission spectroscopy for the determination of the EEDF was brought up long ago<sup>3</sup>. First attempts to use spectroscopy are based on line-ratio techniques, consisting of a mapping of the intensities of different spectral lines onto electron temperature and density<sup>4</sup>. Ideally, line-ratio techniques require a monotonic relation between the desired parameters of the EEDF and the used line-ratios. This is not necessarily fulfilled for all plasma conditions. The present approach is based on a method described by Fischer and Dose<sup>5</sup>, where a collisional-radiative model (CRM) is used to relate a set of line intensities directly to the EEDF. In the present work, the model for the spectroscopic data was extended to a direct modeling of the full spectrum, rather than the analysis of derived line intensities. The use of the full spectrum allows to employ sophisticated parameterizations of the EEDF, and is not limited to the reconstruction of a small number of parameters ( $N_e$ ,  $T_e$ ).

## 1.3. Proof of Principle using a Stable dc Discharge in Neon

The reconstruction of the EEDF is demonstrated using a using a cylindrical dc discharge in neon. The neon discharge is a well-examined physical system (see e.g.<sup>6-14</sup> and references therein for a small selection) with a high reproducibility, thereby allowing for the comparison of equivalent discharges with the same geometrical parameters, gas pressure, and electrical circuit. Consequently, the EEDF obtained for the positive column and the anode region of the discharge could readily be compared to results from literature. For the EEDF in the more complex and strongly inhomogeneous region near the cathode, however, no results from kinetic modelling were available for a direct validation.

## 2. Low Temperature Plasmas

### 2.1. Introduction

The aspects of low temperature plasma physics described in the following chapter define the context and perspective of the spectroscopic approach to the electron kinetics. Comprehensive introductions to plasma physics and its branches can be found in many textbooks e.g. in Refs. (<sup>15-17</sup>). In order to give the background for the concept the electron energy distribution function, main aspects of electron kinetics in ionized gases and related elementary processes are described.

#### 2.1.1. Plasma Physics

A plasma is a quasi-neutral many-particle system of free electrons, ions and neutrals. It is sometimes referred to as the fourth state of matter beside the solid-, liquid-, and gaseous state. In contrast to these three ordinary states, the transition to a plasma is not a phase transition in the thermodynamic sense. The ionization increases gradually when more energy is coupled to the system. A plasma can be created by heating a material until the thermal energy of the particles leads to ionization of the gas. In typical laboratory or technical applications, however, the ionization is mostly achieved by strong (direct or alternating current) electrical fields. The plasma state of matter is associated with a number of characteristic properties, which are either connected to the high particle temperatures ( $\mathcal{O}(\text{eV})$  or greater) or are caused by the existence of free charge carriers, causing a high electrical conductivity and giving rise to collective effects, such as wave phenomena.

#### 2.1.2. A Brief History of Plasma Physics

The term plasma was introduced by Langmuir (1929)<sup>18</sup>, who was investigating the properties of low pressure mercury discharges. He identified the free electrons and ions in the neutral background gas as an analogy to the red and white blood corpuscles in the blood plasma.

The first observations of ionization effects in air date back to as long as the late 16th century when the charging of an electroscope through a flame was observed by Gilbert (1544-1603), the personal physician of the English Queen Elisabeth<sup>16</sup>. The electrical conductivity of air was shown by Coulomb (1736-1806) and attributed to the radioactivity of the environment by Elster (1854-1920) and Geitel (1855-1923). The first efficient electrostatic generator allowing to artificially produce spark overs was built by Otto von Guericke (1602-1686). In 1803 Petroff used a Voltaic battery with around 1000 (!) cells to be able to create electrical arc-discharges in air, a light source with until then unknown luminosity. Faraday (1791-1867) investigated the flow of electrical current through evacuated glass tubes and discovered the glow discharge in 1831. From the middle of the 19th to the early 20th century many prominent physicists engaged in research on electric discharges in gases and cathode ray tubes in general<sup>19</sup>, the discovery of the free electron by Thomson, Townsend and Wilson in 1897<sup>20</sup> is an important result of that era. Up to around the year 1950 the interest in plasma physics was mainly driven by the investigation of astronomical and geophysical phenomena (postulation of the Alfvén wave 1942). In the early 1950s intensive work

**Table 2.1.:** Some applications of plasmas in technological applications

---

plasma propulsion devices	First proposed around 1920.
magneto-hydrodynamic generator	First funded research in 1938.
thermionic converter	Used in atomic batteries as energy source in space flight.
glow discharges in lasers	Leading to a revive of glow discharge physics.
fluorescent lamps	First applications of mercury vapor lamps in the 1930s.
electrical circuit elements	For example thyratrons, spark gaps, high voltages switches and more.
plasma processing, etching	In the second half of the 20th century plasma processing has become a growing field with diverse applications.

---

was begun on the realization of a device for controlled nuclear fusion This brought plasma physics to wider attention. In the course of the last century a number of technological applications for plasmas were invented, In table 2.1 an illustrative, non-exhaustive list of some envisaged or realized examples is given. Also, as in many fields, the advancement in the availability of computational resources allowed the solution of long well-known basic equations for increasingly realistic, complex boundary conditions providing the means for the simulation of systems of practical interest and triggering the development of new ideas<sup>?</sup> .

### 2.1.3. Characteristical Parameters of Plasmas

Unlike the three ordinary states of matter (solid, liquid and gaseous), plasmas exist in a wide range of temperatures (if well defined at all) and densities, giving rise to vastly differing physical properties and a variety of observed phenomena. In addition, the properties of the plasma may depend on other external parameters like strength of electromagnetic fields used to create or confine the plasma, or the degree of ionization of plasma<sup>21</sup>.

There exist different criteria for the classification of plasmas according either to the parameters important for their description or according to the occurrence of certain physical effects. The most important criteria are:

**temperature** Plasmas are broadly categorized in *low* and *high* temperature plasmas, when speaking of technical applications, the latter basically consisting of fusion plasmas, while the former consist of everything else.

**thermality** According to whether the different components (electrons, ions, neutrals) of the plasma are in thermal equilibrium with each other, *thermal* and *non-thermal* plasmas are distin-

guished. As the electrons typically absorb most of the heating power used to sustain the plasma their temperature can be much higher ( $\mathcal{O}(1 \text{ eV})$ ) than that of the other particles.

**plasma parameter** The plasma parameter  $\Gamma$  is a dimensionless number, given the ratio of thermal and electrostatic energy

$$\Gamma = \frac{e^2}{4\pi\epsilon_0 a} \frac{1}{k_B T} \quad (2.1)$$

( $e$ : elementary charge,  $\epsilon_0$ : electric constant,  $k_B$ : Boltzmann constant,  $T$ : temperature,  $a = (4\pi n/3)^{-1/3}$ : Wigner-Seitz radius (mean particle distance)).

Strongly coupled plasmas, which are typically in thermal equilibrium, are characterized by  $\Gamma \gg 1$ . The plasma is said to be ideal, when the plasma parameter is small ( $\Gamma \ll 1$ ). In that case, the particles only interact with a smooth background field determined by the collective effect of the other particles, rather than through pairwise interactions (collisions) and a kinetic description is valid (cf. 2.1.4).

**degree of ionization** The particle densities of ions and neutrals determine the degree of ionization of a plasma. In thermodynamic equilibrium, the Saha equation is used to determine the degree of ionization which reads for the first (positive) ionization stage:

$$\frac{n_+ n_e}{n_0} = \frac{g_+}{g_0} \frac{2(2\pi m_e k_B T_e)^{(3/2)}}{h^3} \exp\left(-\frac{\chi}{k_B T_e}\right). \quad (2.2)$$

( $n$ : densities,  $g$ : statistical weights.  $m_e$ : electron mass,  $k_B$ : Boltzmann's constant,  $T_e$ : electron temperature,  $h$ : Planck's constant,  $\chi$ : ionization potential)

Since the degree of ionization is a continuous function in the electron temperature at given densities, the gas-plasma transition is continuous as well. Therefore, this transition is not a phase transition in its thermodynamic sense. The plasmas in glow discharges investigated here have a low degree of ionization  $\sim 10^{-4} \dots 10^{-8}$ .

**further effects and limitations** Relativistic effects limit the classical description of plasmas in temperature and density, i.e. when the thermal energy or the Fermi energy approaches the mass equivalent of electrons, respectively. These plasmas are called *relativistic plasmas* or *relativistically degenerated*, respectively. In the work we are far below these limits. Magnetic fields, both self generated and externally applied, play an important role for laboratory plasmas. However, the magnetic effects are negligible in the case investigated here.

The neon dc-discharge which was used to prove the applicability of the present diagnostic approach is an example for a *weakly-coupled, non-thermal, low-temperature* plasma. During the reconstruction procedure the intensity of lines in the emission spectrum is related to population densities of excited states of neon atoms. This is only possible in plasmas with a temperature low enough for a significant fraction of the atoms to be not (fully) ionized. The distribution functions of the constituents of a thermal plasma have a Maxwellian form and their temperature can directly be obtained from the Maximum of the black-body emission spectrum.

#### 2.1.4. Kinetic Description of Plasmas

The term *kinetic theory* was first used in the context of Maxwell's work<sup>22</sup>, which was continuing the development of the ideas of Bernoulli, Joule, Clausius and others during the second half of the

19th century. Kinetic theory explains macroscopic properties of gases, like its pressure or temperature, by the dynamics of the molecules, rather than their static repulsion. Maxwell's achievements were generalized by Boltzmann who formulated the basic equation of kinetic theory, which still holds in its original form, although more rigorous derivations are available today<sup>23</sup>.

Once kinetic theory was established, the application of its ideas to the case of ionized gases was natural<sup>24</sup>. It was recognized experimentally<sup>25</sup>, that the electrons and ions in a plasma can frequently be approximately described using the Maxwellian velocity distribution derived in the kinetic theory of neutral gases under the assumption of local thermal equilibrium.

The basis for the kinetic description of a many-particle system is the velocity distribution function  $f(\vec{x}, \vec{v}, t)$ , which quantifies the number of particles in the volume element of phase space  $[(\vec{x}, \vec{v}), (\vec{x} + d\vec{x}, \vec{v} + d\vec{v})]$  at time  $t$ . This is an effectively simplified description, whose feasibility was recognized early, and which can also be derived more rigorously<sup>23</sup>. The microscopic information which is not contained in  $f(\vec{x}, \vec{v}, t)$  is the *relative* location and velocity of the particle on small length- and time-scales, the small scale *correlations*. The validity of a dynamical theory for the many-particle system based on  $f(\vec{x}, \vec{v}, t)$  is based on a number of assumptions listed e.g. in Ref (23). Among these assumptions, the *smallness of the influence of collisions* is one which requires special attention: It allows to treat collisions as a correction to the collision-less case, considering only pair-wise or possibly three-body interactions. It is interesting to note, that this approximation is fulfilled in a plasma and in a neutral gas for completely different reasons. In a neutral gas, the range of the inter-particle (Van-der-Waals) force is small compared to the average particle distance and collective interactions between more than two particles can be neglected. In a plasma, on the contrary, the range  $r_0 = \lambda_D$  of the electromagnetic force between the charged particles is typically much *greater*\* than the average particle distance  $n^{-1/3}$ . In this case the interactions with the cloud of particles in the Debye-sphere dominate over binary collisions and the plasma particles can be treated as if they only interact with a smooth background field, treating collisions as a small correction, again.

The statistical state of a system of  $N$  particles is in a complete - though in an intractably complex - way described by the distribution function  $F_N$  in  $6N$ -dimensional phase space, which is spanned by the coordinates and velocities of all individual particles:

$$F_N(\vec{x}_1, \vec{x}_2, \dots, \vec{x}_N, \vec{v}_1, \vec{v}_2, \dots, \vec{v}_N, t). \quad (2.3)$$

Reduced  $i$ -particle distribution functions  $F_i(\vec{x}_1, \vec{x}_2, \dots, \vec{x}_i, \vec{v}_1, \vec{v}_2, \dots, \vec{v}_i, t)$  can be obtained by averaging over the phase space coordinates of particles  $(i+1) \dots N$ :

$$F_i(\vec{x}_1, \vec{x}_2, \dots, \vec{x}_i, \vec{v}_1, \vec{v}_2, \dots, \vec{v}_i, t) = \int d\vec{x}_{i+1} \dots d\vec{x}_N d\vec{v}_{i+1} \dots d\vec{v}_N F_N(\vec{x}_1, \vec{x}_2, \dots, \vec{x}_N, \vec{v}_1, \vec{v}_2, \dots, \vec{v}_N, t). \quad (2.4)$$

These allow a simplified description of the system. When the coupling between the different particles is weak, it is possible to describe the system by considering only one- and two-particle distribution functions. The two-particle distribution function describes the effect of two-body interactions while the one-particle distribution function completely neglects all microscopic correlations between the particles.

The time evolution of  $F_N$  is given by the Liouville equation from classical mechanics, when all external and inter-particle forces are known. By sequential averaging over the particle coordinates,

---

\*This depends on the density and temperature regime of the plasma, there exist also plasmas, where the number interacting particles is low, allowing a kinetic treatment analogously to the neutral gas case. In the intermediate regime, where there is no small parameter allowing to terminate the BBGKY hierarchy, kinetic theory cannot be applied.

the BBGKY hierarchy of equations for the reduced particle distribution functions is obtained from the Liouville equation. The BBGKY hierarchy has the property, that each reduced  $i$ -particle distribution function depends on the distribution function of next higher order. It can be terminated for some order  $j$ , when the  $f_j$  can be expressed in terms of distribution functions of lower order than  $j$  and the obtained equations that form a closed system are called kinetic equations<sup>23</sup>. As mentioned, the termination of the BBGKY hierarchy is possible when the coupling between the particles is weak and correlation- (=collision-) effects can be treated as correction to the collision-less case. Accordingly, the equations for the one-particle distribution function of the known sets of kinetic equations are of the form

$$\frac{df}{dt} = \frac{\partial f}{\partial t} + \vec{v} \cdot \vec{\nabla} f + \frac{1}{m} \vec{\nabla} \bar{V}(\vec{x}) \cdot \vec{\nabla}_v f = \left. \frac{df}{dt} \right|_{\text{col}}. \quad (2.5)$$

where  $\bar{V}(\vec{x})$  is the average *self-consistent* potential acting on the particles and  $\left. \frac{df}{dt} \right|_{\text{col}}$  is the collision operator describing the effect of collisions. When collisions are neglected ( $\left. \frac{df}{dt} \right|_{\text{col}} = 0$ ), equation (2.5) is called the Vlasov equation<sup>?</sup>, which describes the dynamics of the a plasma with its self-consistent electro-magnetic background field.

In general, the form of the collision operator as well as the average potential depend on the physical properties of the system. The collision operator of a gas of neutral molecules is the Boltzmann operator, which is a non-linear functional of  $f(\vec{x}, \vec{v}, t)$  and takes into account the differential cross-section of the molecule scattering.

The collisions of charged particles in a plasma differ from the interaction of neutral molecules due to the long range of the Coulomb force (compared to a the van-der-Waals force between neutral particles). Instead of relatively few interactions with typically large scattering angles, charged particles undergo a large number of small-angle scattering events. This behavior is described by a Fokker-Planck-type<sup>†</sup> collision operator. The kinetic Landau equation has a form that is similar to a diffusion equation and the dynamics of the Fokker-Planck-distribution function shows a diffusion like behavior, accordingly: deviations from the Maxwellian equilibrium distribution gradually decay like density fluctuations in a diffusive material.

When the BBGKY hierarchy of a plasma is closed by expressing the next higher order (three-) particle distribution function in terms of the one and two particle distribution functions, the kinetic Lenard-Balescu equation<sup>27</sup> is obtained. The latter differs from the Landau equation in that the the Balescu collision operator is a much more non-linear functional of the distribution function. The screening of the Coulomb potential in a cloud of charged particles, which was discovered by Debye 1923<sup>28</sup>, appears in the Balescu equation derived from first principles.

The kinetic equations provide a detailed physical picture of a plasma, in principle allowing for a rigorous description by taking into account higher order correlations. A number of phenomena, like Landau damping, collisional transport, and others can be described in the kinetic picture. The solution of the full equations, however, may become quite involved, especially when complex boundary conditions are considered during the modelling of realistic plasma systems.

There are a number of simplifying assumptions, which are frequently applied to allow for an efficient description in these cases. Symmetries in the system may be used to reduce the number of relevant dimensions of the problem, or it may be sufficient to consider the spatially homogeneous case. The large difference in the electron and ion mass may allow to neglect the energy exchange

<sup>†</sup>The collision operator first derived by Landau<sup>26</sup> also has this property. Therefore, sometimes also the term Landau-collision operator is used.

between the two ensembles (Lorentz-gas approximation) Sometimes a kinetic description is not needed for all particle species in the plasma.

The so called fluid description is obtained from the kinetic equations by integrating the kinetic equations over velocity space, yielding equations for the moments of the velocity distribution function. The full set of equations for all moments is equivalent to the kinetic description, but usually only the lowest two or three moments are considered, when a simplified description is desired<sup>23</sup>.

In 2.2.2 some properties of an efficient model comprising a kinetic treatment of the free electrons of the neon dc-discharge are described.

### 2.1.5. Electron Energy Distribution Functions

The electron energy distribution function  $f(E, \vec{r})$  is obtained from the kinetic velocity distribution function by a variable transformation:

$$E = \frac{1}{2}m\vec{v}^2 \quad (2.6)$$

Since the transformation cannot unambiguously inverted, the energy distribution function contains less information than the velocity distribution function. The transformation can be computed, by a change to spherical coordinates and integration over the azimuthal and polar angle of the velocity:

$$f_i(E, r) = \iint v^2 \sin \theta_v d\phi_v d\theta_v f_{\text{kin},i}(\phi_v, \theta_v, v, \vec{r}) \frac{dv}{dE} \quad (2.7)$$

for isotropic EEDFs  $f_{\text{kin},i}(v, \vec{r})$  with no explicit dependence on  $\phi_v$  and  $\theta_v$  this simplifies to

$$f_i(E, \vec{r}) = \frac{4\pi v}{m} f_{\text{kin},i}(v, \vec{r}) \quad (2.8)$$

## 2.2. Properties of Glow Discharges

The term *discharge* was first used to describe the electrical break down through the air filled gap of an electrical circuit containing a capacitor. Later it was used for any flow of electric current through ionized gas, as well as any process of ionization of a gas by an applied electrical field<sup>17</sup>. A gas discharge at low pressures ( $\sim 10^1 \dots 10^3$  Pa) with a discharge current that is limited by the external circuit ( $\sim 10^{-6} \dots 10^{-1}$  A for a discharge with lateral dimension  $\sim 1$  cm) is called *glow discharge*. The voltage needed to sustain a dc glow discharge is in the range of hundreds to thousands of volts.

There are different modes of operation of glow discharges. Depending on the precise pressure and discharge current the column plasma may form different configurations of stable regions with varying brightness and especially for higher pressures ionization waves travelling from cathode to anode may occur<sup>17</sup>. In Fig. 2.1 a schematic picture of a stable stratified glow discharge is given. The clarity of the occurrence of the different dark and luminous layers is most pronounced at low pressures. The size of the cathode layers depends on the mean free path of the electrons. The positive column fills the residing gap towards the cathode. Its length depends on the size of the discharge tube.

In the regime of the *normal discharge* the current voltage characteristic of the discharge has got a negative slope, leading to the necessity of the external limitation of the discharge current by an ohmic resistor ( $\mathcal{O}(\text{k}\Omega)$ ). This behavior is caused by a positive feedback between increased ionization and increased electron density. The glow discharge is one of the most widely applied and well investigated type of gas discharges. A lot of experimental and theoretical results are available



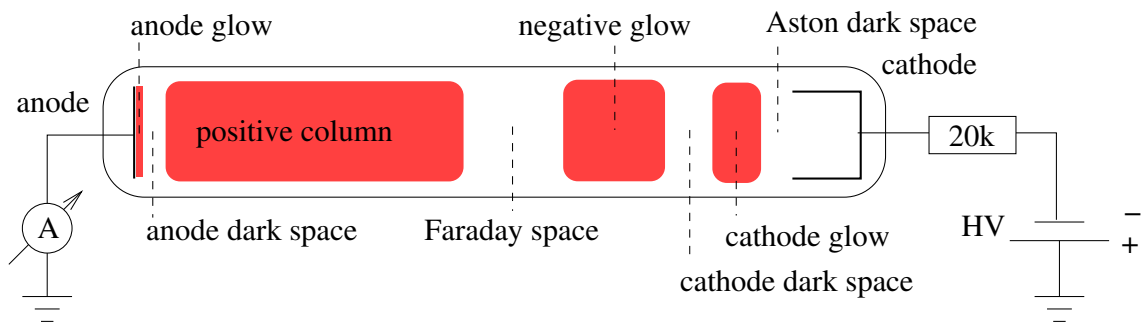


**Figure 2.1.:** Schematic picture of a stable dc glow discharge with the names of the different dark and luminous layers (luminous layers are indicated by red color).

in literature. The experimental operation is simple, the production and filling of the discharge tube being the greatest difficulty. The reproducibility of experimental conditions is also very good, allowing the comparison with results from literature for a given set of discharge parameters.

### 2.2.1. Qualitative Picture of Processes in Gas Discharges

The physical processes in a non-thermalized low-temperature plasma like the glow discharge are dominantly determined by the free electrons. Due to their high mobility they gain energy in the electric fields used to sustain the plasma. The light emission pattern in a stable low pressure glow discharge can be qualitatively understood by following the path of electrons emitted from the cathode:

The electrons are emitted from the cold cathode of the discharge mostly due to secondary emission caused by ion bombardment. Typical energies of the ejected electrons are less than 1 eV. In the strong field of the Aston dark space the electrons gain energy, until they reach the threshold to cause atomic excitation of neutral gas atoms. When the energy grows further, the excitation cross-sections start to fall off, causing the formation of the cathode dark space. In this region most of the ionization takes place, leading to electron multiplication. The slow moving ions build up a large positive space charge, shielding the bulk of the discharge from the strong electrical field in the cathode region. The weaker field lead to moderate electron energies in the region of the maximum of the excitation cross-sections, and the negative glow forms. The electrons loose energy in the negative glow by collisions and the (sometimes even reversed) field of the positive space charge. When the electrons don not reach the excitation threshold any more the Faraday dark space builds up. In the Faraday dark space the electric field gradually increases to the value in the positive column. In front of the anode a region of negative space charge is formed, leading to an increased field directly in front of the anode causing the anode glow.

The electrons of the glow discharge plasma are an example of a non-equilibrium kinetic system. The energy distribution is determined in the balance between plasma-heating and energy dissipation in inelastic collisions with atoms. In certain parameter regimes a stable steady state is reached (stable glow discharge). A survey of discharge regimes can be found in Fig. 2.2. The typical velocity distribution of a non-equilibrium low-temperature plasma is similar to, though deviating in detail from, a Maxwell-Boltzmann distribution and has a slight asymmetry reflecting the drift of the electrons towards the anode. The exponentially decreasing tail of high-energetic electrons causes excitation and ionization of atoms. The degree of ionization is typically in the range of  $10^{-8}$ .. $10^{-4}$ .

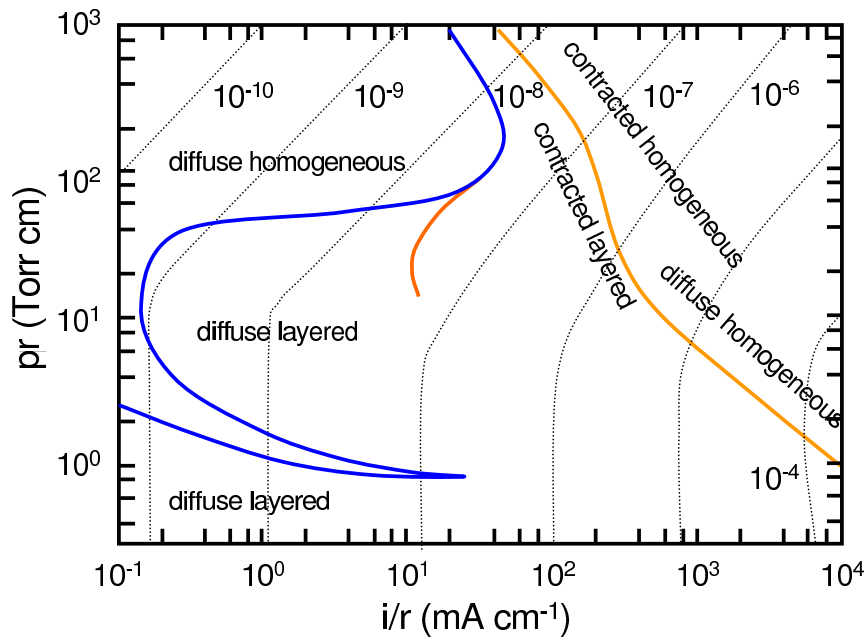


**Figure 2.2.:** Discharge regimes of neon glow discharges as a function of the similarity parameters radius normalized current  $i/r$  and pressure times radius. The figure was adapted from Ref. ( ? )

### Similarity Laws

In general, the particles in a plasma are exhaustively described by a set of kinetic equations (cf. 2.1.4) for the different species (like electrons, atoms in different states, ions and molecules) and accounting for the (self-consistent) electromagnetic fields obtained from Maxwell's equations, which have to be solved accounting for the charged particles of the plasma as well as external boundary conditions.

The properties of cylindrical discharges obey so-called similarity laws. This means, that the plasma properties are very similar for discharges with identical similarity parameters  $p \cdot r_0$  and  $I/r_0$  (gas pressure  $p$ , tube radius  $r_0$ , discharge current  $I$ ). Accordingly, the equations of state of a plasma have to show a at least approximate invariance properties to respective transformations. It was shown by Ref. (6), under which conditions this fulfilled for the Boltzmann equation of the electrons, as well as for Maxwell's equations in matter.

### Elementary Processes

The ground-state atoms or (to be more general) molecules of the plasma get excited to various kinds of unstable states, like excited or ionized atoms, atoms with free bindings, fractions of molecules or free radicals in the energetic environment of the plasma. Each production or destruction channel of a particle species, most of which are two body interactions is called *elementary process*. The kinetics of the population densities  $n_i$  of excited states  $i$  are described by a set of *rate equations* of the type

$$\frac{dn_i}{dt} = -R(i \rightarrow) + R(\rightarrow i) + \Gamma_i \quad (2.9)$$

where  $R(i \rightarrow)$  and  $R(\rightarrow i)$  are the sums of the rates of all transitions out of and into the atomic level  $i$ , respectively, and  $\Gamma_i$  is the external flux of particles caused by diffusion and convection. The time scales of the elementary processes are often very short compared to the speed of the

variation of the plasma conditions. In that case, which will be considered in the following, state populations are in a quasi steady-state and the left hand side of equation (2.9) vanishes, allowing to solve the rate equation for  $n_i$ . The system of rate equations obtain in this way is called *collisional-radiative model*. In the high density case, when thermal equilibrium can be attained at least locally, the excited states are populated according to Boltzmann statistic. In that case it is not necessary to solve the full collisional-radiative model. Another well-known approximation to the full rate equations is the corona-equilibrium, which is valid at very low densities<sup>?</sup>. In the intermediate density range, where typical densities of glow discharges lie, like many plasma used in technical applications, the collisional radiative model has to be solved.

**Table 2.2.:** Elementary processes important in an atomic plasma

$X_z + e \rightleftharpoons X_z^* + e$	collisional excitation and de-excitation
$X_z + e \rightleftharpoons X_{z+1} + e + e$	collisional ionization and three body recombination
$X_z + \hbar\omega \rightleftharpoons X_{z+1} + e$	photo-ionization and radiative recombination
$X_z + e \rightleftharpoons X_z^{**} \rightarrow X_z^* + \hbar\omega$	dielectronic recombination and auto-ionization
$X_z + e \rightleftharpoons X_z + e + \hbar\omega$	Free-free emission and absorption (Bremsstrahlung)
$X_z^* \rightleftharpoons X_z + \hbar\omega$	Excitation due to photon absorption and spontaneous photon emission

In table 2.2 the relevant elementary processes of an atomic (rare gas) plasma are summarized. The rates of all processes with one electron in the initial state can be expressed in terms of a cross-section  $\sigma$ :

$$R = n_e n_i \int_0^\infty v \cdot \sigma(E) f(E) dE, \quad v = \sqrt{\frac{2E}{m_e}}, \quad (2.10)$$

where  $n_e$  is the electron density,  $n_i$  is the density of atoms in the respective initial state, and  $v$  is the velocity of an electron with energy  $E$ .

The transition probability of spontaneous emission is an atomic property, which independent from the plasma state and quantified by the Einstein coefficient  $A$ :

$$R = A \cdot n_i \quad (2.11)$$

In the case of an optically thick plasma, however, the reabsorption of resonance photons leads to an apparent reduction of the transition rate, cf. 2.2.1.

The rates of processes involving three particles in the initial state are proportional to the flux of both collision partners. For example in the case of three body recombination equation (2.12) generalizes to:

$$R = n_e^2 n_{\text{ion}} \int \int v_1 v_2 \cdot f(E_1) f(E_2) \cdot \sigma(E_1, E_2; E) f(E) dE_1 dE_2 \quad (2.12)$$

The rate equations for the different atomic states are coupled due to different elementary processes like step-wise excitation or radiative transitions between excited states. Apart from few exceptions, the rates are proportional to the density of atoms in the respective initial state, causing the rate equations to form a system of coupled linear equations. See 5.2 for the details of the CRM used for the modelling of the spectroscopic data of the neon discharge.

### Radiation Transport

Resonance radiation emitted by excited atoms can easily be absorbed by atoms in the final state of the respective transition. If the absorber density is high, which is usually the case for transitions to the ground state or metastable excited states, the opacity of the plasma for the respective radiation has to be accounted for. The absorbing atom is excited to the upper state and re-emits a photon after time given by the characteristic life-time. After a number of repeated emissions and absorptions the photon escapes the plasma volume. This behavior resembles many features of particle diffusion and is called radiation transport. It is due to this similarity, that early approaches to model radiation transport are based on a diffusion equation.

There are, however, two important differences with respect to diffusion of particles: the first is the finite life-time of the excited states, delaying the re-emission of the photon. The diffusion equation can be adapted to this situation by the incorporation of an additional term<sup>29</sup>. The second more severe difference is the strong dependence of the emission and absorption probability on the precise energy or frequency of the photon, determined by the line shape of the transition. Slight changes in the photon-energy during a absorption/reemission process (this effect is called *frequency redistribution*) lead to an undefined mean free path of the photons, prohibiting a description of radiation transport by a simple diffusion equation<sup>29</sup>.

When the quantity of interest is the number of photons which leaves the plasma for a given spatial distribution of the excited states, the effect of the reabsorption of radiation can be expressed by a single number, the *escape factor*  $\Lambda$ . The latter indicates the fraction of photons leaving the plasma with respect to the number of photons emitted according to the natural time of life of the excited state.

Due to the above considerations, it is necessary to consider the precise line-shape and the underlying physical mechanisms for the description of radiation transport. Under the assumption of *complete frequency redistribution* during each absorption/re-emission event, the spatiotemporal evolution of the excited state densities  $n(\vec{r}, t)$  is described by the *Holstein-Bibermann equation*:

$$\frac{\partial n(\vec{r}, t)}{\partial t} = -\frac{1}{\tau}n(\vec{r}, t) + \frac{1}{\tau} \int_V n(\vec{r}', t)G(\vec{r}, \vec{r}') d\vec{r}' \quad (2.13)$$

(lifetime of the atomic state  $\tau$ , Plasma-volume  $V$ ). The kernel function  $G(\vec{r}, \vec{r}')$  quantifies the probability that a photon emitted at point  $\vec{r}'$  is reabsorbed at  $\vec{r}$ , this is where the line-shape of the transition enters the equation. The general solution of the Holstein-Bibermann can be written down as expansion in eigenmodes, which decay exponentially with time. In cylindrical discharges, the distribution of the excited states is similar to the fundamental mode of the Holstein-Bibermann equation<sup>29</sup>. In this case the decay constant of the lowest order mode, which is called the *trapping factor*, agrees well with the escape factor  $\Lambda$ . Formulae for trapping factors can be obtained in closed form using equation (2.13), when the line-shape can be well approximated either by a Gaussian distribution (Doppler-broadening) or a Lorentzian line-shape (collisional-broadening or natural line-shape), see e.g. Ref (<sup>29</sup>) for trapping factors in various geometries. When the line-shape has to be described by a Voigt profile (which is the case when Doppler- and collisional-

or natural line-broadening are important) the correct trapping factor has to be obtained from an appropriate interpolation between the two line-shapes. Available interpolations are not perfect at all opacities, an improved description can be achieved by taking into account *partial frequency redistribution*.

The simplifying assumption of complete frequency redistribution stands for the independence of the *emission* frequency from the frequency of the absorbed photon. A refined version of this concept, where the emitted photon at least partly 'remembers' at which frequency it was absorbed is called *partial frequency redistribution* (PFR). A generalized version of the Holstein-Bibermann equation for this case exists, but in practical applications, radiation trapping with PFR is frequently described using Monte-Carlo simulations. In this approach the Doppler broadening can be described in a fundamental way by randomly choosing an appropriate velocity for the absorbing and re-emitting atom and computing the Doppler shift between the atomic rest-frame the laboratory-frame. The redistribution in the rest-frame of the atom due to collisional broadening and the natural line-shape is obtained from a quantum mechanical description of the absorption/re-emission process<sup>29</sup>. The escape factors used in the collisional-radiative model and for the determination of the local emissivity are based on calculations of radiation transport taking into account PFR by Ref. (30) (cf. 5.5). In this work the results of different Monte-Carlo simulations covering a wide range of parameters concerning gas density, column radius and Doppler-width are summarized using empirical formulae.

### 2.2.2. Kinetic Modelling of Gas Discharges

The EEDF resulting from the present analysis is compared to a kinetic ab-initio model<sup>13</sup>. The model for the neon glow discharge plasma is based on an efficient combination of a kinetic treatment of the electrons together with the solution of steady-state fluid equations for the charge carriers in their self consistent radial electrical field. The most important collisions in the weakly ionized plasma are (elastic, inelastic and ionizing) electron-atom collisions, which are described by Boltzmann collision operators. Electron-electron collisions, leading to an additional Fokker-Planck type collision operator are not considered in Ref. (13). The angular dependence of the velocity distribution is implemented using an expansion in spherical harmonics. In the considered parameter regime, where the distribution is approximately isotropic because of elastic electron-atom collisions, a description facilitating the two-term expansion<sup>31</sup> is a good approximation. A non-local parameterization of the EEDF, which uses the total energy  $\varepsilon = \frac{1}{2}m_e v^2 - e_0 V_r(r)$  in order to account for the expected shift of the EEDF according to the radial electrostatic potential  $V(r)$  is used<sup>32</sup>. Nevertheless, the kinetic equation is set up radially resolved allowing for deviations from the strictly non-local approximation.

The result of the kinetic treatment are electron transport coefficients and ionization frequencies, which enter the fluid description of the charge carriers. A detailed treatment of excited atoms, comprising the four lowest lying excited states and an additional lumped level, is part of the model, it is required e.g. for a correct description of the ionization in the plasma.

The result of the kinetic self-consistent model is an exhaustive description of the plasma in the positive column, revealing, e.g., the spatial distribution of charged particles and excited atoms, the electrostatic potential, and in particular the electron energy distribution function at different radial positions as shown in Fig. 2.3.

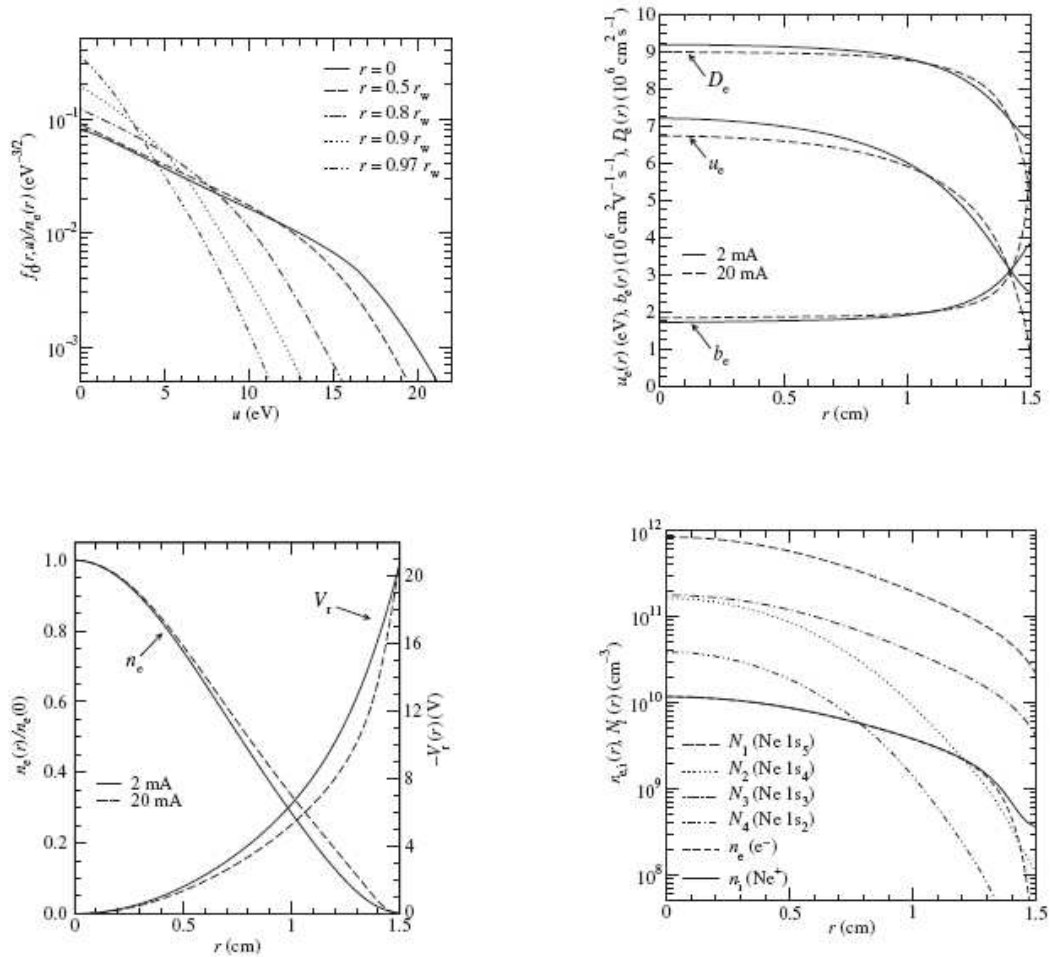


**Figure 2.3.:** Results of kinetic reference modelling of the discharge investigated in this work (neon pressure Pa). The figures are taken from a paper by Uhrlandt and Franke<sup>13</sup>. In the upper left figure, the isotropic part of the electron energy distribution function as a function of the kinetic energy is shown for different radial positions at a discharge current of 2 mA. The upper right figure shows the radial variation of the mean energy  $u_e$ , the diffusion coefficients  $D_e$  and the mobility of electrons  $b_e$  for the discharge currents as designated. The lower left figure show the radial profile of the electron density  $n_e$  and the variation of the space-charge potential  $V_f$ . The lower right figure shows the radial profile of excited state atoms and ion and electron density profiles, respectively, at 20 mA.

### 2.2.3. Electronic Excitation

Unlike in photo-excitation processes where selection rules apply, essentially all excited states of an atom can be populated. This comprises also the population of long-lived metastable atomic states, which take part in secondary electron collisions leading to step-wise excitation and ionization of the atoms. These reaction channels can give significant contributions to the population of the excited states in non-thermal plasmas.

### 2.2.4. Resonance Radiation

An atom in the excited state  $k$  will decay into a state  $i$  with lower energy and emit a photon carrying away the energy-difference  $\Delta E_{ki}$  with a certain probability per unit time, which is given by the *Einstein coefficient* for spontaneous photon emission  $A_{ki}$ . The power emitted from a unit volume into a unit solid angle, which is called the spontaneous line emission coefficient is given by:

$$\epsilon_{ki} = \frac{1}{4\pi} n_k \Delta E_{ki} A_{ki} \quad (2.14)$$

The observation of the emitted light of a certain transition  $k \rightarrow i$  allows the direct determination of the excited state density  $n_k$ , when the emitting plasma volume and Einstein coefficient are known and the reabsorption of the emitted photons can be neglected (cf. 2.2.1). Together with the electronic excitation this relation is a key ingredient for the reconstruction of the EEDF using the spectroscopic approach.

## 2.3. Determination of Excitation Cross-Sections

The availability of computational power allowing for the implementation of detailed plasma models has created a growing demand for precise atomic data in the last decades. At the same time the experimental and theoretical investigation of atomic physics has reached increasing levels of sophistication. The cross-sections (and Einstein coefficients) used in the present analysis are obtained from theoretical ab-initio calculations. Generally, theoretical calculations have the advantage, that complete data sets are available for all excitation channels from the ground (and sometimes the metastable states) into the considered excited states. The development of theoretical models does on the other hand, heavily depend on validation by experimental data.

The most common experimental method for the determination of excitation cross-section is electron-energy loss spectroscopy. Optical techniques are used for the measurement of excitation channels, with a radiatively decaying final state. Proper corrections for cascade contributions and branching have to be applied to the photo-emission cross-sections in that case. Recent advances of scattering experiments include the absolute measurements of cross-sections, experiments using coincidence techniques, spin polarized projectile beams and targets, high-energy-resolution electron beams, and bright beams of electrons<sup>33</sup>.

### 2.3.1. Theoretical Calculations of Cross-Sections

A brief overview over the methods for the calculation of atomic collision cross-sections shall be given here. It is based on a review article<sup>33</sup>. The focus is not set on the detailed and formally correct statement of the expressions, which would be needed for practical calculations, but on the basic ideas of the different approaches. Accordingly, normalization factors and spin wavefunctions are

usually left out for reasons of simplicity, but the important approximations and ansatzes are stated explicitly in the following.

Most theoretical derivations of cross-section of electron impact excitation are based on the solution of the *time-independent* Schrödinger- or Dirac equation for the  $(N + 1)$  electron collision system, consisting of the  $N$  electrons of the target atom plus the projectile-electron. Recently, solutions of the full relativistic problem, making use of the Dirac equation became available<sup>34</sup>, but this discussion is focussed on the simpler non-relativistic case. Also, initial value methods like *time-dependent close-coupling* or *exterior complex scaling* are being developed recently with the help of massively parallel supercomputers. These more direct methods have got the advantage, that the wave functions don not have to be described by finite basis sets. The extensive requirements of computational resources effectively restrict these methods to (quasi-) one or two electron systems at the moment.

In the following, the the time-independent problem will be formulated and two important classes of solutions, namely the *close coupling expansion* (CC) based solutions and the *Born series* based ones will be described. The former delivers a good description in the low-energy regime from the excitation threshold to the ionization energy of the atom, where so called "Feshbach"-resonances occur in the cross-sections. At higher energies than the ionization-threshold electrons of the target atom may be excited to unbound *continuum* states, whose effect can be described to some extent by the introduction of pseudo-states in the CC framework. This non-trivial extension of the approach allows its application at intermediate and high energies and the treatment of ionization collisions. Born series based solutions of the scattering problem, which are in general computationally much less demanding than close coupling methods, deliver appropriate solutions in the "high-energy" domain greater than several times the ionization threshold. They are based on a perturbative approach and usually neglect coupling effects between the excitation of different states of the target atom (channel coupling). The ionization cross-sections can be obtained from Born series based computation in a similar way to the excitation cross-sections without the need for special extensions of the approach.

### The Scattering Problem, Scattering Amplitude and Cross-Section

The quantum mechanical description of the scattering problem is formulated here before the basic ideas of the CC and born series approaches are outlined. The non-relativistic stationary case, which we focus on here, is described by the time-independent the Schrödinger equation:

$$H_{N+1}|\Psi\rangle = E|\Psi\rangle. \quad (2.15)$$

Where  $E$  is the energy of the whole  $N + 1$  electron system ( $N$  target electrons plus projectile), described by the wave function  $|\Psi\rangle$ . The Hamiltonian  $H_{N+1}$  of the electrons in the Coulomb potential of the target nucleus with nuclear charge  $Z$  has the form (in space coordinates):

$$H_{N+1} = \sum_{i=1}^{N+1} \left( -\frac{1}{2} \nabla_i^2 - \frac{Z}{r_i} \right) + \sum_{i>j=1}^{N+1} \frac{1}{r_{ij}} \quad (2.16)$$

where the  $\vec{r}_i$  are the coordinates of the  $i$ th electron and  $r_{ij} = |\vec{r}_i - \vec{r}_j|$  the distance between two electrons. The origin of the coordinate system is the target nucleus which is assumed to have an



infinite mass. We are looking for solutions fulfilling the asymptotic behavior:

$$\Psi_i \xrightarrow{r \rightarrow \infty} \Phi_i e^{ik_i z} + \sum_j \Phi_j f_{ji}(\theta, \phi) \frac{e^{ik_j r}}{r} \quad (2.17)$$

Where  $f_{ji}$  is the scattering amplitude describing the angular distribution of the outgoing electron, and  $\Phi_i$  are the target eigenfunctions describing the bound state of  $N$  electrons fulfilling the eigenvalue equation (eigenenergy  $w_i$  of bound state  $i$ )

$$\langle \Phi_i | H_N | \Phi_j \rangle = w_i \delta_{ij}. \quad (2.18)$$

The inelastic scattering changing a specific initial into a specific final state is called a scattering channel. When a scattering channel is energetically allowed it is said to be *open*, otherwise it is called *closed*.

Here and throughout the discussions, the part of the wavefunction describing the spin is omitted for reasons of simplicity. The descriptions of the different methods below will conclude with the respective wave-function solving the Schrödinger equation. It is assumed, that the scattering amplitude can be obtained from the resulting wave-functions by the consideration of the asymptotic behavior given in equation (2.17). Among factors accounting for the angular momentum conservation and the correct normalization of the wave functions, this involves matrix elements having a form similar to:

$$f_{ji} \simeq \langle \Phi_j, \psi_e | \Psi_i \rangle \quad (2.19)$$

where the fraction of the atoms in the respective final state  $\Phi_j$  is obtained by projection.  $\psi_e$  is the part of the wavefunction describing the scattered electron typically by a plane or distorted plane wave. The cross section is obtained from the scattering amplitude using the relation:

$$\frac{d\sigma_{ji}}{d\Omega} = \frac{k_j}{k_i} |f_{ji}(\theta, \varphi)|^2 \quad (2.20)$$

For targets with high nuclear charge  $Z$  relativistic effects become important even for low-energy scattering. This effects the target wave functions  $\Phi_i$  and also the wave function of the scattered electron. One way of achieving a relativistic description is the use of the Breit-Pauli Hamiltonian where terms accounting for the one-body spin orbit interaction, the mass correction, the Darwin term as well as possibly two-body relativistic terms are added to the Hamiltonian  $H_{N+1}$ . Alternatively a description based on the relativistic Dirac equation may be employed. The principle ideas of the solution of the problem, do not depend on whether a relativistic description is used. The following discussion is based on the non-relativistic case for clarity.

### Born Series

The Born series is a perturbative approach to the scattering problem (2.15), which is based on a splitting of the Hamiltonian  $H_{N+1}$  into a part describing the unperturbed atom  $H_N$  and the free electron  $K_p$  and a part describing the interaction between the two  $H_I$ :

$$H_{N+1} = (H_N + K_p) + H_I, \quad H_I = -\frac{Z}{r_{N+1}} \sum_{j=1}^N \frac{1}{r_{i(N+1)}}. \quad (2.21)$$

In that case the Schrödinger equation (2.15) can be rearranged to the Lippmann-Schwinger equation (see e.g. Ref<sup>2</sup>)

$$|\Psi_i\rangle = |\Phi_i, \vec{k}\rangle + \frac{1}{E - H_N - K_p + i\varepsilon} H_I |\Psi_i\rangle \quad (2.22)$$

Where  $|\Phi_i, \vec{k}\rangle$  is the combined wave function of the target atom  $|\Phi_i\rangle$  and the free particle  $|\vec{k}\rangle$ . The Lippmann-Schwinger equation can be solved formally by the so called the Born series:

$$|\Psi_i\rangle = |\Phi_i, \vec{k}\rangle + G_0^+ H_I |\Phi_i, \vec{k}\rangle + G_0^+ H_I G_0^+ H_I |\Phi_i, \vec{k}\rangle + \dots, \quad (2.23)$$

where the Green's function operator  $G_0^+ = (E - H_N - K_p + i\varepsilon)^{-1}$  is used. When the interaction Hamiltonian  $H_I$  is small compared to the free Hamiltonian  $H_N + K_p$  the Born series can be expected to converge and would deliver the exact solution of the Schrödinger equation when it could be carried to infinity.

In particular do the higher order terms of equation (2.23) describe the coupling between the different excitation channels by the repeated application of the  $G_0^+ H_I$  operators to the states  $G_0^+ H_I |\Phi_i, \vec{k}\rangle$ , which are mixed states in the unperturbed atomic basis. In practice these terms are usually not considered and higher orders of perturbation are, if at all, only computed for the wave function of the scattered electron. This is the major simplification compared to the close coupling approach, which disallows the description of Feshbach-type resonances and makes the Born series approaches inappropriate for scattering near the excitation threshold.

The elastic scattering at high energies, in contrast, can often be already described by the so called *First Born approximation*, where only the first term is kept. In that case the incoming, as well as the outgoing electron is described by a plane wave. In general, it is important to retain consistently all terms of the series which have a similar dependency on the momentum transfer<sup>33</sup>  $|\vec{k}_i - \vec{k}_f|$ . Cross-sections obtained by Born series based approaches show the correct asymptotic behavior for high energies, which is  $\sigma^B \propto E^{-1} \ln E$  for dipole allowed transitions ( $\Delta l = \pm 1, \Delta S = 0$ ),  $\sigma^B \propto E^{-1}$  for parity forbidden transitions and  $\sigma^B \propto E^{-3}$  for spin forbidden transitions.

**Distorted-Wave Method** The perturbative approach, which consists of the division of the Hamiltonian  $H_{N+1}$  into a dominant part, which is solved exactly and a small correction, which is treated as perturbation, can be carried through in different ways. A part of the projectile-target interaction  $H_I$  can be incorporated in the non-perturbative Hamiltonian. The plane wave describing the free electron is in this case replaced by the distorted wave  $\chi_E$ , which is determined by the differential equation

$$\left[ \frac{d^2}{dr^2} - \frac{l(l+1)}{r^2} - 2H_{I,D}(r) \right] \chi_E(r) = 0 \quad (2.24)$$

where  $H_{I,D}$  is the part of the interaction treated exactly. The transition matrix elements are then calculated with the help of the distorted waves, treating in first order the part of the interaction not treated in the distortion potential  $H_{I,D}$ . The distortion of the incident and scattered electron wave is particularly important in the case of the scattering on ions, where the long range coulomb forces have to be considered. This is than called Coulomb-Born approximation.

The distorted wave born approximation (DWBA) becomes more accurate at intermediate energies and with increasing charge of the ion. Consequently it is a useful tool under these circumstances. Partial-wave cross sections at high angular momenta can also be accurately described by Born series based approaches, because the angular momentum barrier depresses the importance of the coupling potential.

The first-order plane wave approaches (FBA) generally overestimates cross-sections in the vicinity of their maximum by a factor of two to three. This is an effect of the neglected polarization of the atom by the incident electron. In many cases of practical interest, however, the results of the FBA calculations can be used to get reasonable results for optically allowed transitions by employing a rescaling transformation of the results suggested by Kim<sup>35</sup>.

### The Close Coupling Expansion

Now a class of solutions of the Schrödinger equation (2.15) is considered which makes use of an expansion of  $|\Psi\rangle$  in the basis of solutions  $|\Phi_j\rangle$  of the  $N$  electron Hamiltonian (and possibly pseudo states added to the set of  $|\Phi_j\rangle$ ) The corresponding expansion coefficients play effectively the role of wave functions for the scattering electron. In spatial coordinates a typical close coupling expansion has the form:

$$\Psi_i = \mathcal{A} \sum_j \bar{\Phi}_j(\vec{r}_1, \dots, \vec{r}_N, \hat{r}_{N+1}) F_{E,i}(r_{N+1}) + \sum_j \chi_j(\vec{r}_1, \dots, \vec{r}_{N+1}) a_{ji} \quad (2.25)$$

Where the operator  $\mathcal{A}$  antisymmetrizes the first summation according to the Fermion statistics of the electrons. The channel functions  $\bar{\Phi}_j$  are obtained by coupling the target states  $\Phi_i$  with the angular (and spin, though not considered here) dependency (unit vector  $\hat{r}_{N+1}$ ) of the wave function of the projectile-electron. The functions  $F_{ji}(r_{N+1})$  are called the reduced radial functions of the scattered electron. The additional anti-symmetrized and square-integrable correlation functions  $\chi_j$  can be used to describe additional short-range correlations. They are also needed when an orthogonality condition between  $F_{ji}$  and the radial dependence of the bound orbitals is imposed for reasons of numerical convenience.

In numerical implementations the expansion has to be cut off after a number of states. The simplest case, where only one final target state is retained, is called the *static exchange approximation*. When more target states are considered, the transitions between all states of the expansion can be calculated, but the obtained cross-section are typically only accurate up to the threshold of the highest state kept in the expansion. The coupling to open and closed channels retained in equation (2.25) arises naturally in the close coupling framework.

By substituting (2.25) into the Schrödinger equation (2.15), projecting onto the basis states  $\Phi_j$  and  $\chi_j$  and eliminating the coefficients  $a_{ji}$ , a system of coupled integro-differential equations for the radial functions  $F_{ji}$  is obtained:

$$\left( \frac{d^2}{dr^2} - \frac{l_j(l_j+1)}{r^2} + \frac{2Z}{r} + k_j^2 \right) F_{ji}(r) = 2 \sum_l (V_{jl} + W_{jl} + X_{jl}) F_{li}(r), \quad (2.26)$$

where  $l_j$  is the orbital angular momentum of the scattered electron and  $V_{jl}$ ,  $W_{jl}$  and  $X_{jl}$  are the partial-wave decompositions of the local direct-, nonlocal exchange-, and nonlocal correlation-potential. The potential  $V_{jl}$  describing the repulsion of the  $N$  target electrons can be written as

$$V_{jl}(r_{N+1}) = \left\langle \Phi_j \left| \sum_{i=1}^N \frac{1}{r_{i,N+1}} \right| \Phi_l \right\rangle, \quad (2.27)$$

where the integral is taken over all  $N+1$  electron space coordinates except for the radial coordinate of electron  $N+1$ . The non-local exchange and correlation potentials  $W_{jl}$  and  $X_{jl}$  cannot be formulated analytically. In practical implementations, they are constructed by special program packages.

The equations of the CC expansion (2.26) are solved by a number of different methods. To be mentioned are the R-Matrix methods, the reduction of (2.26) to linear algebraic equations, the non-iterative integral equations method and the Kohn variational method. In Ref. (33) more literature on these methods is given. Significant work has been devoted to account in some approximate way for the high lying discrete and continuum states of the target. This resulted in the so called convergent close coupling method<sup>2</sup> and the R-matrix with Pseudo-States method (RMPS) proposed by Bartschat et al.<sup>2</sup> based on the same idea. The program package BSR<sup>62</sup> is based on the use of basic spline ("B-splines") as a universal and effectively complete basis to expand the wave function of the scattering electron inside the R-matrix box. The cross-section for electronic excitation of neon used in the present analysis are obtained by the BSR package. The use of basis of term-dependent, non-orthogonal sets of orbitals reveals a very accurate target description. The BSR approach can be used also when pseudo states are used to account for the effects of continuum-coupling. As in other solution methods, the number of pseudo states needed for an accurate description, especially of complex targets like neon, however, may be considerable<sup>67</sup>. The data set of Einstein coefficients used in the present analysis is obtained from these structure calculations.

### 2.3.2. Rates of Direct and Reverse Processes

The matrix element  $T_{a \rightarrow b} = \langle a|T|b \rangle$  is equal to the time reversed process  $T_{b \rightarrow a} = \langle b|T|a \rangle$  if the Hamiltonian of the interaction is time-reversal-invariant. It can be shown that for the cross-section of the reverse process in that case the following equation holds<sup>36</sup>:

$$k_b^2 \cdot d\sigma_{ba} = k_a^2 \cdot d\sigma_{ab} \quad (2.28)$$

where  $k_{a,b}$  is the momentum of the scattering electron in the initial state of the transition.

The same relation can be obtained by considering a plasma in local thermodynamic equilibrium, where *detailed balance* holds, which states that the rate of each process has to equal the rate inverse process. In order to fulfill this condition for any electron temperature  $T_e$ , the cross-section for an electronic excitation process has to fulfill the *Klein-Rosseland* formula

$$g_b \cdot (E + \Delta E) \cdot \sigma_{ba}(E + \Delta E) = g_a \cdot E \cdot \sigma_{ab}(E) \quad (2.29)$$

where  $\Delta E$  is the threshold energy off the cross section and  $g_{a,b}$  is the statistical weight of the level  $a$  or  $b$ , taking into account the multiplicity of degenerated levels. This relation is used to obtain the cross-sections for electronic de-excitation in the present analysis.

## 2.4. Atomic physics in the Discharge in Neon

This section summarizes the basic notions for the neon spectroscopy in the investigated discharge.

In table 5.1, a survey of states used in the spectroscopic model is given for the 14 lowest lying states in neon, a more extensive table is given in Appendix E for reference.

Figure 2.4 shows a simplified Grotrian diagram of neon also indicating the most relevant emission multiplets. The red lines, predominantly visually noticed, emerge from the  $3p \rightarrow 3s$  multiplet. The strongest lines to the ground state are in the vacuum ultraviolet spectral range. Additional information from multiplets ending in the  $3p$  levels and  $4p \rightarrow 3s$  transitions are also used in the present work.

The Grotrian diagram allows to identify the energies which are 'probed' by the emission spectroscopic measurements, i.e. the energy differences corresponding to the electron excitation energy

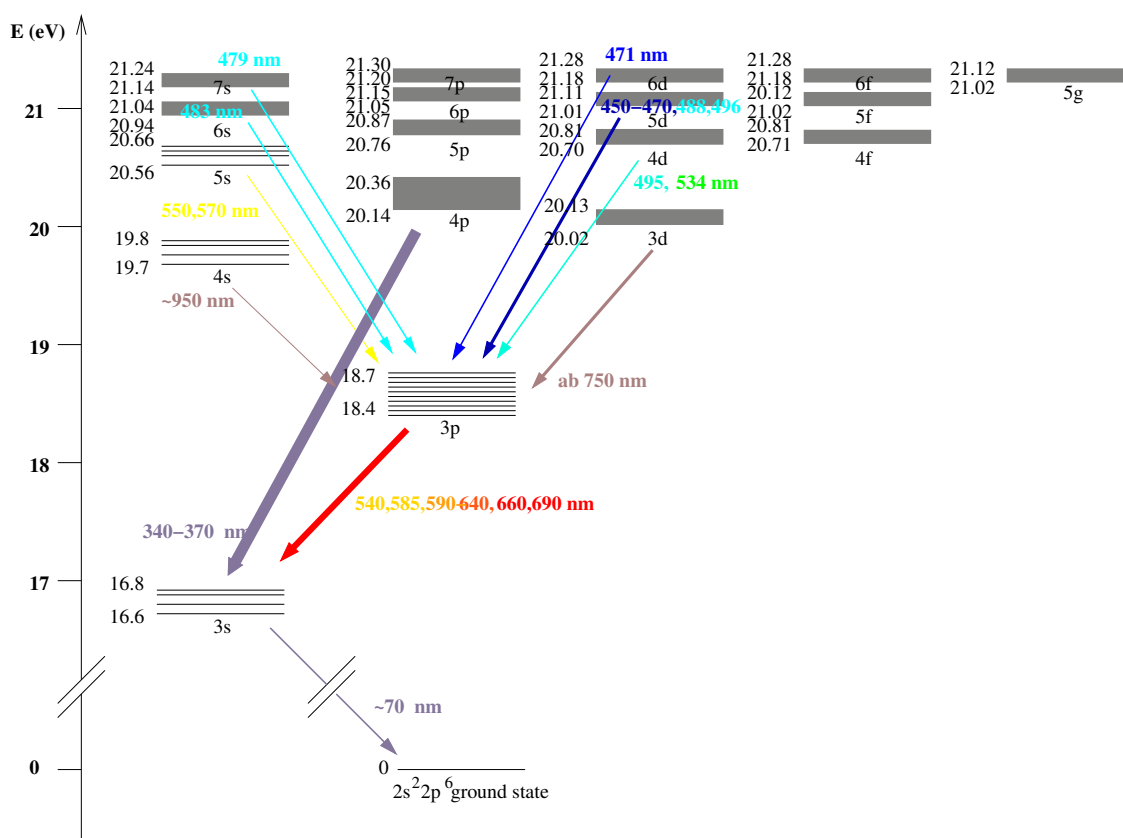


**Figure 2.4.:** Energy level diagram of neutral neon. The thickness of the shown transition reflects the line-strength<sup>37</sup>, the data is taken from NIST<sup>37</sup>.

energies from the most populated states, i.e. the ground state and the  $3s$  levels. As it will be shown later, these differences can be identified in the sensitivity analysis of the reconstruction of the electron energy distribution function.

With the Grotrian diagram at hand, it is to be noted that a full model describing the spectral lines is fitted to all spectroscopic data. In contrast to simple line ratio methods for which only a subset of the state populations is modelled. Consequently, as will be shown along this thesis, the present spectroscopic approach facilitates the diverse energy dependences of the excitation processes as implemented in the model for the determination of the electron kinetic.

#### 2.4.1. Notation of the Excited States.

A convenient labelling of the excited states similar to Paschen's notation is used throughout the paper: The principal quantum number  $n$  and the orbital angular momentum  $l$  of the excited electron are combined with an energy ordered index, which is one for the state with highest energy among the states with identical  $n$  and  $l$ .

In the context of the CRM, an index is used for the atomic states taken into account. In the present work, we chose 0 for the ground state, 1 to 30 for the excited states (increasing with energy), and 31 for the ionized atom.

**Table 2.3.:** Excited states of neon. The assignment between the physical (intermediate  $jK$  coupling) states to the approximated  $LS$  coupling is based on the BSRM<sup>38</sup> calculations.

Index	Label	Paschen's notation	Configuration in $jK$	Configuration in $LS$	Energy [eV] (NIST <sup>37</sup> )
0	2p <sub>1</sub>	1s <sub>1</sub>	2p <sup>6</sup> <sup>1</sup> S <sub>0</sub>	2p <sup>6</sup> <sup>1</sup> S <sub>0</sub>	0
1	3s <sub>4</sub>	1s <sub>5</sub>	2p <sup>5</sup> ( <sup>2</sup> P <sub>3/2</sub> <sup>o</sup> )3s <sup>2</sup> [ $\frac{3}{2}$ ] <sup>o</sup> , $J = 2$	2p <sup>5</sup> 3s <sup>3</sup> P <sub>2</sub>	16.61907
2	3s <sub>3</sub>	1s <sub>4</sub>	2p <sup>5</sup> ( <sup>2</sup> P <sub>3/2</sub> <sup>o</sup> )3s <sup>2</sup> [ $\frac{3}{2}$ ] <sup>o</sup> , $J = 1$	2p <sup>5</sup> 3s <sup>3</sup> P <sub>1</sub>	16.67083
3	3s <sub>2</sub>	1s <sub>3</sub>	2p <sup>5</sup> ( <sup>2</sup> P <sub>1/2</sub> <sup>o</sup> )3s <sup>2</sup> [ $\frac{1}{2}$ ] <sup>o</sup> , $J = 0$	2p <sup>5</sup> 3s <sup>3</sup> P <sub>0</sub>	16.71538
4	3s <sub>1</sub>	1s <sub>2</sub>	2p <sup>5</sup> ( <sup>2</sup> P <sub>1/2</sub> <sup>o</sup> )3s <sup>2</sup> [ $\frac{1}{2}$ ] <sup>o</sup> , $J = 1$	2p <sup>5</sup> 3s <sup>1</sup> P <sub>1</sub>	16.84805
5	3p <sub>10</sub>	2p <sub>10</sub>	2p <sup>5</sup> ( <sup>2</sup> P <sub>3/2</sub> <sup>o</sup> )3p <sup>2</sup> [ $\frac{1}{2}$ ], $J = 1$	2p <sup>5</sup> 3p <sup>3</sup> S <sub>1</sub>	18.38162
6	3p <sub>9</sub>	2p <sub>9</sub>	2p <sup>5</sup> ( <sup>2</sup> P <sub>3/2</sub> <sup>o</sup> )3p <sup>2</sup> [ $\frac{5}{2}$ ], $J = 3$	2p <sup>5</sup> 3p <sup>3</sup> D <sub>3</sub>	18.55511
7	3p <sub>8</sub>	2p <sub>8</sub>	2p <sup>5</sup> ( <sup>2</sup> P <sub>3/2</sub> <sup>o</sup> )3p <sup>2</sup> [ $\frac{3}{2}$ ], $J = 2$	2p <sup>5</sup> 3p <sup>1</sup> D <sub>2</sub>	18.57583
8	3p <sub>7</sub>	2p <sub>7</sub>	2p <sup>5</sup> ( <sup>2</sup> P <sub>3/2</sub> <sup>o</sup> )3p <sup>2</sup> [ $\frac{3}{2}$ ], $J = 1$	2p <sup>5</sup> 3p <sup>1</sup> P <sub>1</sub>	18.61270
9	3p <sub>6</sub>	2p <sub>6</sub>	2p <sup>5</sup> ( <sup>2</sup> P <sub>3/2</sub> <sup>o</sup> )3p <sup>2</sup> [ $\frac{3}{2}$ ], $J = 2$	2p <sup>5</sup> 3p <sup>3</sup> P <sub>2</sub>	18.63679
10	3p <sub>5</sub>	2p <sub>5</sub>	2p <sup>5</sup> ( <sup>2</sup> P <sub>1/2</sub> <sup>o</sup> )3p <sup>2</sup> [ $\frac{3}{2}$ ], $J = 1$	2p <sup>5</sup> 3p <sup>3</sup> D <sub>1</sub>	18.69336
11	3p <sub>4</sub>	2p <sub>4</sub>	2p <sup>5</sup> ( <sup>2</sup> P <sub>1/2</sub> <sup>o</sup> )3p <sup>2</sup> [ $\frac{3}{2}$ ], $J = 2$	2p <sup>5</sup> 3p <sup>3</sup> D <sub>2</sub>	18.70407
12	3p <sub>3</sub>	2p <sub>3</sub>	2p <sup>5</sup> ( <sup>2</sup> P <sub>3/2</sub> <sup>o</sup> )3p <sup>2</sup> [ $\frac{5}{2}$ ], $J = 0$	2p <sup>5</sup> 3p <sup>1</sup> S <sub>0</sub>	18.71138
13	3p <sub>2</sub>	2p <sub>2</sub>	2p <sup>5</sup> ( <sup>2</sup> P <sub>1/2</sub> <sup>o</sup> )3p <sup>2</sup> [ $\frac{1}{2}$ ], $J = 1$	2p <sup>5</sup> 3p <sup>3</sup> P <sub>1</sub>	18.72638
14	3p <sub>1</sub>	2p <sub>1</sub>	2p <sup>5</sup> ( <sup>2</sup> P <sub>1/2</sub> <sup>o</sup> )3p <sup>2</sup> [ $\frac{1}{2}$ ], $J = 0$	2p <sup>5</sup> 3p <sup>3</sup> P <sub>0</sub>	18.96595

### 3. Concepts of Probabilistic Data Analysis

The mathematical concepts that form the basis for statistical data analysis are briefly introduced in the following chapter. The presentation of the ideas of *plausible reasoning* as the natural generalization of deductive logic to the case of uncertain available information follows the introductory books on the topic<sup>39,40</sup>. The book written by Sivia<sup>41</sup> provides a good starting point for further reading on the topic.

After introducing the general scope of probability theory and the plausibility interpretation of probability, the implications of the basic equation for statistical inference, called *Bayes theorem*, are discussed. The role of the principle of Maximum entropy as a tool to identify probability distributions with minimal information content is described. Guidelines for the practical implementation of a probabilistic data analysis<sup>1</sup> are given and the main tool for the numerical investigation of the multi-dimensional probability density functions, namely the Monte Carlo method is introduced. The application of the concepts introduced in the following chapter to the case of the present data analysis of spectroscopic data is described in chapter 6.

#### 3.1. Probability Theory

Probability theory is, in a general sense, the framework for computations involving quantities that are subject to a sort of uncertainty (which will be specified) and which are called *random variables* in the following. A (discrete) random variable  $\theta$  cannot be assigned a single definite value but instead has a set of  $n$  possible values  $\theta_i$ , and a probability  $p_i = p(\theta_i)$  associated with every value, that  $\theta$  may equal  $\theta_i$ . In the continuous case, when  $n \rightarrow \infty$  the  $\theta$  is characterized by its *probability density function*  $p(\theta)$ , where the probability of  $\theta$  to lie in the differential interval  $\{\theta_0, \theta_0 + d\theta_0\}$  is given by

$$\Pr(\theta_0 < \theta < \theta_0 + d\theta_0) = p(\theta_0) d\theta_0 \quad (3.1)$$

Historically two ways have been developed of defining the term 'probability' used here: Early works on the topic, performed by Bernoulli, Bayes and Laplace in the context of the prediction of orbits of celestial objects from uncertain observations at hand, are now regarded as the first examples, for the use of probability theory as an extension of logic to cases of incomplete (i.e. uncertain) information, where Aristotelian deductive reasoning is not possible<sup>40</sup>. In the Laplacian interpretation, probability is regarded as the *plausibility* of the random variables to have a certain value, e.g. the orbit of some celestial object to be of a certain magnitude, rather than another. Based on this ideas Laplace was able to solve, for example, the 'inequality of Jupiter and Saturn'<sup>39</sup>, which was an outstanding problem of science in the 18th century. Unfortunately, Laplace did not formulate the unique requirement of the laws of probability calculus which can be derived from the mere definition of the plausibility interpretation.

Alternatively, this can be easily accomplished when defining probability as the relative *frequency* of the occurrence of an outcome of an infinitely often repeated random experiment. This is also often called the frequentist's definition of probability. Most of the work in the field of statistical inference during the twentieth century was based on this school of thought<sup>40</sup>, because of its well defined character. However, although setting the probabilistic approach on a well defined basis,

the frequentist's point of view suffers from the fact, that it's premise of an identically repeatable experiment is often not applicable in practical inference problems.

In the 1940s and 50s of Polya, Cox and Jaynes showed that the sum- and product rules for conditional probabilities can also be derived from a set of 'desiderata' defining the plausibility interpretation of probability. The term desideratum refers to the fact, that the assumptions taken by Jaynes don't assert anything to be true, but only state desirable goals for a theory of plausible reasoning. The important point of this reinvention of the rules of probability calculus is the much broader applicability of the theory.

In the present work this more general interpretation, which is often called the Bayesian interpretation of probability, is adapted. It allows to extract the information from the spectroscopic data and to make inference about the properties of the electron component, which dominantly determines the properties of the plasma. In this chapter the basic ideas of the Bayesian approach and its most important methods for the field of data analysis will be discussed. The concept of plausible reasoning will be introduced and the two important cases of parameter estimation and hypothesis testing problems will be discussed. The different steps of the employed data analysis are outlined

#### 3.1.1. Plausible Reasoning and Data Analysis

In the context of probability theory, the *plausible reasoning* means the consideration of the validity of a proposition about which only *uncertain* knowledge is available. In this sense, it is a generalization of deductive (Aristotelian) kind of inference, which is often used, for example, in mathematics, where the available knowledge is typically of *definite* axiomatic kind. Definite knowledge is the limiting case of uncertain knowledge, when the uncertainty is diminished by including more and more information and the conclusions of deductive logic must be re-obtained from plausible reasoning in this limit.

A typical example of plausible reasoning is the estimation of model parameters from experimental data. Some scientific theory might not be able to state the value of a numerical parameter from first principles. Instead, the values of has to be extracted from observations of reality (Consider for example the gravitational constant of Newtons law of gravity, or the mixing angles and the phase of the Cabibbo-Kobayashi-Maskawa quark mixing matrix of the standard model of particle physics<sup>42</sup>). As experiments are generally subject to uncertainty, so are the extracted physical parameters. The result of the experiment will be the plausibility of different values for the physical constant. (Which will be encoded in a pdf for that constant) Formally the testing of an hypothesis, i.e. computation the plausibility of a theory as whole turns out to be closely connected to the parameter estimation problem. The vast majority of the issues in (plasma-) physical data analysis fall in on of the categories of *parameter estimation* or *hypothesis testing*. For both classes of data analysis problems the probability, which is to be obtained can be written down in the same way:

$$P(\text{hypothesis}|\text{data}) = P(\text{data}|\text{hypothesis}) \times \frac{P(\text{hypothesis})}{P(\text{data})}. \quad (3.2)$$

This equation follows directly from the application of sum and product rule for conditional probabilities and is usually called *Bayes' theorem*. It relates the desired probability of the the hypothesis (given the data) to something which is usually calculable, namely the expected outcome of the experiment for a given hypothesis ( $P(\text{data}|\text{hypothesis})$ ) (called the likelihood). As equation (3.2) is the basic equation for most problems of statistical inference, there are names established for its terms:

- the resulting probability  $P(\text{hypothesis}|\text{data})$  is called *posterior*,



- the statistical model of the data  $P(\text{data}|\text{hypothesis})$  is called *likelihood*,
- the probability of the hypothesis  $P(\text{hypothesis})$  regardless of the currently considered data is called *prior*,
- and the residing term  $P(\text{data})$  is called the *evidence*.

The two mentioned categories of data analysis problems differ in the kind of hypothesis, which is considered. In the case of hypothesis testing the a qualitative hypothesis, similar to '*the electron energy distribution function of this plasma can be described by a specified kinetic simulation*', while in parameter estimation problems a collection of hypothesis of the form '*the unknown parameter  $\theta$  is in the range  $\theta_0 + d\theta_0$* ' is considered. In the latter case the posterior is a continuous pdf of the parameter  $\theta$  or more generally of the vector of parameters  $\vec{\theta}$ . Equation (3.2) is then written as

$$p(\vec{\theta}|\vec{D}) = p(\vec{D}|\vec{\theta}) \times \frac{p(\vec{\theta})}{p(\vec{D})}, \quad (3.3)$$

where  $\vec{D}$  represent the sequence of all measured data, which are taken into account. Note, that the *evidence*  $P(\vec{D})$  is not a function of  $\vec{\theta}$ . Therefore it is defined uniquely by the normalization  $\int P(\vec{\theta}|\vec{D}) d\vec{\theta} = N_p$  of the posterior. In parameter estimation problems the validity of the model is assumed and  $N_p = 1$ . This is not the case for the comparison of different models, which is done in hypothesis testing, as discussed below. Consequently, the evidence is often not computed in parameter estimation problems. Only the form (location of the maximum and width) of the posterior is of interest in that case.

### 3.1.2. Likelihood

The most effort in the actual implementation of equation (3.2) is the formulation of the likelihood. The physical model for the experimental data, which the considered hypothesis is a part of, enters the formalism here. It should be noted, that the likelihood can always be formulated, because if the outcome of the experiment, expected on the grounds of the valid hypothesis, cannot be formulated, the experiment is usually not suited to validate the hypothesis from the beginning. Often, the likelihood of experimental data is composed of two ingredients: a deterministic, physical model for the 'expected' data  $\vec{D}_{\text{sim}}(\vec{\theta})$  given the hypothesis, and the possible fluctuation of the actual measured data, caused by the finite precision of a real-world experiment, which is called the *error statistics* of the measurement. Moreover, it is quite frequently a good approximation to assume independent normal distributed errors, for which the likelihood can be written down as:

$$p(\vec{D}|\vec{\theta}) = \frac{1}{(2\pi)^{n/2} \prod_{i=1}^n \sigma_i} \exp \left\{ -\frac{1}{2} \sum_{i=1}^n \frac{(D_i - D_{\text{sim},i}(\vec{\theta}))^2}{\sigma_i^2} \right\} \quad (3.4)$$

The description of the error statistics of the data, inherently provides a measure to distinguish structures, which are features of the physical model from mere statistical fluctuations.

Equation (3.3) can be regarded as an *inversion* of the physical model for the data: the mapping from  $\vec{\theta}$  to  $\vec{D}$ , which is given by the data model, is inverted to some sort of 'mapping' which allows to determine  $\vec{\theta}$  from the measured data. It is for this reason, that parameter estimation tasks are also called inverse problems. For a successful inversion inversion, the likelihood has to provide an *unbiased* and *statistically correct* description of the data. Systematic differences between model and data have to be understood and incorporated in the model.

### 3.1.3. Updating Plausibilities: Prior and Posterior

A necessary ingredient for the inversion of the likelihood into a pdf for the parameters of interest  $\vec{\theta}$  is the prior probability  $p(\vec{\theta})$ . The prior represents the state of knowledge about  $\theta$  independent from the currently analyzed experiment. In this way, Bayes rule allows to combine 'new' information (encoded in the likelihood) with 'old' information contained in the prior distribution. The information given by the prior can itself be the result of a data analysis from a different (independent) experiment, in this case the posterior of one analysis is used as prior for the other analysis. The order in which the experiments are analyzed has no influence on the final result, just as the analysis of a set of  $n_d$  independent(!) data points can be equivalently performed using a single combined likelihood, or by setting up  $n_d$  separate likelihoods in  $n$  versions of Bayes rule to update information step by step.

As a side note, the following idea is mentioned: When for a given pdf every piece of information is factored out using Bayes theorem, what is eventually left as a prior in the last instance of equation (3.3), is a pdf quantifying total ignorance about  $\theta$ . The mathematical representation of this pdf is not as trivial as writing down a constant  $p(\vec{\theta})$ , what can be imagined when thinking of the fact, that it is usually possible to find equivalent parameterizations of any given problem. A flat prior pdf in one parameterization may not be flat in a different parameterization, which is nevertheless able to describe the present problem. This leads to the obvious question, in which of the possible parameterizations  $p(\vec{\theta})$  should be flat. This issue will be addressed briefly in 3.1.5. For a practical proceeding it is assumed, that there is a way of expressing sufficient ignorance in the (somehow flat) priors, that the result of the analysis will be dominated by the information included in the likelihood.

It should be mentioned, that all information quantified by the terms in equation 3.2 implicitly depends on the validity of the applied models and all underlying assumptions. This is sometimes explicitly written down as an additional variable  $I$ , which all the pdfs (prior, posterior, likelihood and evidence) are conditional on. By this, it is emphasized that probability theory delivers *objective* results only in the sense, that the incorporation of specific information always leads to the same result. Even subtle differences in the model assumptions will lead to different numerical results for resulting posterior pdf.

In physical parameter estimation problems, the multi dimensional posterior, is often summarized by only a few numbers, e.g. the most probable value of each parameter and its confidence region. This description only works for uni-modal posteriors, i.e. for the case when the posterior has only a single well-defined maximum and the correlations between the parameters are negligible. When, for example, the posterior describes a state of inconsistent information, obtained by several disagreeing measurements, it has a bi- or multi-modal shape and more care has to be taken in its summary. In general, a summary of the posterior should only be carried out for the interpretation of the final results, for successive uses as prior distribution it should be characterized as completely as possible.

### 3.1.4. Marginalization

The following relation, which can be readily derived from the sum rule of probabilities, plays a such prominent role in plausible reasoning, that it is also known as the *marginalization rule*:

$$P(\vec{\theta}|\vec{D}) = \int P(\vec{\theta}, \vec{\eta}|\vec{D}) d\vec{\eta}. \quad (3.5)$$

Here, the parameters of the posterior  $P(\vec{\theta}, \vec{\eta} | \vec{D})$  of some data analysis are divided in two classes: the *parameters of interest*  $\vec{\theta}$ , and the set of parameters  $\vec{\eta}$ , which are important for the modelling of the data, but which are not of primary interest for the hypothesis under consideration\*. By the application of rule (3.5) the plausibility (encoded in the pdf) of different values for  $\vec{\theta}$  is obtained, regardless of the values of the components of  $\vec{\eta}$ . A typical example, where (3.5) is useful, is the treatment of calibration parameters describing the response of some experimental equipment.

Concerning the implementation of the likelihood there is no formal distinction between the two kinds of parameters, the difference is purely given by the current interest in the parameters. When the information about a component of  $\vec{\eta}$  is very comprehensive the pdf describing this parameter will be very peaked, approaching a Dirac- $\delta$  distribution in the limit of precise knowledge. In that case the integral in (3.5) is obtained by just inserting the respective value for  $\eta_i$ , effectively not treating the parameter probabilistically any more. Conversely, when the knowledge about a calibration constant is very vague, the integration will involve a broad range of values  $\eta_i$  and the influence to the parameters of interest will produce a broadened distributions for  $\vec{\theta}$ . This kind of uncertainty propagation is able to take into account all interdependencies between the model parameters and different kinds of prior knowledge about the components of  $\eta_i$  are able to be treated, as will be described below.

The marginalization rule also describes the relation between parameter estimation and hypothesis testing. The plausibility of a hypothesis to be valid given the experimental evidence is calculated by fully marginalizing its posterior as a function of the parameters:  $P(H | \vec{D}) = \int P(H(\vec{\theta}) | \vec{D}) d\vec{\theta}$ .

### 3.1.5. Entropy and the Maximum Entropy Principle

As introduced above, the plausibility interpretation of probability theory means that a pdf  $P(\theta)$  represents the available knowledge or *information* about a proposition under consideration. In 1948 it was shown by Shannon, that there exists a measure for the *amount* of information contained in a discrete probability distribution: When a system is in one of  $n$  possible states, and our knowledge about the system is encoded in  $n$  probabilities  $p_i$ , each quantifying the plausibility of the system being in state  $i$ , then the *uncertainty* of our knowledge is given by  $H(p_i)$ :

$$H(p_1, \dots, p_n) = -k \sum_{i=1}^n p_i \log(p_i) \quad (3.6)$$

where  $k$  is an arbitrary constant, which allows to freely choose the base of the logarithm. The *information* encoded in a set of  $p_i$  is given by the difference between the entropy of the state with greatest uncertainty  $H(p_i = \frac{1}{n})$  and  $H(p_i)$ . The functional form of  $H$  was derived by Shannon from a set of assumptions, the most important of which is the assumption of consistency, requiring to obtain the same value for  $H$  for different ways of combining the elements  $p_i$  together<sup>43</sup>.

The basic idea of the maximum entropy (MaxEnt) principle is to use this measure of information to find a set of probabilities which is consistent with a certain prior information and carries the least amount of information. The prior information, which can be incorporated has to be *testable* information<sup>40</sup>. This means that for every set of probabilities it must be possible to state whether it is compatible with the testable information or not. By using the least informative of all possible sets of information, no additional information is introduced. The respective set is obtained, by maximizing the entropy  $H$  subject to certain constraints of the form  $f(p_i) = 0$ , given by the available prior information. The property of not introducing additional information is obviously

\*These additional parameters are frequently called *nuisance* parameters.

desirable, as the inference about the quantity of interest should only be based on the explicitly stated information.

In physical parameter estimation problems, the quantities of interest are most of the time continuous quantities. The generalization of (3.6) to the continuous case, sometimes called the Shannon-Jaynes entropy, as discussed e.g. in Ref. (2) is:

$$H_c(p(\theta)) = - \int p(\theta) \ln \left\{ \frac{p(\theta)}{m(\theta)} \right\} d\theta \quad (3.7)$$

The quantity  $m(\theta)$ , which can be interpreted as the state space density of the  $\vec{\theta}$ , ensures that the entropy is invariant under parameter transformations  $\theta \rightarrow \theta'$ , because  $m$  and  $p$  transform in the same way. Jaynes proposes to use invariance arguments to assign  $m(\theta)$ , if a convenient group of transformations is present in the problem. By applying this idea to the case of translational and scale invariance, the important cases of non-informative priors, given by the flat and the Jeffrey's prior<sup>2</sup> can be obtained. It can be seen here, that the determination of non-informative priors cannot be separated from the formulation of the problem, i.e. the invariance properties of data model and likelihood. Although in practical applications  $m(\theta)$  is frequently assumed to be constant, its general role is still a matter of ongoing research.

An interesting perspective in this context is discussed in Ref. (44) where the connection between the maximum-entropy prior and the likelihood is made explicit by maximizing the entropy of the *posterior* distribution:

$$P(\vec{\theta}|\vec{D}) \propto P(\vec{D}|\vec{\theta})P(\vec{\theta}). \quad (3.8)$$

The least informative posterior is obtained by varying the prior  $P(\vec{\theta})$ . The entropy to be maximized is then given by:

$$H = - \int d\vec{D} d\vec{\theta} P(\vec{D}|\vec{\theta})P(\vec{\theta}) \log \frac{P(\vec{D}|\vec{\theta})P(\vec{\theta})}{m(\vec{D})g^{1/2}(\vec{\theta})}, \quad (3.9)$$

where the state space density now consists of the two terms  $g^{1/2}(\vec{\theta})$  and  $m(\vec{D})$ . The density of the parameters  $\theta$  is set to the determinant  $g^{1/2}(\vec{\theta})$  of the Fisher Rao metric of the *likelihood*:

$$g_{ij} = \int d\vec{D} P(\vec{D}|\vec{\theta}) \frac{\partial \log P(\vec{D}|\vec{\theta})}{\partial \theta^i} \frac{\partial \log P(\vec{D}|\vec{\theta})}{\partial \theta^j}. \quad (3.10)$$

The state space density of the data  $m(\vec{D})$  can not be specified without information about the physical system being investigated. In Ref. (44) it is argued, that when the often used approximation of a Gaussian likelihood is applicable, a constant  $m(\vec{D})$  is a reasonable choice, and the translational invariant constant prior is obtained as a special case of an entropic prior.

Other recent works, go in the direction of unifying the principles of inference taking into account testable information and observed data<sup>45,46</sup> and thus revealing the Maximum Entropy principle and Bayes rule as special cases of a more general approach.

### 3.1.6. Maximum Entropy Priors

Despite the mentioned conceptual discussions about the assignment of ignorance priors, in the present analysis the practical approach was followed to set  $m(\vec{\theta})$  to a constant, in order to be able to assign maximum entropy priors on the basis of the testable information. Technically the entropy is maximized using the method of Lagrangian multipliers. The calculation is demonstrated for the case of just the trivial constraint  $\sum_{i=1}^M p_i = 1$ , leading to the following equation for the differential

of the function to be maximized (Lagrangian multiplier  $\lambda$ ):

$$d \left[ - \sum_{i=1}^M p_i \ln(p_i/m_i) - \lambda \left( \sum_{i=1}^M p_i - 1 \right) \right] = 0. \quad (3.11)$$

By writing the differential as  $d = \sum_i \frac{\partial}{\partial p_i} d$  on obtains:

$$\sum_{i=1}^M (-\ln(p_i/m_i) - 1 - \lambda) dp_i = 0,$$

which can only be fulfilled if all  $p_i$  equal the  $m_i$  multiplied by a constant value (given by the Lagrangian multiplier):

$$p_i = m_i e^{-(1+\lambda)},$$

and in the case of constant  $m_i$ s the normalization of the  $p_i$  leads to

$$p_i = 1/M \quad (3.12)$$

When generalizing this result to the continuous case  $M$  goes to infinity and the  $p_i$  vanishes. This can be circumvented by introducing a lower and upper bound  $a$  and  $b$ , leading to the normalized uniform prior given in table 3.1. There also the other priors used in the present analysis are summarized together with the underlying constraints.

**Table 3.1.:** Maximum Entropy distributions for different kind of testable Constraints

constraints		Distribution
$\int p(\theta) d\theta = 1$	Uniform	$p(\theta) = \frac{1}{b-a}$
$\int p(\theta) d\theta = 1$ $\int \theta p(\theta) d\theta = \theta_1$	Exponential	$p(\theta \theta_1) = \frac{1}{\theta_1} e^{-\theta/\theta_1}$
$\int p(\theta) d\theta = 1$ $\int (\theta - \theta_1)^2 p(\theta) d\theta = \theta_2^2$	Gaussian	$p(\theta \theta_1, \theta_2) = \frac{1}{\sqrt{2\pi}\theta_1} e^{-(\theta-\theta_1)^2/2\theta_2^2}$

### 3.1.7. The Implementation of a Data Analysis

The practical implementation of a data analysis based on the ideas outlined above, can be broken down to a list of tasks that have typically to be taken care of. The presentation of the current data analysis problem also follows this list, compare also chapter 6.

**Problem Statement** Formulation of the considered proposition and implementation of a model for the measured data.

**Likelihood** Examination of the error statistics of the measurement, formulation of the likelihood of the data.

**Priors** Consideration of the available knowledge about all parameters and numerical values used in the forward model, selection of probabilistic parameters, assignment of priors.

**Posterior** Characterization of the Posterior: analytical marginalization, Monte Carlo Sampling.

**Summary** The quantities of interest have to be either condensed in a few numbers for human inspection or comprehensively summarized for incorporation in further analysis.

### 3.1.8. Monte Carlo methods

The formal result of equation (3.3) is the multi-dimensional posterior pdf  $p(\vec{\theta}|\vec{D})$ . It encodes all information, which was included in the analysis by:

- the choice of the parameterization of the model,
- the prior pdfs for the model parameters,
- and the actual data.

The final (human) evaluation and interpretation of the result requires suitable characterizations of the often high-dimensional posterior function. To obtain any summary of the posterior, it needs to be evaluated at a number of points  $\vec{\theta}_i$  covering the domain of the posterior to some extent. When the number of components of  $\vec{\theta}$  is as low as three or four, the characterization can be done in an intuitive way, by scanning  $p(\vec{\theta}|\vec{D})$  on a predefined grid and summarizing the results by a graphical representation. Quite often however, the data model is more complex and the number of employed parameters is considerably greater. The immediate problem which arises is, that the cost of an algorithm exploring the whole parameter space is proportional to its volume, i.e. grows exponentially with dimension  $N$  of the parameter space:  $\mathcal{O}(a^N)$ , where  $a$  is the number of grid-points per dimension.

In *Monte Carlo* (MC) methods, the points  $\vec{\theta}_i$  at which the posterior is to be evaluated, called *samples*, are chosen *randomly*<sup>†</sup>. The beneficial effect of this randomness is, that it makes the convergence rate *independent* from the number of dimensions of the problem. This can be seen for example, when comparing the error-estimate of a numerical integration of a  $N$  dimensional function  $f$  using standard numerical (i.e. grid-based) and Monte Carlo integration: the error of the integral  $\sigma_{MC}$  obtained by MC sampling is inversely proportional to the square root of the number of function evaluations  $m$ . This square root  $m$  dependence on the number of samples is a general property of Monte Carlo algorithms<sup>48</sup>:

$$\sigma_{MC} \propto \frac{1}{m^{0.5}}. \quad (3.13)$$

When trying to use standard numerical quadrature rules to obtain an  $N$  dimensional integral, the integration has to be recursively decomposed into integrations with decreased dimension. For the sake of simplicity, only the error of the last integration is considered here. For the usual quadrature rules, there are analytical formulae giving an upper bound for the error of the integration as a function of the number of the support points per dimension  $a$ . For the trapezoidal rule, for example,

---

<sup>†</sup>In allusion to games of chance, the term *Monte Carlo* was first used in the 1940s by physicists working on nuclear weapon projects in the Los Alamos National Laboratory<sup>47</sup>.

the error bound is proportional to  $1/a^2$ . By expressing this in terms of the number of overall function evaluations  $m = a^N$  the following expression is obtained:

$$\sigma_{\text{num}} \propto \frac{1}{m^{2/N}}. \quad (3.14)$$

It can be seen from this heuristic argument, that for low dimensional problems (i.e. one or two dimensional) standard numerical integration converges more rapidly. With increasing number of parameters however, MC integration becomes more and more advantageous.

The human assessable representation of the posterior typically involves the computation of integral quantities. In general, the quantity to be inferred is a function of the model parameters  $f(\vec{\theta})$ . In the simplest case  $f$  may be just a component of the parameter vector, but frequently the quantity of physical interest is not identical to a numerical convenient parameterization of the problem and  $f(\vec{\theta})$  is a non-trivial function. If the data being analyzed allow to make an unambiguous statement (i.e. the posterior is uni-modal), what is a desirable situation, then the result of the data analysis can be summarized by giving the best fitting model and some measure for the uncertainty of the fit. This can be achieved by computing expectation value and the variance of the function  $f(\vec{\theta})$  whose pdf is given by the posterior<sup>‡</sup>:

$$\langle f \rangle = \int f(\vec{\theta}) \cdot P(\vec{\theta}|\vec{D}) d\vec{\theta}. \quad (3.15)$$

$$\sigma_f^2 = \langle f^2 \rangle - \langle f \rangle^2 = \int f^2(\vec{\theta}) \cdot P(\vec{\theta}|\vec{D}) d\vec{\theta} - \langle f \rangle^2. \quad (3.16)$$

If there are more than one quantities of interest  $f_i(\vec{\theta})$ , the correlations between the  $f_i$  may be non-vanishing. They can be obtained in analogous way as mean and variance. As mentioned, the description of the quantities of interest in terms of their expectation value and covariance matrix is comprehensive for uni-modal posteriors and corresponds to a multi-dimensional Gaussian fit to the posterior (also called Laplace approximation<sup>40</sup>).

If the posterior has a more complex structure, it is often helpful to consider graphical representations of (possibly multi-dimensional) distributions instead of mean and covariance of the quantities of interest.

If the (multi-modal or high order correlated) structure of the posterior is spread out over more parameters of interest than are graphically representable, its adequate interpretation may get tedious. A sensible utilization of such a posterior could be the combination with additional information (e.g. from independent measurements, as used in the combined analysis of different plasma diagnostics). In that case, either a representation using multi dimensional histograms or a combined sampling of the product of both likelihoods is conceivable.

In any case, the implementation of each of the above mentioned characterizations can be carried out, if there is a method available to draw samples  $\vec{\theta}^i$  distributed according to the posterior

<sup>‡</sup>Relation (3.15) can be formally obtained, by considering the pdf  $P(f)$  as the total marginal over the pdf for  $f$  and  $\vec{\theta}$ . The emerging  $P(f|\vec{\theta})$  is given by the Dirac  $\delta$  function because the value of  $f$  is known as the function  $f(\vec{\theta})$  of the model parameters:

$$\begin{aligned} P(f) &= \int P(f, \vec{\theta}) d\vec{\theta} & \langle f \rangle &= \int f \cdot P(f) df \\ &= \int P(f|\vec{\theta}) \cdot P(\vec{\theta}|\vec{D}) d\vec{\theta} & &= \int f(\vec{\theta}) \cdot P(\vec{\theta}|\vec{D}) d\vec{\theta} \quad \square \\ &= \int \delta(f - f(\vec{\theta})) \cdot P(\vec{\theta}|\vec{D}) d\vec{\theta} \end{aligned}$$

When the integration over  $f$  is carried out the  $\delta$  function vanishes and  $f$  is replaced by  $f(\vec{\theta})$ .

$p(\vec{\theta}|\vec{D})$ . The distributions of the quantities of interest  $f_i(\vec{\theta})$  can be obtained from the set of samples  $\{\vec{\theta}^i\}_{i=1}^m$  by just calculating the  $f_i$  for each sample and the expectation value  $\langle f(\vec{\theta}) \rangle$  can be obtained from

$$\tilde{f} = \frac{1}{n} \sum_{i=1}^m f(\vec{\theta}^i), \quad (3.17)$$

accordingly. (Multi-dimensional) distributions can be depicted in the form of histograms of the quantities of interest  $f_i$ .

The simplest way to obtain samples distributed according to the posterior  $P(\vec{\theta}|\vec{D})$  is the *simple sampling* approach sketched above: A random number is drawn uniformly from the domain of the posterior and weighted the value of the posterior  $P(\vec{\theta}|\vec{D})$ . The problem here is, that a high dimensional probability distribution  $P(\vec{\theta})$  is often concentrated in an extremely small region of its domain, called the *typical set*  $T$ , whose volume can be estimated using  $|T| \simeq 2^{H_{SG}(\vec{\theta})}$ , where  $H_{SG}(\vec{\theta})$  is the Shannon-Gibbs entropy of  $P(\vec{\theta})$ ,

$$H_{SG}(\vec{\theta}) = \sum_{\vec{\theta}} \log_2 \frac{1}{P(\vec{\theta})}. \quad (3.18)$$

There are more sophisticated MC sampling algorithms, e.g. *importance sampling* and *rejection sampling* (see e.g. Ref.<sup>48</sup>), which are designed to sample more efficiently from the typical set of the posterior. Although these methods may be appropriate in problems of moderate complexity, their general drawback is, that they make use of an approximative pdf, or an envelope pdf respectively, that are hard to assign properly in high dimensional problems.

### Markov Chain Monte Carlo Methods

In general<sup>48</sup>, it is tedious to effectively create *independent* samples from a high dimensional probability distribution. Instead, the undesired evaluation of the posterior outside the typical set can be avoided, by starting from a point lying in the typical set and exploring  $P(\vec{\theta})$  using a random walk like scanning procedure. The length scale of the random walk can be adapted to the size of the typical set in each dimension. By this method, which is the basis for *Markov chain* based MC algorithms, a sequence of states  $\{\vec{\theta}^{(t)}\}$  is generated, where each sample is generated from a probability distribution, that depends on the previous state  $\{\vec{\theta}^{(t-1)}\}$ . It can be shown, that it is possible (and actually even simple) to construct a Markov chain which has the property, that the distribution of its samples converges to a designated stationary distribution  $P(\vec{\theta})$ . It is important to keep in mind, that the correlation of subsequent samples may make it necessary to run the chain for a considerable time, before a number of effectively independent samples are generated. Moreover, multi-modal posteriors, for which the typical set is split in different regions have to be treated with special care, because the algorithm is unlikely to make transitions between distant modes. The careful choice of the initial states is of special interest in this case. See e.g. Ref. (<sup>49-51</sup>), for a comprehensive introduction into Markov chain Monte-Carlo methods)

A Markov chain is a discrete stochastic process, i.e. a sequence of random variables  $\{\vec{\theta}^{(t)}\}$ , which has the property that it can be generated from the conditional distribution of state  $\vec{\theta}^{(t+1)}$  given only its preceding state  $\vec{\theta}^{(t)}$ :

$$T(\vec{\theta}^{(t+1)}|\vec{\theta}^{(t)}). \quad (3.19)$$

$T$  is called the transitional kernel of the Markov chain. The generability condition from the transitional kernel can be written as<sup>51</sup>:

$$P(\vec{\theta}^{(t+1)}|\vec{\theta}^{(t)}, \{\vec{\theta}^{(i)} : i = 0, \dots, t-1\}) = T(\vec{\theta}^{(t+1)}|\vec{\theta}^{(t)}) \quad (3.20)$$



In the following, only time-homogeneous Markov chains are considered, where the transitional kernels does not depend on  $t$ . It can be shown, that under quite general conditions the samples generated from a Markov chain are distributed according to an invariant distribution, which is called the stationary distribution  $\pi(\vec{\theta})$ . As a special case, Markov chains, which satisfy the condition of *detailed balance* possess a stationary distribution and their sample will also converge to it regardless of the choice of the initial state  $\vec{\theta}^{(t=0)}$ . The detailed balance condition is:

$$\pi(\vec{\theta}^{(t)})T(\vec{\theta}^{(t+1)}|\vec{\theta}^{(t)}) = \pi(\vec{\theta}^{(t+1)})T(\vec{\theta}^{(t)}|\vec{\theta}^{(t+1)}). \quad (3.21)$$

This expression implies, that every possible state can be reached by the chain. The Metropolis Hastings algorithm is an example for an algorithm satisfying condition (3.21). There exist also Markov chains which don't obey detailed balance, but nevertheless have a stationary distribution. It can be shown, that a transitional kernel which is positive for all states is sufficient for the existence of  $\pi(\vec{\theta})$ . See e.g. Ref. (51) for a comprehensive discussion of different Markov chain Monte-Carlo (MCMC) algorithms.

### The Metropolis Hastings Algorithm

The idea of Markov chain based sampling was invented together with the first digital computers, at times when programming computers was performed not even using punchcards, but with electronic plugboards<sup>52</sup>. The first publication<sup>53</sup> reporting results obtained using a MCMC (in the form, now known as Metropolis algorithm) was printed 1953. Hastings<sup>54</sup> generalized the Metropolis algorithm to the form which is presented below, some 20 years later.

For a target distribution  $\pi(\vec{\theta})$ , which can be computed up to a normalizing constant, the Metropolis-Hastings algorithm yields a sequence of samples  $\{\vec{\theta}^{(t)}\}$ , whose distribution converges to the target distribution. The basic principle of the algorithm is to generate a candidate for each successive sample using a *proposal distribution*  $q(\vec{\theta}^{(t+1)}|\vec{\theta}^{(t)})$  and accepting the candidate with a probability given by the *acceptance probability*  $\alpha(\vec{\theta}^{(t+1)}|\vec{\theta}^{(t)})$ . The acceptance probability is a functional of the desired stationary distribution  $\pi(\vec{\theta})$  (Equation 3.23) This way, the sample candidates can be drawn from a distribution which allows for an efficient numerical generation of random numbers. When the candidate is rejected, the successive sample is given by the current sample, and a new candidate is generated. The distribution  $\pi(\vec{\theta})$  has to be evaluated at each candidate point.

The transitional kernel corresponding to the algorithm reads:

$$T(\vec{\theta}^{(t+1)}|\vec{\theta}^{(t)}) = q(\vec{\theta}^{(t+1)}|\vec{\theta}^{(t)})\alpha(\vec{\theta}^{(t+1)}|\vec{\theta}^{(t)}), \quad (3.22)$$

where the acceptance probability is given by:

$$\alpha(\vec{\theta}^{(t+1)}|\vec{\theta}^{(t)}) = \min \left\{ 1, \frac{\pi(\vec{\theta}^{(t)}) \cdot q(\vec{\theta}^{(t)}|\vec{\theta}^{(t+1)})}{\pi(\vec{\theta}^{(t+1)}) \cdot q(\vec{\theta}^{(t+1)}|\vec{\theta}^{(t)})} \right\}. \quad (3.23)$$

The chosen proposal density does not influence the stationary distribution of the Markov chain. The rate of convergence, however, can depend crucially on the combination of proposal and desired target distribution. The implementation of a proposal distribution leading to rapid mixing of the chain depends on craftsmanship and experimentation. Nevertheless, untuned canonical forms of proposal distributions may perform well in some cases. It is often convenient to choose a proposal distribution, which generates each component of  $\{\vec{\theta}^{(t)}\}$  independently, reducing the class of proposal distributions to be considered to the one-dimensional case. Heavy tailed proposals, like e.g. the Cauchy distribution, often improve the mixing rate in the presence of a structured target

density which is not perfectly unimodal. The width of the proposal distribution in each dimension is usually adapted to the desired stationary distribution: A large *step-width* leads to a faster random walk, but this applies only when the candidates are accepted, which gets improbable for a too large step-width. As a matter of experience, good mixing is often obtained by adjusting the step-width to the value, where roughly one third of the proposed candidates are accepted by the algorithm.

### Convergence of Markov Chain Monte-Carlo

The inference from the serially correlated set of samples generated using a Markov chain Monte-Carlo algorithm requires some care. If the number of computed iterations of the algorithm is too small, the distribution of the samples may be grossly unrepresentative of the target distribution. Generally, the inference from correlated draws from a distribution is far less precise, than from the same number of independent draws. The early iterations of the Monte-Carlo are still characteristic of the starting approximation of the simulation, rather than the target distribution. The samples of the so called *burn-in* phase can not be used for the characterization of the target distribution. The length of the burn-in depends on the degree of serial correlation of the parameter. Various methods to assess the convergence can be found in literature, see for example<sup>55,56</sup> for reviews of the topic.

In the present analysis, the autocorrelation of the time series of each element of the parameter have been considered, as well as a method to assess the convergence of scalar estimators described in<sup>50</sup>.

The autocorrelation quantifies the statistical dependence of the values of a time-dependent function at different points in time. It allows to assess the number of Monte-Carlo steps that are needed, before an effectively independent sample is obtained. The autocorrelation  $R_k$  of a discrete time series  $\{\theta^{(t)}\}$  is given by the following expression:

$$R_k = \frac{1}{(n-k)\text{Var}(\theta)} \cdot \sum_{t=1}^n (\theta^t - \text{E}(\theta))(\theta^{t+k} - \text{E}(\theta)), \quad (3.24)$$

where  $\text{Var}(\theta)$  is the variance and  $\text{E}(\theta)$  the sample mean of the parameter.  $k$  is called the *time-lag*.  $\theta$  might be an element of the parameter vector or any scalar estimate deduced from the sampled parameters. The autocorrelation of a time series obtained by MCMC can typically be described by an exponentially decaying function of time-lag:

$$R_k \sim e^{-\kappa k} \quad (3.25)$$

Where  $\kappa$  is called the autocorrelation *length*. When equation (3.25) applies, the autocorrelation length can be estimated from the samples of the time series and the autocorrelation can be characterized by its decay length  $\kappa$ . See Appendix B, for the formulae that were used for the estimation of the autocorrelation length by non-linear regression, in the present analysis.

The sampling can usually be regarded as converged, when the number of samples is large compared to the autocorrelation length. The correlation lengths of the elements of the parameter vector may differ strongly.  $\kappa$  allows a quick identification of parameters that may need to be monitored more closely.

The authors of<sup>50</sup> propose a convergence criterion that is applicable, when multiple Monte-Carlo chains were run in parallel: The between- and within-sequence variance can be used to monitor the convergence of a scalar estimand  $\theta$ . The draws from  $J$  parallel sequences of length  $n$  are labeled as  $\theta^{(ij)}$  ( $i = 1..n$ ,  $j = 1..J$ ). Then, the *between-sequence* variance  $B$  and the *within-sequence* variance

$W$  can be obtained using the following expressions:

$$B = \frac{n}{J-1} \sum_{j=1}^J (\bar{\theta}^{(\cdot,j)} - \bar{\theta}^{(\cdot)})^2, \quad \text{where } \bar{\theta}^{(\cdot,j)} = \frac{1}{n} \sum_{i=1}^n \theta^{(ij)}, \quad \bar{\theta}^{(\cdot)} = \frac{1}{J} \sum_{j=1}^J \bar{\theta}^{(\cdot,j)}$$

$$W = \frac{1}{J} \sum_{j=1}^J s_j^2, \quad \text{where } s_j^2 = \frac{1}{n-1} \sum_{i=1}^n (\theta^{(ij)} - \bar{\theta}^{(\cdot,j)})^2.$$

The variance of  $\theta$  distributed according to the stationary distribution  $\pi(\vec{\theta})$  of the Monte-Carlo chain can be estimated using a weighted average of  $W$  and  $B$ :

$$\widehat{\text{Var}}^+(\theta) = \frac{n-1}{n}W + \frac{1}{n}B.$$

Which overestimates the variance, assuming the starting values of the chain were appropriately dispersed. At the same time, the within-sequence variance  $W$  should be an under-estimate of the variance of  $\theta$ , as the individual sequence may not have covered the whole typical set. The convergence of the sampling is validated by computing the ratio of the both, which approaches one if convergence is accomplished:

$$\sqrt{\widehat{R}} = \sqrt{\frac{\widehat{\text{Var}}^+(\theta)}{W}}. \quad (3.26)$$



## 4. Experiment

### 4.1. Setup

The experimental setup of the spectroscopic measurement (Fig. 4.1) is simple and inexpensive. It consists of a dc glow-discharge, a simple imaging optic and a miniature optical-fiber-spectrometer observing the emitted light. The response of the spectrometer as a function of wavelength was calibrated by replacing the discharge tube with a standard light source in an Ulbricht sphere.

The electric circuit used to operate the glow-discharge is shown in Fig. 4.1. The anode which is connected to the positive pole of the high-voltage power supply lies on ground potential. The ohmic resistor which is connected in series with the discharge is used to stabilize its negative current-voltage characteristics. The current of the discharge is conveniently measured at the anode side of the circuit which is at ground potential.

For measurements at several different spatial positions, the discharge tube was mounted on a movable support with a millimeter scales in horizontal and vertical direction. This way, the calibrated optical setup could be left in position, reducing the number of necessary calibrations of the setup.

#### 4.1.1. Optical Setup

The light from the positive column of the discharge was imaged onto the optical-fiber of the spectrometer, using a single plano-convex lens with a focal length of 15 cm. The opening angle of the cone of the line of sight is much smaller than depicted in Fig. 4.1. An iris diaphragm is used to adjust the amount of light for convenient detection by the spectrometer.

#### 4.1.2. Spectrometer

The spectrometer that was used is a commercially available Czerny-Turner type spectrometer produced by Ocean Optics<sup>57</sup> which can be read out digitally. Of the two spectral channels for

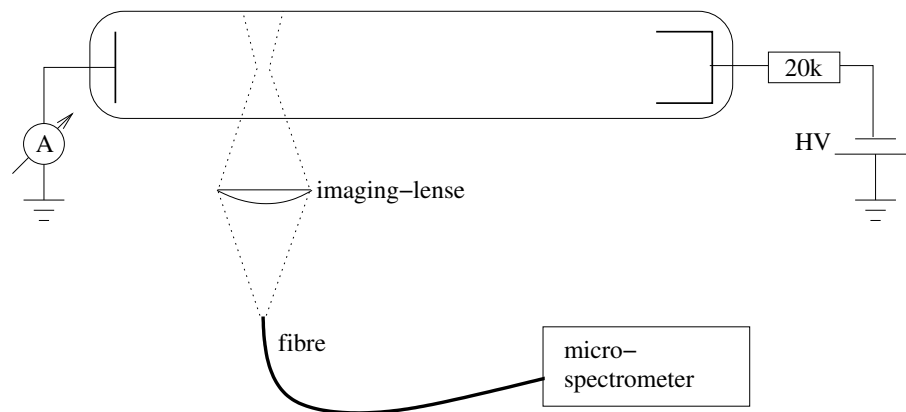


Figure 4.1.: Experimental setup of the spectroscopic measurement.

the ultraviolet wavelength-range (UV, 247..573nm) and visible and near infrared range (NIR, 475..1121 nm) only the NIR channel was used for the measurement.

The slit width of 50  $\mu\text{m}$  and the fixed grating with 600 lines/mm (UV: 1200 lines/mm) determine the spectral resolution of roughly 2nm (UV: 1 nm). A cylindric convex lens is used to image the entrance slit height of 600  $\mu\text{m}$  onto the detector, which has got a height of 200  $\mu\text{m}$ . The detector of the UV channel is coated with a low-pass filter which has got a cutoff wavelength that varies as a function of pixel number (wavelength). The filter allows for the suppression of effects of second order radiation on all pixels. The low-pass filter coating on the NIR channel has got a constant cutoff wavelength, which leads to a deterioration in the range of  $\lambda > 920\text{nm}$  by additional radiation from second order of interference. The detectors of the spectrometer are two rows of silicon-CCDs, each having 2048 Pixels with a size of  $14 \times 200 \mu\text{m}^2$ . The charges read out of the pixels are digitized by a 1 MHz A/D converter with a dynamic range of 12 bit. The mapping of wavelengths to pixel-numbers of each spectrometer channel is implemented using a second order polynomial:

$$\lambda_i = \lambda_0 + \lambda' \cdot i + \lambda'' \cdot i^2, \quad (4.1)$$

see table 4.1 for the approximate values of the used coefficients. The wavelength mapping is obtained from the neon emission spectra considered in the present analysis by incorporating the parameters of equation (4.1) in the probabilistic model (cf. 5.9 and 6.3.6).

**Table 4.1.**

	$\lambda_0$ [nm]	$\lambda'$ [nm]	$\lambda''$ [nm]
UV	242.85	0.18365	$-1.10 \cdot 10^{-5}$
NIR	466.06	0.36625	$-2.241 \cdot 10^{-5}$

## 4.2. Calibration with the Standard Light Source

The response of the spectrometer as a function of wavelength was calibrated by replacing the discharge tube (Fig. 4.1) with a standard light source in an Ulbricht sphere. The spectral radiance of the standard light source is known from a reference measurement. In Fig. 4.2, the spectral radiance of the standard source is shown together with the response of the spectrometer. The light bulb in the standard source emits predominantly in the visible and near infrared region. The intensity drops for wavelengths smaller than 350nm. This poses no problem, as the part of the neon spectrum which is described by the plasma model is located between 550 and 900nm.

### 4.2.1. Uncertainty of the Spectral Measurement

The formulation of the probabilistic model, described in chapter 5), requires precise knowledge about the reproducibility of the measured data. The error statistics of the spectral measurement is given by the noise of the CCD chip, which consists of two contributions: the photon noise  $\sigma_{\text{ph}}$  and the readout noise  $\sigma_{\text{ro},i}$ . The photon noise is caused by the statistical incidence of photons at the detector. It follows photon statistics and  $\sigma_{\text{ph}}$  is proportional to the number of photo-electrons generated in the CCD. The readout noise was assumed to be independent of the signal amplitude and the same for all pixels. Consequently, the noise of the signal obtained by a CCD sensor

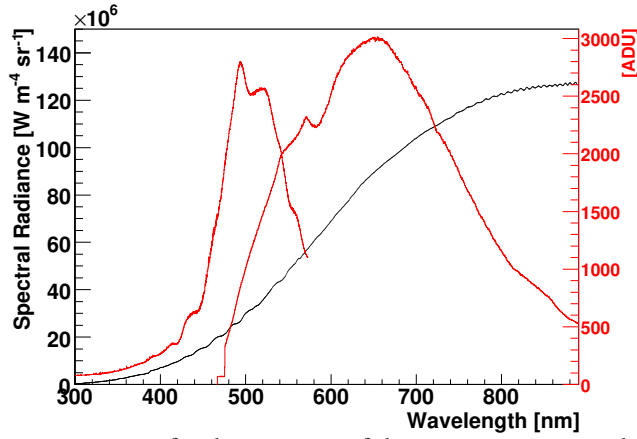


**Figure 4.2.:** Calibration measurement for the response of the two spectrometer channels. The black curve shows the spectral radiance of the standard source, as known from the reference measurement. The red curves depict the response of the spectrometer (UV + NIR).

depends on the amplitude  $D_i - D_{\text{dark},i}$  in the following way<sup>2</sup> :

$$\sigma_{\text{spec},i}^2 = E_\gamma \cdot (D_i - D_{\text{dark},i}) + \sigma_{\text{ro}}^2. \quad (4.2)$$

The conversion factor  $E_\gamma$  is equal to the inverse number of photon electrons per ADU. Experimentally the dependence of the variance  $\sigma_{\text{spec},i}^2$  on the signal amplitude was determined from repeated measurements of the spectrum of the standard light source. The variance of each pixel of the spectrum of the standard light source was plotted against  $D_i - D_{\text{dark},i}$ . The parameters of equation (4.2) were fitted to the data in Fig. 4.3, with the following result:

$$E_\gamma \approx \frac{1}{28.5}, \quad \sigma_{\text{ro}}^2 \approx 5.72 \text{ ADU}^2.$$

$$E_\gamma \approx \frac{1}{16.2}, \quad \sigma_{\text{ro}}^2 \approx 9.01 \text{ ADU}^2.$$

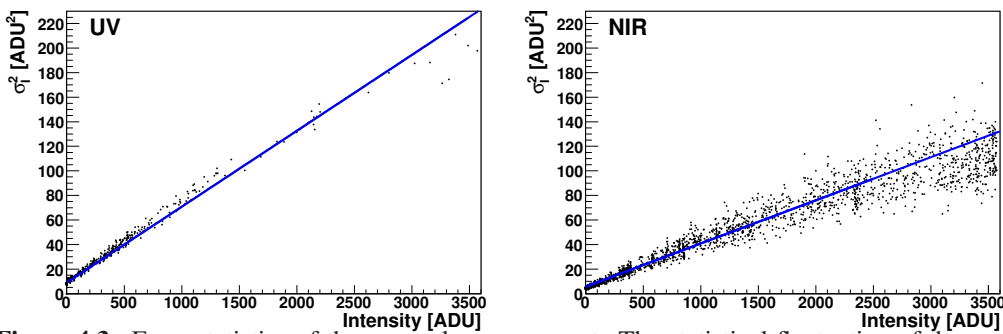


**Figure 4.3.:** Error statistics of the spectral measurement. The statistical fluctuation of the spectrometer is obtained by repeated measurements of the spectrum of the standard light source. It is described by counting statistics (Poisson distribution,  $\sigma^2 \propto I$ ). The variance  $\sigma_{\text{spec},i}^2$  is obtained from 100 exposures and is shown as a function of the intensity measured in analog-to-digital units. The straight line is fitted to data in the range from 0 to 2500 ADU.





## 5. Data Model

The Data Model is a simulation  $\vec{D}_{\text{sim}}(\vec{\Theta})$  of the experimental data for a given set of model parameters  $\vec{\Theta}$ . The forward model is the basis for the reconstruction of the EEDF, which is basically an inversion of the forward model, resulting in (a set) of model parameters consistent with a given measured spectrum  $\vec{D}$ . The forward model on its own, is not of probabilistic nature. It is combined with the errors statistics of the measurement in the likelihood, as described in 6.2, which constitutes a probabilistic model of the data. In order to take advantage of the full information content of the measured spectrum, the present forward model describes the raw data, i.e., the intensities of the different spectrometer pixels, rather than deduced quantities such as line intensities.

### 5.1. Overview

The model  $\vec{D}_{\text{sim}}(\vec{\Theta})$  for the spectroscopic data consists of a stationary collisional-radiative model (CRM) revealing the population densities  $n_i$  of excited states and ions in the discharge plasma and a description of the spectroscopic measurement. The chain of the different elements of the forward calculation can be summarized as follows:

$$f_e(\vec{\Theta}_f) \xrightarrow{\text{CRM}} n_i \xrightarrow{\text{lifetime} \cdot \frac{A_{ij}\hbar\omega}{4\pi}} \epsilon_{ij} \xrightarrow{\text{radiation transport} \int_{\text{l.o.s.}} dV} L_{ij} \xrightarrow{\text{line shape} \otimes s(\lambda)} L_\lambda \xrightarrow{\text{calibrations}} \vec{D}_{\text{sim}}. \quad (5.1)$$

The EEDF  $f_e(\vec{\Theta}_f)$ , which depends on the subset  $\vec{\Theta}_f$  of the model parameters, enters the CRM. The calculated population densities  $n_i$  are multiplied by the inverse lifetime of the excited states  $A_{ij}$  (Einstein coefficient) times the photon energy  $\hbar\omega$  and the inverse of the full solid angle  $(4\pi)^{-1}$  to obtain the *locally emitted power*  $\epsilon_{ij}$  [ $\text{W}/(\text{m}^3 \cdot \text{sr})$ ]. The radiation has to pass through the plasma before it leaves the discharge device. The apparent lifetime of the excited states is affected by the transport of photons if the absorber density is high, e.g., for transitions to the ground state of the atom<sup>30</sup>. Together with the integration along the line-of-sight (l.o.s.) of the spectrometer, the description of this opacity results in the *effective radiance*  $L_{ij}$  of each transition.

The line intensities given by the effective radiance have to be convoluted ( $\otimes$ ) with the line shape  $s(\lambda)$  to obtain the *effective spectral radiance*  $L_\lambda$ . The observed line shape is determined by a convolution of the apparatus function with the natural line shape, which is determined by broadening mechanism like Doppler- or impact broadening (cf. 2.2.1). For the present model of the overview spectrometer, the line shape is dominated by the apparatus function, which was obtained here from distinct lines in the spectrum as described in 5.8.

The modeling of the spectrometer output furthermore comprises the description of the response per incident power of each pixel (intensity calibration, cf. 4.2) and the mapping of pixel numbers onto wavelengths (wavelength calibration, cf. 5.9).

## 5.2. Collisional Radiative Model of the Neon Discharge

The population densities of the atomic states  $n_i$  were described by a set of balance equations accounting for all *elementary processes* populating or de-populating an atomic level  $i$  (equation 5.2). Ions were treated as an additional state. With a few exceptions, the rates of the elementary processes are proportional to the population density of another excited state (cf. 2.2.1). This was used for the solution of the following system of coupled equations for the stationary case:

$$\begin{aligned}
 0 \stackrel{!}{=} \frac{dn_i}{dt} = & \underbrace{n_e \left[ \sum_{k \neq i} (\langle \sigma_{ki}^e v_e \rangle n_k - \langle \sigma_{ik}^e v_e \rangle n_i) \right]}_{\text{Electron (de-)excitation}} + \underbrace{\left[ \sum_{k > i} \Lambda_{ki} A_{ki} n_k - \sum_{k < i} \Lambda_{ik} A_{ik} n_i \right]}_{\text{Radiative transitions}} \dots \\
 & + \underbrace{n_a \left[ \sum_{k \neq i} \langle \sigma_{ki}^a v_a \rangle n_k - \sum_{k \neq i} \langle \sigma_{ik}^a v_a \rangle n_i \right]}_{\text{Atom collisions}} \dots \\
 & - \underbrace{n_e \langle \sigma_{i\infty}^e v_e \rangle n_i}_{\text{Electron impact ionization}} - \underbrace{\langle \sigma_{ii}^a v_a \rangle n_i^2}_{\text{Chemo-ionization}} \dots \\
 & + \underbrace{n_e (\beta_{\text{rad}} + \beta_{\text{DE}}) n_\infty}_{\text{Recombination}} - \underbrace{\Gamma_i n_i}_{\text{Wall de-excitation}} \quad (5.2)
 \end{aligned}$$

The rate coefficients of radiative transitions which are not optically thin (see also below) and the rate coefficients for chemo-ionization were calculated by iteratively solving the linearized system of equations.

*Electron excitation and de-excitation.* The transition rate is given by the rate coefficient  $n_e \langle \sigma v \rangle = n_e \int_0^\infty \sigma(E) E^{1/2} f_e(E) dE$  multiplied by the density of atoms in the initial state of the excitation. Different parameterizations of the energy distribution  $f_e(\vec{\Theta}_f)$  are employed to determine electron collision rates for the CRM. See also 6.3.2 for a description of the used excitation-cross-sections.

*Radiative transitions.* For optically thin transitions, the transition rate is given by the Einstein coefficient  $A_{ki}$ . The escape factor  $0 < \Lambda_{ki} \leq 1$  accounts for the radiation transport in optically thick regimes. Its computation is described below. See also 6.3.2 for a description of the used coefficients.

*Atom collisions.* Collisions of the excited atoms with neutral gas atoms lead to excitation transfer between metastable and resonant states of neon, which have the lowest excitation energy among the excited states. The calculation of the rate coefficient is analogous to the electron excitation but much simplified since the atoms are a Maxwellian ensemble at room temperature. The rate coefficient for the respective transitions were taken from Ref. <sup>(58)</sup>

*Electron impact ionization.* The charge carrier balance is determined by ionization. Only singly charged neon ions are taken into account. The cross-sections were taken from Ref. <sup>(59,60)</sup>

*Chemo-ionization.* The energy of two excited neon atoms is greater than the ionization energy. Therefore collisions between excited atoms may lead to ionization of one of the atoms, while

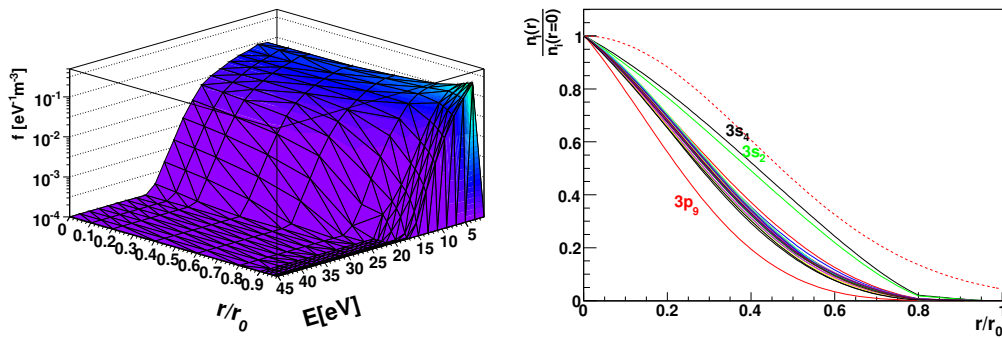


**Figure 5.1.:** The radial variation of the EEDF as obtained by a hybrid model<sup>13</sup> (left) and the radial variation of the 30 excited states considered in the CRM (right, see 2.4.1 for the notation), which was obtained with the EEDF depicted on the left;  $r_0$  is the radius of the discharge tube. The red dotted line is the radial variation of an effective states considered in Ref. (13), as shown in Fig. 5.2. The profiles of the 27 states of the model, that have a very similar radial dependence are not labelled, the color code for the states is the same as in Fig. ???. States  $3s_4$  and  $3s_2$  are metastable.

the other atom returns to the ground state. The rate coefficient for the chemo-ionization of two metastable atoms was taken from<sup>61</sup>.

*Wall de-excitation.* Excited atoms or ions coming into contact with the wall of the discharge tube are de-excited to the ground state. The flux  $\Gamma_i$  was obtained by considering diffusion of the excited atoms and ambipolar diffusion of the ions in the plasma.

### 5.3. Spatial Dependence of the Plasma Model

#### 5.3.1. Coordinate System

The vessel of the glow discharge is cylindrically symmetric. The coordinate system used to describe the plasma is chosen accordingly: the  $z$ -axis is given by the axis of the discharge tube and the whole system is azimuthally symmetric.

In order to model the line averaged spectroscopic measurement, the emissivity of the plasma volume which is imaged onto the optical fiber, has to be integrated to obtain the radiance of the plasma surface. As the line-of-sight of the spectrometer is chosen perpendicular to the discharge axis, the axial extension of the imaged volume is small:  $600\ \mu\text{m}$  at the axis and  $1.5\ \text{mm}$  at the walls of the tube\*. Accordingly, the *axial* variation of plasma parameters can be neglected in the model. Also, the axial resolution of axial scans is  $1\ \text{mm}$ . The *radial* variation of the population densities and the emissivity, however, has to be accounted for in the model, as the line-of-sight extends over the whole radial range. In the present implementation, the radial variation is described using predetermined, fixed radial profiles:

$$n_i(r) = n_i \cdot n_i^r(r) \quad (5.3)$$

\*Following from the magnification of the optics (which is  $1 : 1$ ), the diameter of the fiber ( $600\ \mu\text{m}$ ) and the the double-conical form of the volume, which leads to a broadening of  $600\ \mu\text{m}$  or  $1000\ \mu\text{m}$  depending on the diameter of the discharge tube.

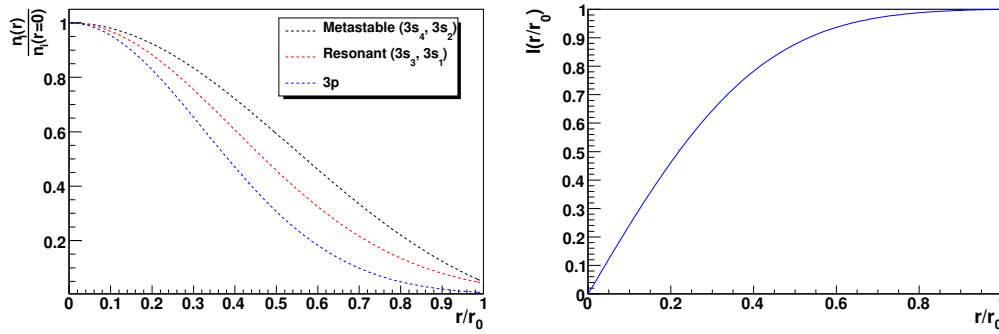


**Figure 5.2.:** The radial variation of three of the five effective states considered in Ref. <sup>(13)</sup> (left). The variation of the resonant 3s states is also shown in Fig. 5.1 for comparison. The integrated population density  $I(r/r_0)$  (equation 5.4) demonstrates the small fraction of light emitted from the outer part of the discharge: less than 5% are emitted are  $r/r_0 > 0.65$ .

The following considerations are the basis for the choice for the form of the radial profiles: In the simplest case, under the assumption of diffusion dominated radial transport, the profile form is given by a zeroth order Bessel Function (in cylindrical symmetry <sup>15</sup>).

The excitation profiles obtained by a 1-dimensional self-consistent kinetic model of the cylindrical glow discharge in neon <sup>13</sup>, however, show a somewhat different behavior. Uhrlandt <sup>13</sup> obtains radial profiles for five *effective* excited state densities. The metastable  $3s_4$  and  $3s_2$  states and the resonant  $3s_3$  and  $3s_1$  states are each described by a combined state, and the ten elements of the 3p multiplet are also treated as a combined state. The profiles of these states are shown in Fig. 5.2. In order to obtain multiplet-resolved profiles, the radial variation of the EEDF given by Uhrlandt <sup>13</sup> is fed to the current collisional-radiative model. In Fig. 5.1 the radially resolved EEDF is shown, as well as the resulting radial profiles for the 30 excited states considered in the present model. The red, dashed curve shows the profile obtained by <sup>13</sup> for the combined  $3s_3$  and  $3s_1$  state for comparison. Note, that although not well visible in the plot, the slope of the multiplet-resolved profiles vanishes for  $r = 0$ , as required for a continuously differentiable density profile.

The obtained multiplet resolved profiles and the profiles of Uhrlandt show a somewhat different radial variation. On the other hand, the metastable ( $3s_4$  and  $3s_2$ ) states show a broader profile in both cases. In the multiplet resolved calculation, all states except the state  $3p_9$  show a very similar radial profile. They are not labelled in the plot, since the lines overlap partly. The only state with a noticeable narrower profile is the state  $3p_9$ . This is consistent with the dependence of the population density on the EEDF (cf. 7.1.5) depicted in Fig. ???. The state  $3p_9$  shows also a different behavior there, in that it gets depopulated by an increase of the EEDF at low energies. In order to validate the robustness of the model against different choices of the radial profiles, the reconstruction of the EEDF was performed for both sets of profiles shown in Fig. 5.1 and Fig. 5.2 (cf. 7.1.3).

### 5.3.2. Line Averaging of the EEDF

The spectroscopic measurement of the light emission from the plasma is averaged along the line-of-sight of the spectrometer. As shown in Fig. 5.1 the EEDF is not constant as function of radius (i.e. along the line of sight), but is shifted to lower energies by the radial electric field in front of the glass tube. In the right part of Fig. 5.2, the integrated population density  $I$ , is shown for the

effective 3p state, which is obtained from the following expression:

$$I(r) = \frac{\int_0^r n_i^r(r') dr'}{\int_0^{r_0} n_i^r(r') dr'}. \quad (5.4)$$

$I(r)$  is proportional to the fraction of light emitted at radii smaller than  $r$ . It can be observed, that only 5% of the emitted light come from the outer part of the discharge ( $r/r_0 > 0.65$ ). Therefore, the change of the EEDF close to the wall of the discharge only leads to a very small change of the observed spectrum.

## 5.4. Parameterizations of the EEDF

The parameterization used to implement the EEDF in the reconstruction is a Maxwellian distribution multiplied by a correcting function :

$$F_M(E) = \underbrace{2 \sqrt{\frac{E}{\pi(kT_e)^3}} \exp\left\{\frac{-E}{kT_e}\right\}}_{\text{Maxwellian}} \times \underbrace{\exp\{f_{\text{Spline}}(E)\}}_{\text{correction}}. \quad (5.5)$$

The correction allows for the description of EEDFs that deviate from Maxwellian distributions, as expected from independent kinetic modeling<sup>13</sup>. The correction was implemented using splines of different order: A linear spline is advantageous in that it doesn't tend to oscillate and overshoot the data, while a cubic interpolation allows for an overall better description. The exponential of the spline was taken to assure positivity of the EEDF.

Note, that the parameterization  $F_M(E)$  is not normalized to unity. In principle, a normalized implementation is easily possible:

$$\tilde{F}_M(E) = \frac{F_M(E)}{\int_0^\infty F_M(E) dE}. \quad (5.6)$$

In the forward model, the EEDF is always multiplied by the electron density. Using a normalized parameterization of the EEDF allows an implementation of the product  $N_e \cdot \tilde{F}_M$ , where the numerical parameter  $N_e$  directly gives the electron density. Such a physically clear parameterization, though, has an unfavorable influence onto the convergence of the Monte-Carlo sampling (cf. 7.1.4). Better results are obtained by multiplying  $F_M(E)$  by a rough estimate of the electron density and using only the values of the correcting spline and the electron temperature as free parameters of the model. In this case, the actual electron density corresponding to a set of parameters has to be obtained by integration.

The number of knots used for the correcting spline influences the flexibility of the parameterization. Results for different numbers of knots are shown in 7.1.5.

## 5.5. Optical Depth of Resonance Transitions

As described in 2.2.1, resonance radiation may be re-absorbed by atoms in the final state of the respective transition. The radiation transport influences the collisional radiative model by changing the rates of several radiative decays and also affects the amount of light leaving the plasma and reaching the spectrometer. The re-absorption of photons yields an apparent enhancement of the

**Table 5.1.:** Symbols used in the formulae for the escape factors (equation (5.8) to 5.10)

Symbol	Description
$\tau_v$	natural time of life of transition: $1/A_{ki}$
$\lambda_0$	wavelength of emitted radiation
$N_0$	neutral gas density
$N_r$	reduced density $N_r = N_0 \lambda_0^3$
$h$	radius of discharge tube
$H_r$	reduced radius $H_r = \frac{h}{\lambda_0}$
$a_{v0}$	Voigt parameter
$\nu_0$	line center frequency
$c$	speed of light
$k_B$	Boltzmann's constant
$T$	gas temperature
$M$	atomic mass
$P_c$	probability of dephasing collision
$g_l/u$	statistical weight of lower/upper state

lifetime  $\tau_i = (\sum_j A_{ij})^{-1}$  of the excited state, which can be quantified using the escape factor  $\Lambda_{ki}$ :

$$A'_{ki} = \Lambda_{ki} \cdot A_{ki}, \quad 0 < \Lambda_{ki} \leq 1 \quad (5.7)$$

Approximate models of the radiation transport in discharge tubes were developed in Ref. (30). Empirical formulae are used to summarize the results of a large number of Monte-Carlo simulations of radiation transport in cylindrical discharge tubes<sup>30</sup>. The formulae (equation (5.8) to 5.10) take into account the geometrical dimensions of the discharge and the atomic data of the respective transition. They were employed in the present model for transitions to the *ground state*:

$$(A_t \tau_v)_{dm} = \frac{1.575 + \frac{\sqrt{a_{v0}}}{2.75} + \frac{0.22 \ln^{1.3}(1.0 + 2.75 a_{v0}^{3/2} Z)}{0.35 + \sqrt{a_{v0}}}}{1.575 + \frac{\sqrt{a_{v0}}}{2.75} + Z \sqrt{\ln(1.0 + \frac{Z}{\sqrt{\pi}})}} \quad (5.8)$$

$$(A_t \tau_v)_{rcm} = \left( \frac{P_c a_{v0} N_r^{3/4} H_r^{1/4}}{a_{v0} N_r^{3/4} H_r^{1/4} + 0.92} \right)^{0.15} \frac{0.196}{\sqrt{H_r}} \quad (5.9)$$

$$\Lambda = \sqrt{(A_t \tau_v)_{dm}^2 + (A_t \tau_v)_{rcm}^2}. \quad (5.10)$$

(The used symbols are summarized in table 5.1)

Voigt parameter and probability for a dephasing collision are obtained from the expressions given below, the Voigt parameter in that form is valid only in the limit of low gas density:

$$a_{v0} = \frac{1}{4\pi \nu_0 \tau_v \sqrt{\frac{2k_B T}{Mc^2}}}, \quad P_c = \left( 1 + \frac{65.71 g_l}{N_0 \lambda_0^3 g_u} \right)^{-1}. \quad (5.11)$$

In table 5.2 typical values for the escape factors of transitions to the ground state are given, which are obtained for a ground state density of  $2.1 \cdot 10^{22} [\text{m}^{-3}]$ , corresponding to 89 Pa.

**Table 5.2.:** Escape factors of transitions to the ground state

Initial State	Escape Factor $\Lambda_{ki}$
3s <sub>3</sub>	0.00044
3s <sub>1</sub>	0.00025
4s <sub>3</sub>	0.00070
4s <sub>3</sub>	0.00047
3d <sub>11</sub>	0.0011
3d <sub>7</sub>	0.00039
3d <sub>1</sub>	0.00095

### 5.6. Optical Depth of Transitions to Metastable States.

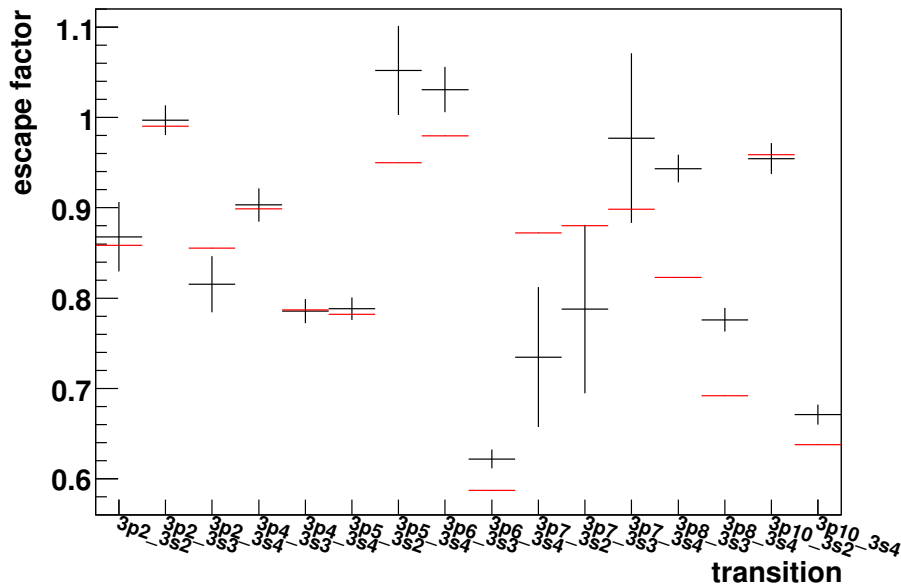


**Figure 5.3.:** Escape factors of different transitions to states in the 3s multiplet. The black points with error bar are extracted from line ratios in a measured spectrum, while the red lines are escape factors obtained from equation (5.8) to (5.10) using effective densities as described in the text.

The next-to highest populated states of the neon atoms are states of the 3s multiplet, in particular the metastable states 3s<sub>4</sub> and 3s<sub>2</sub> which have a negligible radiative decay rate<sup>†</sup> Their density is sufficiently high to cause an optical depth of transitions to these states. The formulae (5.8) to (5.10) used for the escape factors to the ground state are not directly applicable here, since the absorber density is not spatially homogeneous. They can be used, however, to obtain lower limits

<sup>†</sup>Their de-population is caused by electron impact de-excitation, collisions of the metastables with the glass tube, and collisional transfer to resonant states.

for the escape factors by inserting the radial *maximum* of the respective population density (The escape factor is a monotonically increasing function of the population density). The resulting lower limit is as low as 0.1 for some transitions, indicating the necessity of an incorporation of radiation transport of these transitions.

In order to obtain escape factors for the radially varying population densities of the 3s states, *effective* absorber densities were introduced. The population density of the states 3s<sub>4</sub>, 3s<sub>3</sub>, and 3s<sub>2</sub> as obtained from the CRM is multiplied with a correction factor, which is fitted to the measured spectra in the inversion procedure. It can be expected, that the fitted correction factors roughly reflect the ratio between average and maximum density of the radial profiles, and this is indeed the case. In table 5.3 typical escape factors to states in the 3s multiplet are summarized.

In Fig. 5.3 an independent way to obtain some of the escape factors of the transitions to the 3s multiplet is summarized: Transitions to the least populated of the 3s state are approximately optically thin. This fact can be used to obtain the population densities of states in the 3p multiplet that have a transition to 3s<sub>1</sub> from line intensities in a measured spectrum. From the population intensities, obtained this way, and the intensities of lines to other states in the 3s multiplet, escape factors can be extracted. Escape factors extracted from a measured spectrum in this way are shown together with escape factors obtained using equation (5.8) to (5.10) with *three* effective densities for the 3s states. Although the quantitative agreement is not perfect, it can be seen:

1. That the escape factors of several of the shown transitions deviate significantly from one.
2. The overall behavior of the fitted and computed escape factors is similar.

For two transitions, the fitted escape factors are slightly greater than one, indicating an underestimation of the population density from the line to 3s<sub>1</sub>. The error bars of the escape factors of the 3p<sub>7</sub> lines are fitted with a great error bar, because the line of the transition 3p<sub>7</sub> → 3s<sub>1</sub> has a strong overlap with the strong 3p<sub>10</sub> → 3s<sub>4</sub> - line.

In conclusion, Fig. 5.3 gives a strong indication, that the description of the radiation transport of transitions to 3s states using the escape factor approximation of Ref. (30) with effective densities is appropriate.

**Table 5.3.:** Escape factors for transitions to the 3s<sub>i</sub> states. The escape factors are omitted for spectral lines, which have a negligible intensity and can not be found in NIST<sup>37</sup>

Escape Factors $\Lambda_{ki}$	3s <sub>4</sub>	3s <sub>3</sub>	3s <sub>2</sub>
3p <sub>10</sub>	0.51	0.98	0.97
3p <sub>9</sub>	0.2	—	—
3p <sub>8</sub>	0.61	0.88	—
3p <sub>7</sub>	0.92	0.94	0.85
3p <sub>6</sub>	0.41	0.99	—
3p <sub>5</sub>	0.98	1	0.69
3p <sub>4</sub>	0.81	0.96	—
3p <sub>3</sub>	—	0.97	—
3p <sub>2</sub>	0.89	1	0.85
3p <sub>1</sub>	—	1	—



## 5.7. Line-of-Sight Integration.

The contribution  $L_{ij}$  of the transition  $j \rightarrow i$  to the overall radiance of the plasma surface<sup>‡</sup> has to be obtained by an integration of the local emissivity  $\varepsilon_{ij}(s, r_{\perp})$  of that transition along the line-of-sight (l.o.s.):

$$L_{ij} = \int ds \frac{1}{A_{\perp}(s)} \int dA_{\perp} \varepsilon_{ij}(s, r_{\perp}), \quad (5.12)$$

in which  $A_{\perp}(s)$  is the area perpendicular to the line-of-sight of the plasma volume, which is imaged onto the optical fiber.  $A_{\perp}(s)$  depends on the position  $s$  along the l.o.s. and is computed taking into account the area of the optical fiber, the opening angle of the optics, and the magnification of the imaging optics. Equation (5.12) can be regarded as the average of  $\varepsilon_{ij}$  over the area  $A_{\perp}(s)$ , which is integrated with respect to  $s$ . In Fig. 5.4 the imaged volumes of different lines-of-sight are shown.

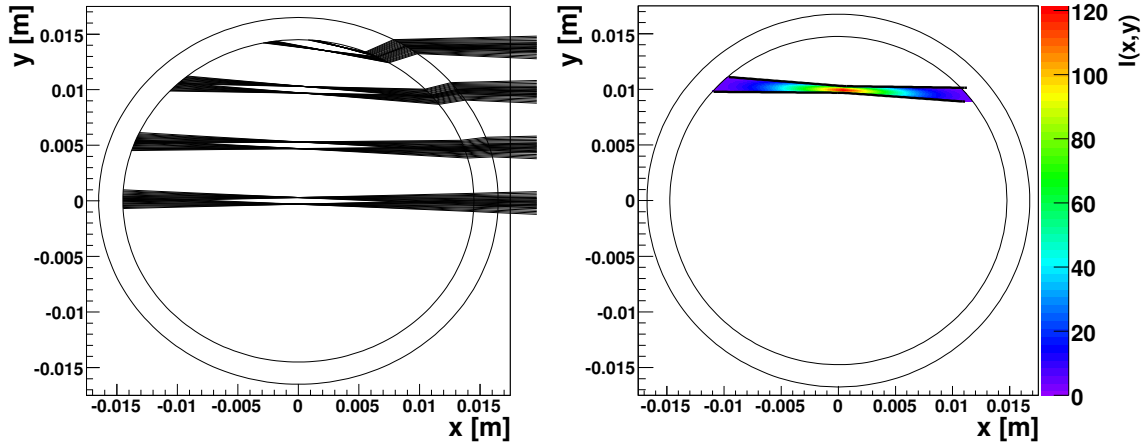


Figure 5.4.: and  $I(x,y)$

For each l.o.s. a number of rays covering the angular range, which is imaged onto the optical fiber is shown. The diffraction in the glass of the plasma tube is taken into account (the employed formulae are given in Appendix C). It can be seen, that for l.o.s. which are close to the upper tube wall, the shape of the emitting plasma volume is changed.

Because the direction of the line-of-sight is chosen perpendicular to axis of the glass-cylinder, the change of shape of the emitting volume appears only in the  $x$ - $y$ -plane. Consequently, the area  $A_{\perp}$  has got an elliptical shape.

By writing down equation (5.12) in the Cartesian coordinates used in Fig. 5.4 the expression:

$$L_{ij} = \int dx dy dz \frac{\varepsilon_{ij}(\sqrt{x^2 + y^2})}{A_{\perp}(x,y)} \quad (5.13)$$

is obtained. Because of the assumption of axial homogeneity along the emitting volume (cf. 5.3) and the line-of-sight being perpendicular to the  $z$ -axis, the integrand in equation (5.13) has no

<sup>‡</sup>The wavelength dependence is obtained by convolution with the transfer function as described in 5.8.

explicit  $z$ -dependence and the integration along the  $z$ -axis can be done analytically:

$$\begin{aligned}
 L_{ij} &= \int dx dy \int_0^{\frac{R_a}{R_b} \sqrt{R_b^2 - y^2}} dz \frac{\varepsilon_{ij}(\sqrt{x^2 + y^2})}{A_{\perp}} \\
 &= \int dx dy \underbrace{\frac{R_a}{R_b} \sqrt{R_b^2 - y^2} \varepsilon_{ij}(\sqrt{x^2 + y^2})}_{=I(x,y)} \frac{1}{A_{\perp}}.
 \end{aligned} \tag{5.14}$$

Here,  $y'$  is the distance of the point in the  $x$ - $y$ -plane, where the integrand is computed, to the center of the line-of-sight (cf. Fig. C.2). The elliptical  $A_{\perp}$  is characterized by the major and minor radius  $R_a$  and  $R_b$ . The quantities  $A_{\perp}$ ,  $y'$ ,  $R_a$ , and  $R_b$  all depend on  $x$  and  $y$ . The expressions used for their computation are given in Appendix C.

The integrand  $I(x, y)$  of equation (5.14) is shown in Fig. 5.4 (right part). The integration is performed using a Gaussian quadrature in two dimensions (as described e.g. in Ref. ( ? )).

## 5.8. Apparatus Function

The effective spectral radiance  $L_{\lambda}(\lambda)$  as introduced in equation (5.1) can be regarded as the intensity distribution of the light after passing the dispersing grating of the spectrometer. It is obtained by convolving the actual spectral radiance of the plasma  $L_{\text{plasma}}(\lambda)$  with the apparatus function  $s_a$ . The difference between  $L_{\text{plasma}}(\lambda)$  and  $L_{\lambda}(\lambda)$  is, that the former reflects the physical distribution of the emitted light as a function of the wavelength, while the latter is determined by the response of the employed spectrometer. The convolution with the apparatus function reads:

$$L_{\lambda}(\lambda) = \int L_{\text{plasma}}(\lambda') s_a(\lambda - \lambda') d\lambda'. \tag{5.15}$$

Since the width of the apparatus function is large compared to the line broadening effects in the plasma<sup>§</sup>, the natural broadening may be neglected and the line shape is given by the mere apparatus function  $s = s_a$ . In the present model, the effective spectral radiance was obtained by summing up the radiance of each transition  $L_{ij}$  multiplied by the line shape:

$$L_{\lambda}(\lambda) = \sum_{ij} L_{ij} s(\lambda - \lambda_{ij}), \tag{5.16}$$

where  $\lambda_{ij}$  is the wavelength of the light emitted by the respective transition.

**Determination of the Apparatus function** In first approximation, the apparatus function of a spectrometer using a grating as its dispersive element can be described by a Gaussian function (cf. Fig. 5.7). The deviations from a Gaussian apparatus function are shown in Fig. 5.6. Although the apparatus function looks similar to a Gaussian, the deviation is quite significant when expressed in units of the statistical error of the spectral measurement.

In order to model the form of the function with higher precision, splines were used which were fitted to measured line profiles. For this purpose, well-separated spectral lines at different wavelengths were shifted and rescaled, and a smoothing spline was fitted to all points of the superimposed lines. As there are not enough well separated lines in the neon spectrum, additional spectra

<sup>§</sup>Typical line widths in a low pressure discharge plasma are  $\mathcal{O}(10)$  pm, mainly determined by Doppler-broadening<sup>29</sup>, the resolution of the spectrometer in the range of visible light is  $\Delta\lambda \simeq 1$  nm.

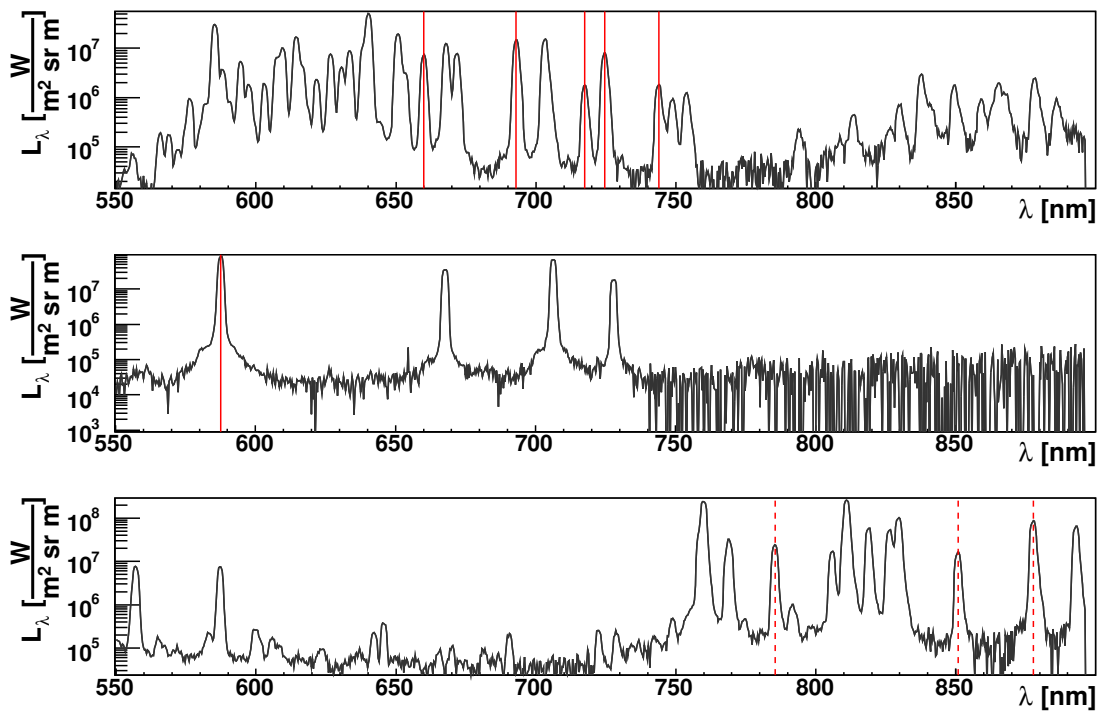


**Figure 5.5.:** Spectral lines (red lines) used to determine the apparatus function of the spectrometer. The spectra were obtained from discharges in neon, helium and krypton (top to bottom). The lines in the krypton spectrum, marked with dashed lines are used for the determination of apparatus function at high wavelengths.

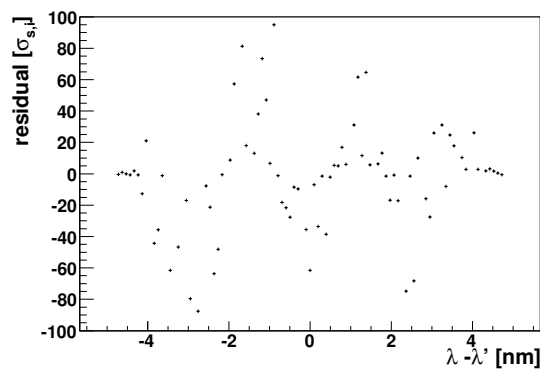


**Figure 5.6.:** The residuals between different measured spectral lines and a Gaussian apparatus function is shown as function of the position relative to the line center  $\lambda - \lambda'$  in units of standard deviations. Although the deviations from a Gaussian are small on an absolute scale, the residuals are large because of the small statistical error of the spectral measurement.

from discharges in krypton and helium were used for the determination of the apparatus functions. As discussed in 7.1.1, the consistence of measured and modelled spectrum is not perfect at higher wavelength ( $\lambda \gtrsim 750$  nm). Because the distribution of the residuals indicated a variation of the apparatus function for high wavelengths, two different splines were used for the apparatus function at the different wavelength regimes. In Fig. 5.5 the spectra used for the determination of the appa-

ratus functions are shown and the employed lines are indicated. The dashed lines in the krypton spectrum were used for the fit of second apparatus function at high wavelengths.

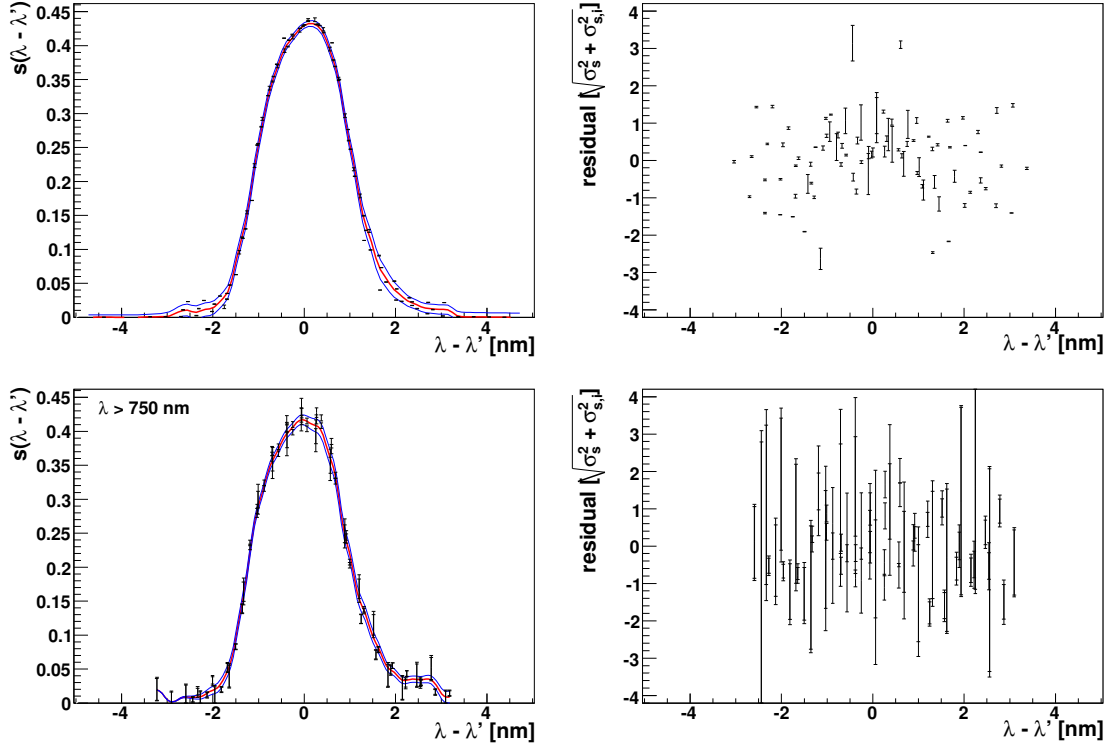


**Figure 5.7.:** The apparatus functions used at high (top) and low (bottom) wavelengths. For each apparatus function(left plot), the smoothing spline obtained by shifting and scaling different lines (red, see text) is shown with the assigned error band (blue) and the data points from the different lines. The right plots shows the residuals  $(s(\lambda_i - \lambda') - D_{s,i}) / \sqrt{\sigma_s^2(\lambda_i - \lambda') + \sigma_{s,i}^2}$ , (where  $\lambda_i$  is the position of the  $i$ th measurement of the apparatus function  $D_{s,i}$  (see also text)). The error bar of the residuals depicts the contribution of the uncertainty  $\sigma_{s,i}^2$  of the spectral measurement, which is rescaled by the combined error in the denominator of the residuals in order to match the units of the ordinate.

An error  $\sigma_s(\lambda - \lambda')$  was determined from the residuals of the smoothing spline fit. It quantifies the variation of the apparatus function for the different lines in the spectrum. (cf. 6.3, for the incorporation of this uncertainty in the analysis.) In order to obtain the uncertainty of the transfer function from the uncertain measured spectra, a probabilistic analysis was performed. The residuals of five adjacent data points  $D_{s,i}$ ,  $i = 1..5$  from the rescaled spectral lines were considered at a time, in order to estimate the uncertainty at the position of the middle point. Later, a smoothing spline is fitted to the obtained uncertainty as a function of  $\lambda - \lambda'$ .

The estimation of the uncertainty from each five adjacent data points uses the hierarchical model<sup>50</sup> summarized in Fig. 5.8. The position  $\lambda - \lambda'$  is omitted in the following for the sake of brevity. As the five data points may come from five different spectral lines, they are based on slightly different (unknown) apparatus functions  $s_i$  (as mentioned  $\lambda - \lambda'$  is fixed, here), which are assumed to be described by a normal distribution with mean  $s$  and standard deviation  $\sigma_{s,i}$ . The mean of the normal distribution is given by the smoothing spline, while  $\sigma_{s,i}$  is the sought variation of the transfer function. Because of the (known, Gaussian) uncertainty of the spectral measurements  $\sigma_{s,i}$ , the data points  $D_{s,i}$  obey an additional scattering around the  $s_i$ . As described in

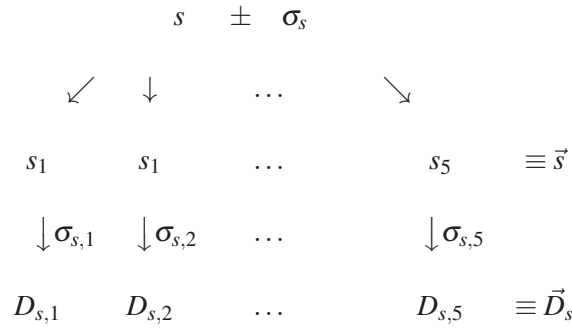


**Figure 5.8.:** The hierarchical model of the measurement of the apparatus function at a fixed  $\lambda - \lambda'$ : The apparatus function of different spectral lines varies with the unknown standard deviation  $\sigma_s$ . The different apparatus functions  $s_i$  are measured with the uncertainty  $\sigma_{s,i}$ , determined by the error statistics of the spectrometer.

Appendix A, a marginal probability distribution (cf. chapter 3) for the hyper-parameters  $s$  and  $\sigma_s$  can be obtained in closed form:

$$p(s, \sigma_s | \vec{D}_s) = \frac{1}{(2\pi)^{n/2}} \prod_{i=1}^n \left\{ \frac{1}{\sqrt{\sigma_s^2 + \sigma_{s,i}^2}} \exp \left( -\frac{s^2 - s_i^2 - 2sD_{s,i}}{2(\sigma_{s,i}^2 + \sigma_s^2)} \right) \right\}. \quad (5.17)$$

By maximizing<sup>¶</sup>  $p(s, \sigma_s | \vec{D}_s)$  for the given  $s$  with respect to  $\sigma_s$ , an estimator for the uncertainty of the apparatus function is obtained. In Fig. 5.7 the two resulting transfer functions are shown together with their respective error band. The residuals of the apparatus function are shown as a function of the wavelength position on the right of Fig. 5.7, and for the first apparatus function (low-wavelengths) their distribution is also shown as a histogram (cf. Fig. 5.9). It can be seen, that the distribution is symmetrically centered around zero for all wavelength, and the correct assignment of  $\sigma_s$  as a function of wavelength position is reflected in the distribution of the residuals having a variation of approximately one.

## 5.9. Calibration of the Spectrometer.

The description of the response of the CCD chip has to take into account the dark current  $D_{\text{dark},i}$  and calibration factor  $C_i$  for each pixel. The mapping of pixel numbers to wavelengths was implemented using a second-order polynomial:

$$D_{\text{sim},i} = C_i \cdot L_\lambda(\lambda_i) + D_{\text{dark},i}; \quad \lambda_i = \lambda_0 + \lambda' i + \lambda'' i^2. \quad (5.18)$$

The output of the used spectrometer  $D_{\text{sim},i}$  for each pixel  $i$  has a dynamic range of 12 bit and is expressed in analog-to-digital units (ADU).

The fluctuation of the dark current and the readout noise  $\sigma_{\text{ro},i}$  were determined by repeated measurements without light incidence. The parameters of the wavelength mapping  $\lambda_0, \lambda', \lambda''$  were fitted to the data together with parameters of the EEDF.

<sup>¶</sup>The maximum was found using an implementation<sup>2</sup> of Brent's algorithm, the algorithm is described e.g. in Ref. (?).

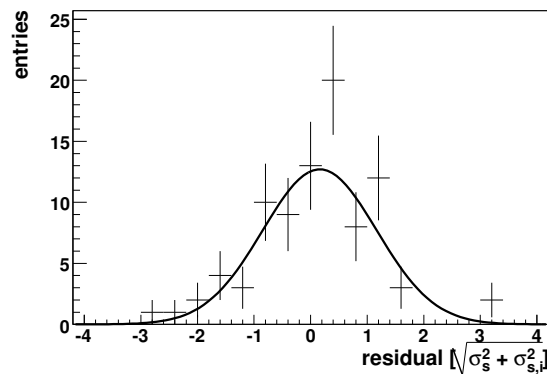


**Figure 5.9.:** Left: A histogram of the residuals of the apparatus function at low wavelengths (shown as a function of the wavelength position in the top right of Fig. 5.7) is shown together with a fit by a normal distribution (The uncertainty of number of entries is assumed to be described by Poisson statistics). The fitted normal distribution has mean value of  $0.15 \pm 0.13$  and a standard deviation of  $0.98 \pm 0.15$ .

The calibration factor was determined using a standard light source. The response of the CCD pixels  $s_i$ , when exposed to the spectral radiance  $L_s(\lambda_i)$  of the standard light source, was measured and  $C_i$  was computed:

$$C_i = \frac{T}{T_s} \frac{(s_i - D_{\text{dark},i})}{L_s(\lambda_i)}. \quad (5.19)$$

Here  $T$  and  $T_s$  are the exposure times of the spectral measurement of the plasma and the standard light source. As the calibration factor is the result of a measurement, it is also subject to statistical uncertainty with the standard deviation  $\sigma_{C,i}$ . Assuming independent and Gaussian-distributed noise of the spectral measurement, the uncertainty of  $C_i$  can be estimated using Gaussian error propagation:

$$\sigma_{C,i} = \frac{T}{T_s L_s(\lambda_i)} \cdot \sigma_{\text{spec},i}. \quad (5.20)$$

Here  $\sigma_{\text{spec},i}$  is the rms-variance of the spectral measurement of the standard light source (see also next section).

## 6. Analysis of Spectroscopic Data

In this chapter, the elements of the implementation of data analysis procedure are described. The data analysis was performed according to the integrated data analysis procedure as given in 6.2.

### 6.1. Problem Statement

Goal of the analysis is the reconstruction of the electron energy distribution function, which is most consistent with the measured spectroscopic data. A full forward model was specified in equation (5.1), mapping the EEDF  $f_e$  with onto a simulation of the simulated data  $\vec{D}_{\text{sim}}$ .

### 6.2. Likelihood

The likelihood  $P(\vec{D}|\vec{\Theta})$  states the probability to obtain the measured data  $\vec{D}$  given the parameter set  $\vec{\Theta}$ . It represents the statistical model of the measurement. The likelihood of each pixel  $D_i$  can be obtained from the value of the model  $D_{\text{sim},i}$  and the distribution of the statistical error of this pixel. In concordance with the principle of Maximum Entropy (cf. chapter 3), a Gaussian likelihood is appropriate when the estimates for the data value and its uncertainty are known. In that case, the likelihood of the data is given by:

$$P(\vec{D}|\vec{\Theta}) = \frac{1}{\prod_i \sqrt{2\pi\sigma_i^2}} \exp \left\{ -\frac{1}{2} \sum_i \frac{(D_i - D_{\text{sim},i})^2}{\sigma_{\text{eff},i}^2} \right\}. \quad (6.1)$$

**Effective Width of the Likelihood  $\sigma_{\text{eff},i}$ .** The uncertainty of the apparatus function  $\sigma_s(\lambda - \lambda')$ , which is most important for a proper description of the data, (cf. 5.8) and of the relative intensity calibration  $\sigma_{C,i}$  (cf. 5.9) were taken into account by using an effective width in the Gaussian likelihood:

$$\sigma_{\text{eff},i}^2 = \sigma_{\text{spec},i}^2 + \sigma_{C,i}^2 + \sum_{jk} L_{jk}^2 \sigma_f^2(\lambda_i - \lambda_{jk}). \quad (6.2)$$

This formulation is equivalent to the introduction of additional model parameters with Gaussian priors and subsequent marginalization, as derived in Ref. (?).

### 6.3. Priors

For all parameters treated in a probabilistic way, the prior pdfs  $P(\vec{\Theta})$  have to be specified. This means that the available knowledge about the respective parameter is quantified without taking into account the experimental data,

Generally speaking, there are two kinds of parameters that have to be described probabilistically: First, the *parameters of interest*, which are inferred from the data and are to be determined in the

inversion procedure. Second, parameters which we are not interested in, but whose values are not known precisely. In table 6.1 the parameters of the forward model and the assigned priors are summarized. The choice of the prior distributions is discussed in the following paragraphs.

**Table 6.1.:** Summary of the parameters  $\vec{\Theta}$  used in the forward model. Parameters, for which no prior is stated, are not treated probabilistically. The Gaussian priors of the line shape and the intensity calibration of each pixel are taken into account by the effective width of the likelihood (see text).

Symbol	Parameter Description	Remarks, Prior
$\vec{\Theta}_f$	Parameters of the EEDF	Flat prior
$N_e$	Electron density	Uniform prior
$\sigma_{ij}$	Scale of electron impact excitation cross sections	Gaussian prior
$A_{ij}$	Einstein coefficients	Gaussian prior
$D_m$	Diffusion coefficient of metastables	-
$D_I$	Ambipolar diffusion coefficient of Ions	-
$\Lambda_{ij}$	Escape factors (EF) of transitions to ground state	-
$C_{3s4/3s2}$	EF of transitions to the metastable levels	Flat prior for eff. densities
$p_{Ne}$	Gas pressure	-
$T_{Ne}$	Gas temperature	-
$r$	Diameter of the discharge tube	-
$n_{Duran}$	Refractive index of glass	-
$d$	Thickness of glass	-
$n_{5si,4di}$	Populations of unmodeled atomic levels	Exponential prior
$n_{3si,3p,3d,...}$	Radial profiles of the excited state densities	Gaussian prior
$s(\lambda)$	Line shape	Gaussian prior, analytic
$\lambda_0, \lambda', \lambda''$	Wavelength calibration	Uniform priors
$C_i$	Intensity calibration	Gaussian prior, analytic
$C_{scale}$	Scale of intensity calibration	Gaussian prior

### 6.3.1. Parameters of interest

For the parameters we are interested in no additional information was included in the analysis and flat prior distribution were employed. The parameterization of the EEDF is given in equation (5.5). Beneath the parameters of the equation (5.5), which are the electron temperature and the values of the spline nodes, also the electron density was extracted from the spectral data and a flat prior was used for  $N_e$ .

### 6.3.2. Atomic Data

For the electron excitation cross sections and Einstein coefficients, a dataset from semi-relativistic  $B$ -spline Breit-Pauli  $R$ -Matrix (BSRM) calculations was used. Details of these calculations can be found in Refs. (<sup>38,62</sup>). Briefly, they are based on a close-coupling description of  $e - Ne$  collisions, including the lowest (in energy) 31 target states. Using term-dependent, and hence non-orthogonal orbital sets, which were individually optimized for each target state of interest, allowed for a highly accurate target description with a relatively small number of configurations in the configuration-interaction expansion. The above data were chosen, since they represent a complete, and internally consistent, dataset for all transitions of interest.



Data for oscillator strengths from the same BSRM model were combined with those from the atomic line database NIST<sup>37</sup>. Where data from NIST are available, a weighted average of the Einstein coefficients was computed using the uncertainties stated by NIST and the ones described below. The cross sections for ionization of neon in the ground and excited states were taken from Ref. (59) and Ref. (60).

The uncertainties of the *electron-impact excitation cross sections* were incorporated using a single, energy-independent scale parameter for each cross section. This is a reasonable choice, since in BSRM calculations the energy dependence of the cross sections is known to be more reliable than the absolute scale<sup>63</sup>. The use of a single scale parameter also allowed for an efficient implementation in the model.

A log-normal distribution<sup>64</sup> was used as prior for the scale parameters. Its pdf is given by:

$$G_{\log}(x|\tilde{\mu}, \tilde{\sigma}) = \frac{e^{-(\ln x - \tilde{\mu})^2 / (2\tilde{\sigma}^2)}}{x\tilde{\sigma}\sqrt{2\pi}}; \quad (6.3)$$

$$\mu = e^{\tilde{\mu} + \tilde{\sigma}^2/2}; \quad \sigma_{\text{rms}} = (e^{\tilde{\sigma}^2} - 1)e^{2\tilde{\mu} + \tilde{\sigma}^2}$$

with an expectation value  $\mu$  and a rms-variance  $\sigma_{\text{rms}}$ . The relative width ( $\sigma_{\text{rms}}/\mu$ ) used is listed in table 6.2. The numbers were chosen according to details of the BSRM calculations and the available independent experimental validations of the cross sections (see Refs.<sup>38,62,67?</sup>).

**Table 6.2.:** Uncertainties of the excitation cross sections.

final state	$\sigma_{\text{rms}}/\mu$ of log-normal distribution (relative error)
2p <sup>5</sup> 3s $J = 1$	10%
2p <sup>5</sup> 3s $J = 2$	20%
2p <sup>5</sup> 3p	40%
2p <sup>5</sup> 4s	60%
2p <sup>5</sup> 3d	60%

The uncertainty of the *Einstein coefficients*  $A_{ij}$  was assessed by considering the results of the BSRM calculations in the length and the velocity form of the electric dipole operator. Since both should, in principle, yield the same result, the difference was used as an estimate for the uncertainty<sup>65</sup>. Figure 6.1 shows the relative difference between the results in the two forms of the dipole operator as a function of the absolute value of the Einstein coefficient. For small  $A_{ij}$ , the calculations are expected to be less accurate compared to stronger transitions. Consequently, the relative width of the prior distribution  $\sigma_{\text{rms}}/\mu$  in Fig. 6.1 was chosen depending on the value of  $A_{ij}$ . It is taken as large as the biggest relative difference for a certain value of  $A_{ij}$ , but never smaller than 10%. Where both numbers were available, a weighted average of the Einstein coefficients from the BSRM calculations and the NIST database<sup>37</sup> was computed.

### 6.3.3. Escape Factors to Metastable States

The effective densities of the metastable states (1s<sub>5</sub> and 1s<sub>3</sub>) were implemented by means of correction factors  $C_{3s4/3s2}$  to the densities obtained by the collisional-radiative model (cf. 5.6). These correction factors have to be smaller than unity, since the maximum of the population density is located in the center of the discharge, for which the CRM was calculated. A uniform prior distribution between  $0 < C_{3s4/3s2} < 1$  was used for the factors.

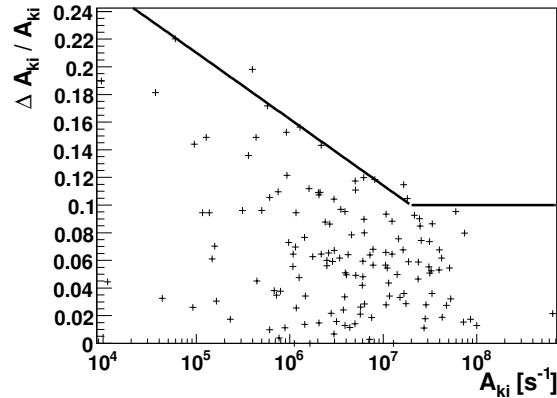


**Figure 6.1.:** Absolute value of the relative difference  $2|A_{ij,(v)} - A_{ij,(l)}| / (A_{ij,(v)} + A_{ij,(l)})$  between the BSRM results for the Einstein coefficients in the length and velocity form of the dipole operator plotted as a function of the absolute value of the Einstein coefficient. The straight line depicts the rms-width of the prior distribution as a function of the absolute value of the coefficient (see text).

#### 6.3.4. Population Densities of Unmodeled Levels

In the spectral range described by the forward model, there are a few lines originating from excited states, for which no cross-section data is available. In order to complete the forward model in these areas, the population densities of these states ( $4d_i$ ,  $5s_i$ ) were introduced as parameters of the forward model. The population densities are expected to be somewhat lower than the lower-lying states that are described by the CRM. In concordance with the MaxEnt principle<sup>41</sup>, exponential distributions were used as priors. The expectation value of the respective density was estimated using a Boltzmann factor for an electron temperature of 4 eV.

#### 6.3.5. Prior Distributions of the Radial Profile Integrals

An assumption about the radial profiles of the excited states populations is necessary for the line of sight integration. In order to account for the uncertainty of this assumption scale factors were introduced for the radial profiles. A log-normal prior distribution with expectation value of 1 and a rms-variance of 0.1 was used. The assignment of the rms-variance was based on the variation of the integral of the radial profiles for profiles taken directly from<sup>13</sup> compared to the multiplet-resolved computation described above.

#### 6.3.6. Priors of the Wavelength Calibration

The wavelength calibration is well determined by the data. Hence the posterior for  $\lambda$ ,  $\lambda'$ , and  $\lambda''$  is strongly dominated by the likelihood. Uniform prior distributions were used for the parameters of the calibration.

#### 6.3.7. Priors of the Absolute Intensity Calibration

In addition to the uncertainty of the calibration factors that is caused by the finite precision of the calibration measurement (cf. 5.9), there is an uncertainty in the (wavelength-integrated) radiance of the standard light source. The uncertainty of the calibration measurement of each pixel was incorporated in the effective width of the Gaussian likelihood (equation 6.2). The uncertainty

of the radiance, which is specified by the supplier of the standard light source (Labsphere Inc., <http://www.labsphere.com>), was taken into account by a scale parameter for the spectral radiance of the standard light source. A log-normal prior distribution with an expectation value of 1 and a rms-variance of 0.05 was used as prior.

### 6.3.8. Priors of the Apparatus Function

As described in 5.8, the apparatus function extracted from measured spectra is subject to uncertainty. This uncertainty was accounted for by the effective width of the Gaussian likelihood described above. The description with an effective likelihood is equivalent to the introduction of additional parameters with Gaussian prior distributions and a subsequent marginalization?

## 6.4. Focusing: Marginal Posterior Probability Distributions

The characterization of the posterior (equation 3.2), i.e. the numerical computation of estimators for the parameters of interest of the high dimensional pdf, is performed using a Markov chain Monte-Carlo (MCMC) algorithm, (cf 3.1.8).

In short, a Markov chain is a sequence of random variables  $\{\vec{\Theta}_1, \vec{\Theta}_2, \dots\}$  where the next state  $\vec{\Theta}_{t+1}$  is sampled from a distribution  $P(\vec{\Theta}_{t+1}|\vec{\Theta}_t)$ , called the transition kernel, which only depends on the current state of the chain  $\vec{\Theta}_t$ . A time-homogeneous Markov chain whose transition kernel does not depend on  $t$ , will converge to a unique stationary distribution  $\phi$ . When an arbitrary starting state  $\vec{\Theta}_0$  was chosen, the chain will take a number of steps before it converges to the stationary distribution. A Markov chain with a selectable desired stationary distribution, can be constructed e.g. using the Metropolis-Hastings algorithm. The transition kernel of the Metropolis-Hastings algorithm consists of a *proposal distribution* from which a sample is drawn and accepted with a certain probability depending on the desired  $\phi$  of the chain. The dependence of the algorithm on the previous state arises because  $\phi$  is evaluated at  $\vec{\Theta}_t$  and  $\vec{\Theta}_{t+1}$ .

In the present case the desired stationary distribution is the posterior pdf (equation 3.2), whose numerical implementation is based on the likelihood and the priors described above. A Cauchy distribution for each element of the parameter vector  $\vec{\Theta}$  is used as proposal distribution (single-component Metropolis-Hastings algorithm). In a so called *burn-in* phase the width of the proposal distributions is adjusted in a way, that a fraction of roughly 0.35 of the drawn proposal samples are accepted during the Metropolis-Hastings algorithm. As a matter of experience this acceptance rate allows a good convergence of the chain. During the burn-in the chain also departs from the initial state of the chain, thus getting rid of the influence of the initial values of the inversion procedure.

The numerical computations were performed on a linux cluster. On each CPU a chain of the length of  $\mathcal{O}(10^4)$  samples was computed. A burn-in of several thousands of samples was used in each chain to adjust the width of the proposal distributions. The samples of the burn-in were not used for the characterization of the posterior.

The set of samples  $\{\vec{\Theta}_1, \vec{\Theta}_2, \dots, \vec{\Theta}_n\}$  obtained this way was used for the estimation of the parameters of interest. The possibility to formulate estimators for quantities derived from the actual model parameters was employed to depict the reconstructed EEDF  $f_E(\vec{\Theta})$  at a given energy  $E$ . The expectation value for  $f_E$  was extracted from the MC samples in the following way:

$$\langle f_E(\vec{\Theta}) \rangle = \int f_E(\vec{\Theta}) P(\vec{\Theta}|\vec{D}) d\vec{\Theta} \simeq \frac{1}{n} \sum_i^n f_E(\vec{\Theta}_i). \quad (6.4)$$

Its variance is given by:

$$\text{Var}\left(f_E(\vec{\Theta})\right) = \left\langle f_E^2(\vec{\Theta}) \right\rangle - \left\langle f_E(\vec{\Theta}) \right\rangle^2 \simeq \frac{1}{n} \sum_i^n f_E^2(\vec{\Theta}_i) - \left( \frac{1}{n} \sum_i^n f_E(\vec{\Theta}_i) \right)^2. \quad (6.5)$$

In the plots of the results section, which are showing the reconstructed EEDF,  $f_E$  is shown as given in equation (5.5) and multiplied by the electron density  $N_e$ . The parameters of interest that are depicted in the plots are accordingly:  $N_e$ ,  $T_e$  and the values of the spline nodes of equation (5.5).

## 7. Results

In the previous chapters a detailed probabilistic model of the emission spectroscopic diagnostic of a neon dc glow discharge was presented. The model describes the spectroscopic measurement on the neon discharge depending on a number of input quantities, such as the electron energy distribution in the plasma, the atomic data and the properties of the spectroscopic setup. Many of these quantities are subject to uncertainty and are incorporated in the model in a probabilistic way (cf. chapter 6). Instead of assigning a definite numerical value to these parameters, probability distribution functions are used to specify ranges of possible values together with a measure of the plausibility of each value. This applies equally to parameters who are approximately known, like the atomic data and to parameters which are to be determined completely from the spectroscopic data, like the parameters of the EEDF. By connecting the probabilistic model with experimental data, additional information is acquired and is quantified in form of a refined set of probability distributions for the model parameters (cf. 3.1.1). The result of the probabilistic analysis has to be of probabilistic nature, as the conclusions drawn from the uncertain information entering the analysis have also to be uncertain.

Accordingly, the results presented in the following chapter have the form of probability distributions for different model parameters, cf. 3.1.8 for a description of methods for the representation of probability distribution functions. Where suitable, estimators for the best fit values of the parameters (or deduced quantities) and their respective uncertainties are stated. The presentation of the results is divided into two major parts:

- First, the validity of the probabilistic model is demonstrated, as the correctness of the inferred information crucially depends on the quality of the model.
- In a second part, the results that could be inferred from the spectroscopic data are presented: the EEDF at different discharge conditions is reconstructed and the employed atomic data is validated, indicating the importance of continuum coupling corrections in the derivation of certain cross-sections and confirming the correctness of a number of previously unmeasured Einstein coefficients.

All probability distributions that are shown below are obtained using Monte-Carlo sampling, unless otherwise stated.

### 7.1. Validation of the Data Analysis Procedure

In general, the validity of the conclusions inferred from a probabilistic analysis depends on the physically correctness of the model. Though there is no rigorous way of proving the correctness, there are a number of indications that can be considered: The model has to deliver a statistically correct, unbiased description of the measured data, which is reflected by a distribution of the residuals that is consistent with the assumed error statistics of the measurement. Note, that with increasing number of uncertain model parameters an unbiased description of the data gets more and more achievable, while not guaranteeing the correct physical interpretation of the model parameters. This has to be assessed independently, and the dependency of the inferred information

on the validity of the physical picture is something the probabilistic approach has in common with a standard (non-probabilistic) data analysis.

On the more technical side, the accurate implementation, the reliability, and also the potential of the inversion procedure in terms of significance of the inferred quantities, can be examined by reconstructing 'synthetic' data: The forward model is used to obtain simulated data for a given set of model parameters. Then the inversion procedure is applied to the obtained data and if the reconstruction works correctly, the model parameters used to generate the data have to be reobtained and the attainable precision of the reconstruction will be reflected in the uncertainty of the probability distributions of the reconstructed parameters.

This part of the chapter is structured in the following way: First, the statistically correct description of the spectral data is demonstrated. Then the successful reconstruction of simulated, 'synthetic' spectral data is shown. The convergence of the Monte-Carlo sampling, which turns out to be an issue, is discussed. Then the physical correctness of the model is considered by investigating the influence of different assumptions on a number of approximations which are employed in the model. It will be shown, that in particular the consistent identification of the effect of radiation transport for transitions to some of the 3s levels, in simulated and in measured spectral data is an indication for the quality of the model.

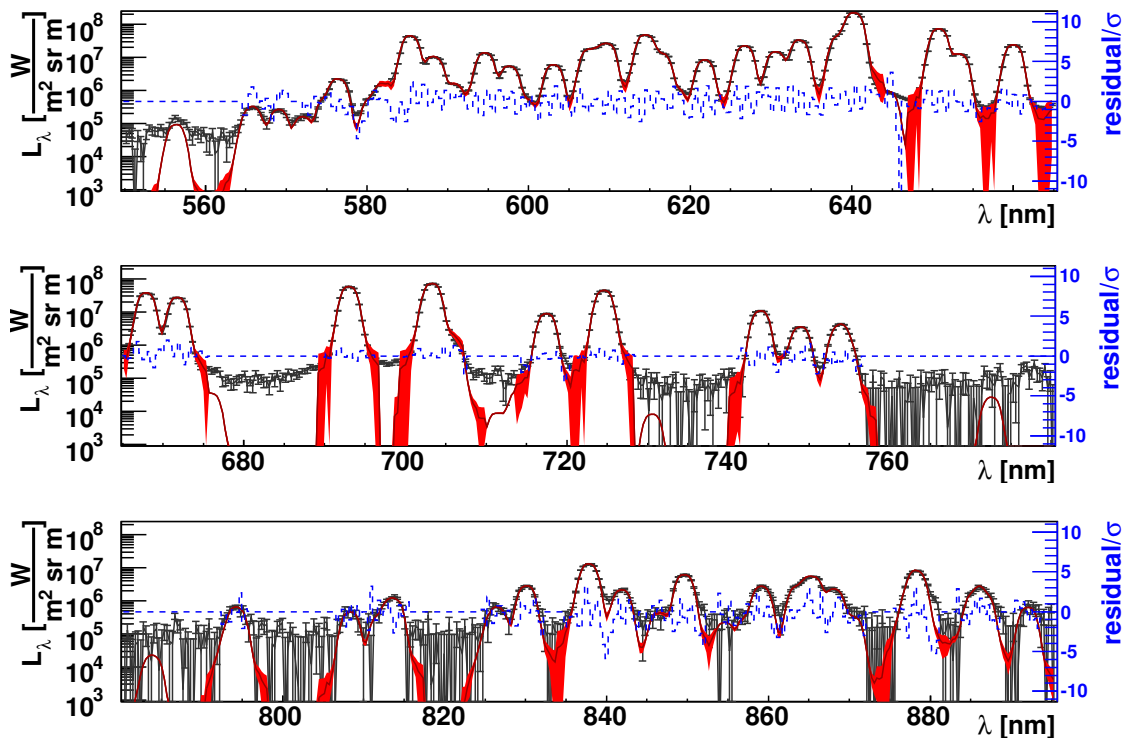


**Figure 7.1.:** Result of the model of the discharge in neon and the spectroscopic measurement. The three rows together show the emission spectrum from 550 nm to 900 nm. The intensity is shown on a logarithmic scale allowing to depict also the less intense lines. The red area is the result of the model and its uncertainty, the black points with error bars show the measured spectrum. The blue dashed curve shows the difference between model and measurement in units of standard deviations  $\sigma$ .

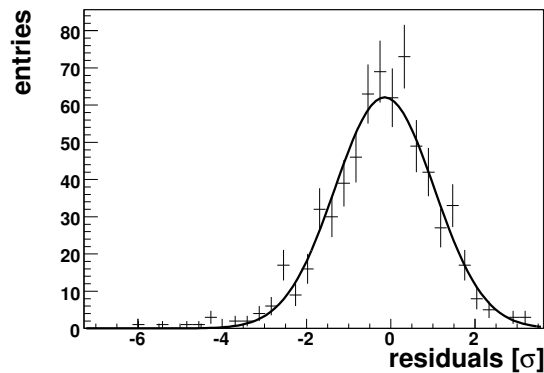


**Figure 7.2.:** Distribution of the residuals between forward model and measurement (cf. Fig. 7.1). The Gaussian which was fitted to the residuals has a mean of  $0.07 \pm 0.07$  and a sigma of  $1.17 \pm 0.05$  (error of mean and sigma as stated by the fitting algorithm).

### 7.1.1. Result of the Forward Model

In Fig. 7.1, the result of the forward model is shown together with a measurement. Every feature of the emission spectrum between 550nm and 900nm is contained in the model: around 60 spectral lines, which can be distinguished by inspecting Fig. 7.1 and contributions from roughly 70 additional weaker lines are taken into account. The high detail of the model is possible due to the extensive set of atomic structure and collision data available from the BSRM calculations<sup>38</sup>.

The red area depicts the uncertainty of the forward model, which is primarily caused by the uncertainty of apparatus function (cf. 5.8), as well as the uncertainty of the intensity calibration (cf. 6.3). The error shown for the measurement is the statistical error (cf. 4.2.1). It is generally small, since the exposure time of the spectrometer can be chosen sufficiently long for the measurement of a steady state of the plasma. The statistical error of the spectroscopic measurement is only important for pixels with very low signal intensity. Otherwise, the uncertainty of the transfer function is the dominant error.

The only significant differences between model and measurement are at 645 nm and around 840 nm, where at some pixels the measured spectral radiance is higher than the simulated one. These small deviations are suspected to be caused by imperfections of the spectrometer-device and are not considered further, because of the little number of concerned pixels. In Fig. 7.2 the distribution of the residuals between model and measurements is shown in units of standard deviations of the respective pixel. The distribution is very close to a normal distribution with variance one and mean zero, which would reflect a perfect description of the data and its uncertainty. Keeping in mind, that the modelled spectroscopic data has a dynamic range of three orders of magnitude, and that the uncertainty of model and data at this point consists only of contributions, that could be physically motivated, this is a strong indication of the consistency and quality of the data model.

In table 7.1 typical population densities of the excited states considered in the forward model are given for the purpose of documentation.

### 7.1.2. Reconstruction of Simulated Spectral Data

The correct technical implementation, the reliability and the potential of the inversion procedure are examined by reconstructing 'synthetic' spectral data: The forward function is used to obtain a simulated spectrum for a given set of model parameters. Then this spectrum is inverted using the present data analysis procedure. If the reconstruction works correctly, the model parameters used

**Table 7.1.:** Population densities of the excited states of neon atoms considered in the forward model. The number are obtained for a typical discharge situation ( $p = 89 \text{ Pa}$ ,  $I = 10 \text{ mA}$ ,  $r_0 = 1.5 \text{ cm}$ )

state	population density [ $m^{-3}$ ]	state	population density [ $m^{-3}$ ]	state	population density [ $m^{-3}$ ]
2p <sub>1</sub>	$2.14871 \cdot 10^{22}$	3p <sub>10</sub>	$8.23057 \cdot 10^{12}$	3d <sub>12</sub>	$9.81717 \cdot 10^{10}$
		3p <sub>9</sub>	$5.15322 \cdot 10^{13}$	3d <sub>11</sub>	$4.3609 \cdot 10^{11}$
		3p <sub>8</sub>	$5.28536 \cdot 10^{12}$	3d <sub>10</sub>	$8.16153 \cdot 10^{11}$
3s <sub>4</sub>	$2.75806 \cdot 10^{17}$	3p <sub>7</sub>	$2.54865 \cdot 10^{12}$	3d <sub>9</sub>	$3.66689 \cdot 10^{11}$
3s <sub>3</sub>	$3.07219 \cdot 10^{16}$	3p <sub>6</sub>	$7.03938 \cdot 10^{12}$	3d <sub>8</sub>	$3.99229 \cdot 10^{11}$
3s <sub>2</sub>	$4.44034 \cdot 10^{16}$	3p <sub>5</sub>	$2.59925 \cdot 10^{12}$	3d <sub>7</sub>	$8.34077 \cdot 10^{11}$
3s <sub>1</sub>	$6.7653 \cdot 10^{15}$	3p <sub>4</sub>	$3.21508 \cdot 10^{12}$	3d <sub>6</sub>	$2.85986 \cdot 10^{11}$
		3p <sub>3</sub>	$7.48251 \cdot 10^{11}$	3d <sub>5</sub>	$5.78695 \cdot 10^{11}$
		3p <sub>2</sub>	$2.16638 \cdot 10^{12}$	3d <sub>4</sub>	$2.69743 \cdot 10^{11}$
		3p <sub>1</sub>	$2.02695 \cdot 10^{12}$	3d <sub>3</sub>	$2.13643 \cdot 10^{11}$
				3d <sub>2</sub>	$2.47991 \cdot 10^{11}$
				3d <sub>1</sub>	$3.63426 \cdot 10^{11}$
		4s <sub>4</sub>	$2.90417 \cdot 10^{12}$		
		4s <sub>3</sub>	$1.75412 \cdot 10^{12}$		
		4s <sub>2</sub>	$4.48691 \cdot 10^{11}$		
		4s <sub>1</sub>	$1.65642 \cdot 10^{12}$		

to generate the data have to be reobtained and the attainable precision of the reconstruction will be reflected in the uncertainty of the probability distributions of the reconstructed parameters.

In Fig. 7.3, the result of a reconstruction of 'synthetic' data is shown. The potential of the reconstruction procedure is demonstrated: Non-thermal features of the EEDF are significantly reobtained by the inversion. This demonstrates the general feasibility of the method to detect non-thermal features of the EEDF.

The color coded histograms show the inferred probability distribution of the EEDF at the respective energy. They are obtained from the Monte-Carlo sampling by creating histograms of the EEDF of each Monte-Carlo sample as described in 3.1.8, equations (3.15) to (3.17). These distributions depict the values of the EEDFs, that are compatible with the spectral data being reconstructed and allow for the assignment of an error band to the reconstructed EEDF.

The 'synthetic' data whose reconstruction is shown in Fig. 7.3 were generated and reconstructed using the parameterization of the EEDF given by equation (5.5), where a spline of 0th order was used (linear interpolation). The positions of the knots of the spline on the energy axis are indicated in Fig. 7.3 by the dashed vertical lines. The value of the spline knots, used for the generation of the 'synthetic' data, were assigned to reproduce the form of the EEDF from kinetic modelling<sup>13</sup>. The form of the EEDF shows a distinct non-thermal behavior, as evident by comparison with the Maxwellian distribution in Fig. 7.3.

It can be observed, that for energies below 5 eV only an upper limit for the electron population can be extracted from the data. The distribution of the allowed values is flat. The reason for this inconclusiveness of the spectroscopic data are the vanishing electron (de-)excitation cross-



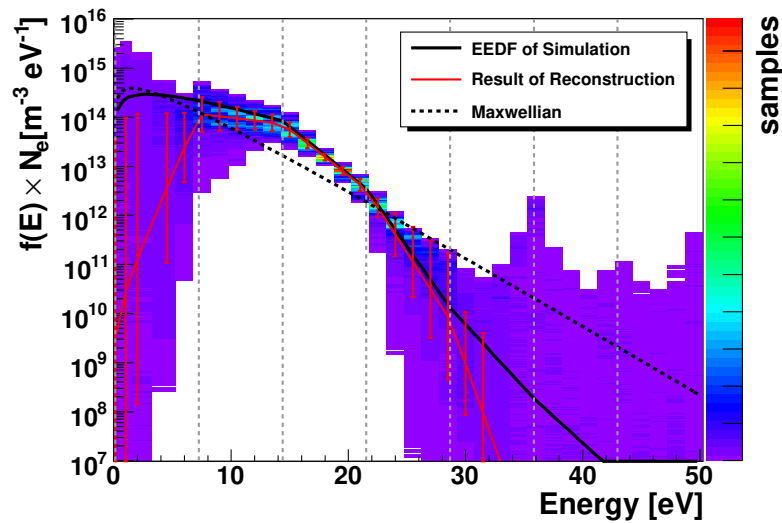


**Figure 7.3.:** Reconstruction of the EEDF from simulated data. The EEDF used to simulate the data is shown together with the result of the reconstruction. The ordinate depicts the number of electrons per energy interval per volume on a logarithmic scale. The black solid curves show the EEDF used to create a simulated spectrum, while the red curve with error bars shows the expectation value and variance of the result of the reconstruction (see also text). The black dotted curve shows a Maxwellian distribution for comparison. The dotted vertical lines indicate the positions of the knots of the spline of the EEDF. The color coded histogram in the background shows the marginal probability distribution as obtained by the Monte-Carlo sampling (see also text).

sections. As will be discussed in 7.1.5 electrons with an energy below roughly 5 eV have negligible impact on the rate coefficients and no influence on the plasma model, accordingly.

A similar behavior can be observed at energies greater than 25 eV. At this energy, the electron population decreases below roughly 1/500th of the population at the maximum of the EEDF, corresponding to a number of  $10^{11}$  electrons per  $\text{m}^3\text{eV}$ . This value appears to be the lower limit for the electron population to result in a significant contribution to the emission spectrum and is independent from energy, for energies higher than the threshold for excitation of 3p states from the ground state.

The red error band in Fig. 7.3 is obtained by computing the mean and variance of the color coded histograms, where the bins of the ordinate are weighted by the logarithm of the EEDF instead of the EEDF itself. The logarithm was used, since the marginal distributions tend to show a flat shape in the logarithm of the EEDF, which can be reasonably described by mean and variance in contrast to the strongly asymmetric shape on a linear scale. In any case, the summary of the marginal distributions by mean and variance only works well in the energy region, where the EEDF is well constrained by the spectral data, otherwise, the full information is only contained in the complete distributions.

### Validation of Atomic Data

The objective of the present analysis is not only the reconstruction of the EEDF, whose correct inversion from simulated data is shown above, but also the validation of the atomic data used to model the spectrum. Therefore, the correct inversion and the information content of the spectral data is also studied with respect to the remaining model parameters.

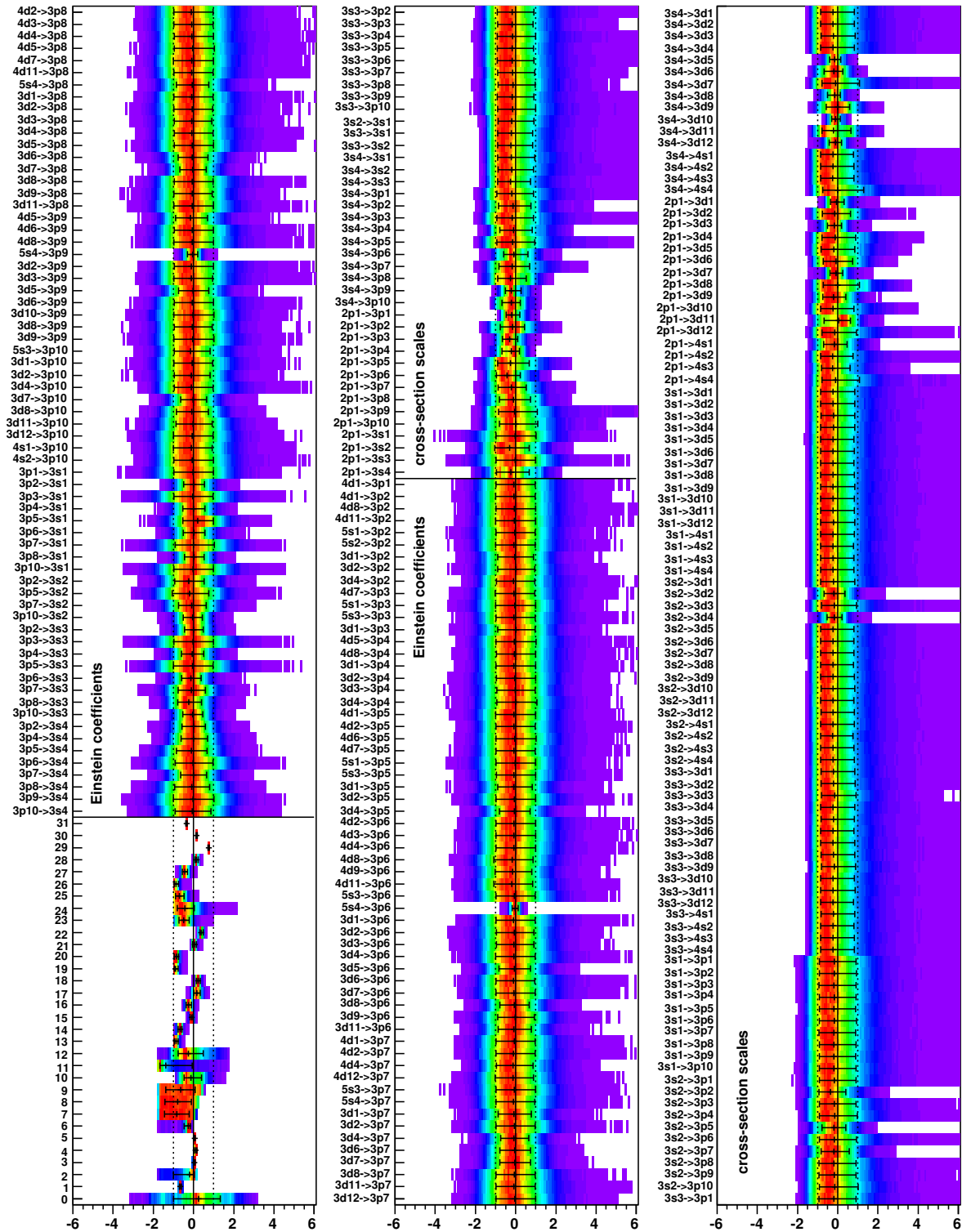


**Figure 7.4.:** Marginal distribution of all model parameters in units of the prior knowledge. Each row shows one marginal distribution, see table 7.2 for the names of the indexed parameters. The marginal distributions are shifted by the expectation of value of their respective prior distribution and the abscissa axis of each marginal distribution was rescaled by the variance of the prior distribution (see also text). The confidence intervals, which are shown, are obtained from the 0.16, median and the 0.84 quantile of the rescaled distribution. A distribution which is centered around zero and has a confidence interval from -1 to 1 corresponds to a parameter for which no information could be inferred from the data.

**Table 7.2.:** Meaning of the indices in Fig. 7.4.

Label	Parameter
0	Scale factor: Uncertainty of absolute intensity scale.
1	Electron temperature of the Gaussian in equation (5.5)
2-9	Value of the spline in equation (5.5) at different energies.
10-12	Effective densities of the $3s_4$ , $3s_3$ and $3s_2$ states for the calculation of optical depth, cf. 5.6
13-24	Densities of the $4d_1 \dots 4d_{12}$ states, which are not described by the collisional-radiative model
25-28	Densities of the $5s_1 \dots 5s_4$ states, which are not described by the collisional-radiative model
29-31	Parameters of the 2nd-order polynomial describing the wavelength calibration

In contrast to the model parameters associated with the EEDF, for which a state of ignorance is assumed apart from the information extracted from the measured data, the atomic data has to be known to a certain precision for the analysis. This state of knowledge, which is based on the structure calculation of the BSRM approach<sup>38</sup> (cf. 6.3) is combined with the information obtained from the spectral data. This means, that based on the probability distributions representing the information of the BSRM calculations which are called *priors* in the following, the incorporation of the information extracted from the measured data with the help of the probabilistic model allows to assign a refined set of distributions, which are called *posterior* distributions. Figure 7.4 shows a comparison of the marginal probability distributions of all parameters *with* and *without* taking into account the information obtainable from the (simulated) spectral data. The difference between the both is exactly the information contained in the likelihood of the spectral measurement, which is to be assessed here.

In order to visualize this difference, each posterior is shifted by the 'true' value of the parameter and is rescaled by the inverse uncertainty of the prior knowledge. Since the data we are considering here were simulated, the 'true' value of each underlying parameter is known. The shift of the distribution allows to verify an unbiased reconstruction of the model parameters, which is reflected by the shifted posterior being centered around zero. Similarly, the rescaling by the inverse width of the prior uncertainty allows to evaluate the amount of information that can be gathered from the analysis of the spectral data for each parameter: A confidence interval from -1 to 1 of the rescaled posterior shows that nothing about this parameter can be learned from the data, while a smaller width reflects the potential of the reconstruction concerning this parameter. The confidence interval, depicted by the black error bar in each row of Fig. 7.4 is obtained by computing the 0.16 and 0.84 quantile of the respective distribution.

**Discussion** The parameters shown in Fig. 7.4 are divided in three groups: First, the parameters labeled by indices, see table 7.2, which are the parameters of interest describing the EEDF and uncertain quantities needed for the description of the spectroscopic measurement. The other two groups consist of parameters accounting for the uncertainty of the atomic data: the Einstein coefficients (second group) and scale factors quantifying the uncertainty of the excitation cross sections (third group). The parameters accounting for the uncertainty of the atomic data are labeled by

the respective initial and final state of the transitions, see also Appendix E for the notation of the excited states of neon.

In the first group of parameters, several marginal posterior distributions can be found, that are very narrow compared to their prior distributions. These are the parameters of the EEDF (index 1..9) for which broad prior distributions are used, in order to incorporate no additional information and the parameters of the wavelength calibration (index 29..31), which are very well determined by the data. The rescaled posteriors of parameters for which flat priors are used are not expected to be located around zero, as the 'true' value of these parameters is not the expectation value of the prior.

For the scale factor accounting for the uncertainty intensity calibration (index 0), no information can be reobtained from the simulated data, as can be seen by the width of the posterior distribution which is close to unity. The large estimated autocorrelation length of  $\kappa \approx 1332$  samples, however, indicates a strong interaction with other model parameters, which is a sign for the importance this parameter for the inference about these parameters.

The parameters with index 10..12 are the effective densities used for description of the opacity of the plasma for photons from transitions to the 3s states. The priors of these parameters are uniform distributions from 0 to 1 and the rescaled posterior is not expected to be centered at zero, accordingly. The opacity of transitions to the metastable states  $3s_4$  and  $3s_2$  can be reconstructed from the data\*, while the effective density of the resonant  $3s_3$  is badly determined. This can be attributed to the smallness of the effect in case of the  $3s_3$  state.

The population of the excited states in the 4d- and the 5s-multiplets are described by parameters 13..28. The priors used for these parameters are exponential distributions with an expectation value of  $5 \cdot 10^9$  (4d) and  $1 \cdot 10^{10}$  (5s). See table 7.1 for the population of the excited states described by the collisional-radiative model. The populations of the 4d- and 5s-states are not well determined by the data. The apparent relative narrowness of the posterior distributions is due to the uncertain prior distributions, again, since the standard deviation of the exponential distribution is equal to its expectation value.

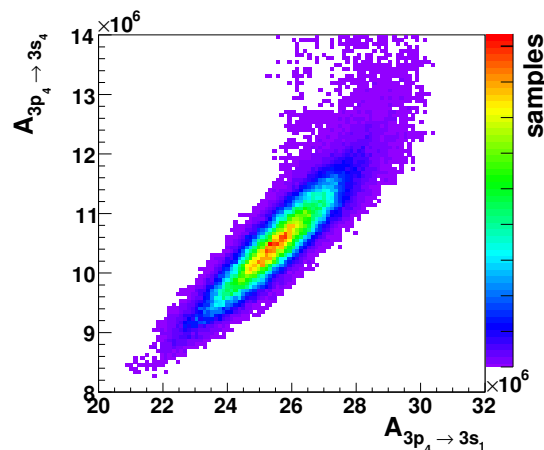


**Figure 7.5.:** Joint marginal posterior distribution of two Einstein coefficients with the same initial state ( $3p_4$ ) as obtained from the Monte-Carlo sampling.

\*The simulated data were generated using a value of 0.43 for the effective densities, which is the ratio between average and peak density of a Bessel function of the first kind.

The reconstruction of the Einstein coefficients from the 'synthetic' data allows to assess the potential of the analysis of the spectroscopic data concerning their validation. By identifying marginal posterior distributions which are not equal to their respective prior distributions, the Einstein coefficients can be recognized, which can be validated by the analysis. It is found that about most coefficients belonging to transitions with an initial state in the 3p-multiplet and also about a part of the transitions with an initial state in the 3d-multiplet information can be gained from the analysis. The width of the posterior distributions is in the region of half the width of the respective prior distribution or greater. This means, that the additional information gained from the analysis of the spectroscopic data only allows a moderate improvement of the precision of each individual Einstein coefficient. On the other hand, even a slight narrowing of the posterior shows, that the information gained from the data (as encoded in the likelihood), has a comparable or larger precision than the employed prior information. In this case, the analysis of measured spectra may serve as validation of previously unmeasured Einstein coefficients<sup>†</sup>. In contrast to the excitation cross-sections whose absolute value can be validated, for the Einstein coefficients only the consistency of the data set can be verified. The reason for this is, that the Einstein coefficients do not determine the total number of photons which are emitted from the plasma. Every excited atom has to decay back to the ground state and emits a photon independently of the precise life time of the excited state. The values of the individual Einstein coefficients only determine the branching ratios among different possible transitions. This is reflected in a strong correlation of the posterior for the Einstein coefficients belonging to transitions with the same initial state. In Fig. 7.5, an example for the joint marginal distribution of Einstein coefficient for the  $3p_4 \rightarrow 3s_4$  and the  $3p_4 \rightarrow 3s_1$  transition is shown.

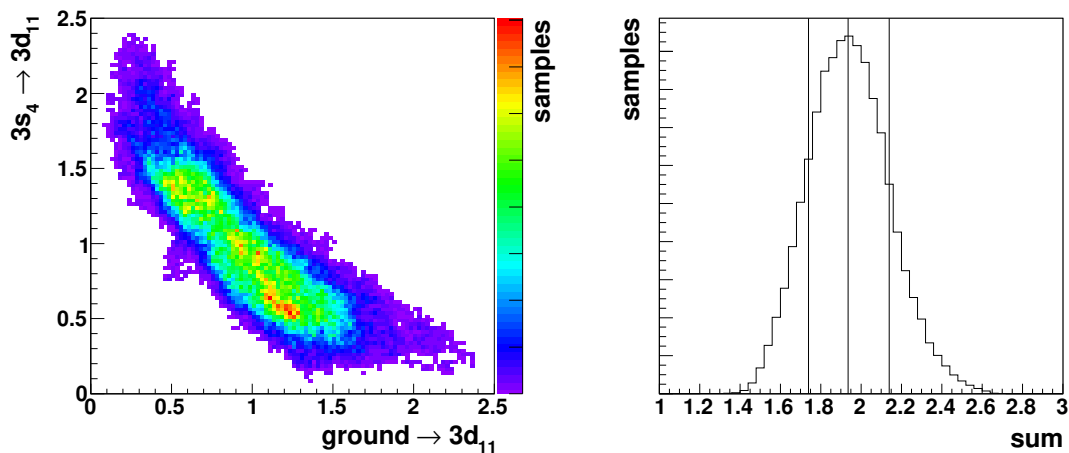


**Figure 7.6.:** Joint marginal posterior distribution of the scale factors for the excitation of the  $3d_{11}$  level from ground and the  $3s_4$  metastable state as obtained from the Monte-Carlo sampling (left). The marginal posterior of the *sum* of both scale factors (right) shows a smaller width, than the individual marginal distributions.

The uncertainties of the excitation cross-sections used for the collisional-radiative model are implemented by means of a scale factor for each cross-section (cf. 6.3). As for the Einstein coefficients, a marginal posterior which is not identical to the used prior proves the significance of

<sup>†</sup>Some of the Einstein coefficients are only available from theory<sup>38</sup>, and are not published in NIST<sup>37</sup> because no experimental validation is available, up to now.

the data concerning the respective scale factor<sup>‡</sup>. In contrast to the Einstein coefficients, the spectroscopic data is sensitive to the absolute value of the excitation cross sections in most cases. For the excitation of some levels, however, the spectroscopic data are not able to resolve the excitation from ground state and the metastable  $3s_4$  state well. In these cases, the joint marginal posterior shows a distinct anti-correlation, as exemplified in Fig. 7.6.

### 7.1.3. Robustness of Reconstruction Against Different Model-Assumptions

It was demonstrated above (cf. 7.1.1), that the forward model allows a consistent description of measured spectra and that the inversion of 'synthetic' data works successfully. In the present section, the physical correctness of the model is assessed by investigating the influence of different assumptions on approximations which are employed in the model.

To achieve this, the 'synthetic' data which were generated using the forward model in its physically most reasonable configuration as described in chapter 5, is reconstructed using different, slightly-changed configurations of the forward model. The result of each reconstruction is summarized by confidence intervals in units of the prior information for each parameter. See also 7.1.2, above, for a description of this graphical representation. In the figures of this section, only the marginal distributions of the Einstein coefficients of transitions from the  $3p$  multiplet are shown. Distributions for the whole set of parameters are given in Appendix D.

In Fig. 7.7, the influence of different model assumptions on the reconstruction of 'synthetic' data is shown. The model configurations obtained by a variation of different assumptions, are as follows (the keywords are referring to the labels in Fig. 7.7):

**standard** The model configuration which was decided to be physically most plausible, is referred to as standard configuration. It was used to generate the 'synthetic' data, as well as for the reconstruction of the measured spectra, if not otherwise stated. In the standard configuration, the radial profiles are taken from Uhrlandt<sup>13</sup>, as described in 5.3 and the optical depth of transitions to the  $3s$ -multiplet is accounted for (cf. 5.6).

**radial profiles** As discussed in section 5.3, the radial profiles available from Uhrlandt<sup>13</sup>, are only available for seven effective, multiplet-*combined* excited states. Multiplet-*resolved* profiles were obtained by using the EEDF at different radial positions, also available from Uhrlandt<sup>13</sup>, as input for the collisional-radiative model of the present analysis. The overall shape of the multiplet-resolved profiles shows some deviations from the effective profiles of Uhrlandt (cf. 5.3). The latter were used for the standard configuration, since they are the result of a detailed radially resolved description of the positive column plasma. In order to study the sensitivity of the reconstruction, a configuration of the forward model using multiplet-resolved profiles is considered.

**22 knots** The flexibility of the parameterization of the EEDF, i.e. the number of knots of the spline in equation (5.5), influences the uncertainty band of the EEDF as function of energy (cf. 7.1.5). A configuration with an EEDF having 22 spline knots is used to examine the influence of a very flexible parameterization on the uncertainty of the reconstruction of the model parameters associated with the atomic data.

<sup>‡</sup>As an outlook, the use of broader, uninformative priors, subsequently for each element of the atomic data set, would allow a closer investigation of the information content of the data for parameters, which can not be validated with the current approach.

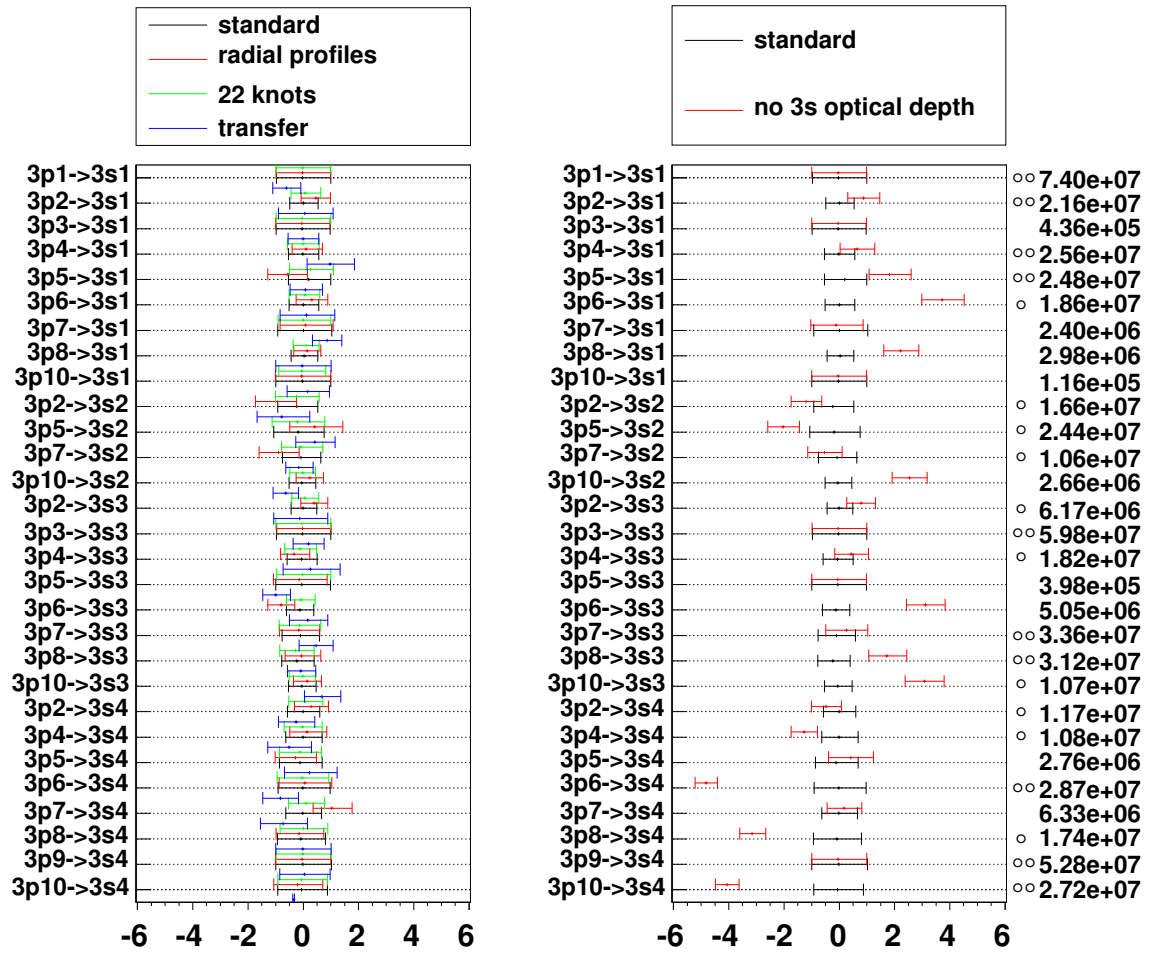


**Figure 7.7.:** Influence of different model assumptions on the reconstruction of 'synthetic' data. In each row of the plot, the marginal posterior distributions of one Einstein coefficient (abscissa) are summarized. The rows are labelled by the final and initial state of the corresponding transition, cf. Appendix E. On left, the influence of different radial profiles of the densities of excited states (red), the influence of a parameterization of the EEDF with a large number of spline knots (green) and the influence of a different apparatus function (blue) are compared to the standard configuration (black). On the right, the effect of the negligence of the optical depth for photons emitted in transitions with a final state in the 3s-multiplet (red) is compared to the standard configuration used to generate the data (black). See Appendix D, for the marginal distributions of the whole parameter set. The numbers at the right side, are the absolute values of the Einstein coefficients. The dominantly depopulating transition of each initial state is marked with two circles (oo), while Einstein coefficients which are larger than one fifth of the dominantly depopulating are marked by one circle (o).

**transfer** The apparatus function  $s_a$  determines the line shape of measured spectral lines, because the experimental resolution is much coarser than the natural line width. The apparatus function is obtained from measured spectra (cf. 5.8) and subject to uncertainty. The precise shape of  $s_a$  is of particular importance in regions of the spectrum with overlapping lines. For the 'transfer'-configuration, a apparatus function is used that was extracted from a different spectrum, than the one used for the generation of the 'synthetic' data. The difference

between the two representations of the apparatus function, however, is merely given by the reproducibility of the apparatus function when extracted from different measured spectra.

**no 3s optical depth** The last configuration being considered, is obtained by neglecting the optical depth of transitions with a final state in the 3s multiplet. The escape factors of these transitions, as derived in in 5.6, are not incorporated in the model and the influence on the reconstruction is examined.

In the left part of Fig. 7.7, the influence of the different radial profiles, the parameterization of the EEDF with high flexibility, and the variation of the apparatus function are shown in comparison with the standard configuration. The effect of the optical depth of the transitions with final states in the 3p-multiplet are shown separately in the right part of the figure.

The influence of the three first mentioned model variations is not significant. The obtained confidence intervals are with a few exceptions compatible with the 'true' values of the parameters used to generate the 'synthetic' data. This is an indication for the robustness of the reconstruction against the underlying assumptions. This is still true, when considering the whole set of marginal distributions shown in Appendix D. In particular, the flexibility of the parameterization of the EEDF (cf. 7.1.5), which is determined by the number of spline knots in equation (5.5), does not influence the reconstruction of the model parameters used for the description of the Einstein coefficients and excitation cross-sections. The greatest sensitivity can be observed with respect to the precise modelling of the apparatus function. In particular, the atomic data needed for the description of spectral lines with an initial state in the 3d-multiplet show a high sensitivity to the correctness of  $s_a$ . This can be seen, for example, by the scale factor for the electron excitation cross-section for the transition  $3s_4 \rightarrow 3d_{12}$ , and by the Einstein coefficient of the transition  $3d_2 \rightarrow 3p_{10}$ . This sensitivity is caused by the overlap of the different spectral lines of transitions with an initial state in the 3d multiplet in the measured spectra. Several of the 3d-multiplet lines cannot be well resolved and the fraction of the measured intensity that is assigned to each line is sensitive to the precise form of the apparatus function. This observation emphasizes the importance of the correct determination of  $s_a$  from the spectral data and need of monitoring the quality of the obtained description.

In the right part of Fig. 7.7, the effect of the optical depth of the transitions with final states in the 3p-multiplet is shown. The influence on the reconstruction is significant, for this configuration. The reconstructed parameters differ by several standard deviations from the 'true' values of the simulated data. The negligence of the additional escape factors has the same effect onto the reconstruction like an overestimation of Einstein coefficients. When the data would allow an unambiguous determination of the Einstein coefficients, the posterior could always be expected to show a deviation towards negative values in the representation of of Fig. 7.7. This can, however, not be observed in Fig. 7.7: the marginal posterior distributions of several Einstein coefficients show a preference for values larger than their 'true' values. This behavior is caused by the fact, that the Einstein coefficients enter the forward model twice: The line intensity is proportional to the respective Einstein coefficient for a *given* population density of the initial state, but the Einstein coefficient also determines the population density by determining the rate coefficient depopulating the initial state.

When an excited state can only be observed through a single spectral line, because other transitions are too weak too be measured, then the two effects precisely cancel each other. In this case, the line intensity is insensitive even to escape factors as small as 0.2 (transition  $3p_9 \rightarrow 3s_4$ , cf. table 5.3, in 5.6). The  $3p_1$ -,  $3p_3$ -, and  $3p_9$  levels are only measured through a single lines, the second strongest lines of the  $3p_1$ -,  $3p_3$  state have coefficients, which are about a factor of more than 50 smaller than the dominant coefficients. Accordingly, the confidence interval of the marginal posteriors for the transitions from these levels extend precisely from -1 to 1.



When there are more than one spectral line with the same initial state, the situation is different. In this case, there is a positive correlation between the Einstein coefficients associated with the same initial state. Typically, there are one or two large Einstein coefficients which dominantly determine the population density of their initial state in the collisional radiative model. The Einstein coefficients of the weaker transitions only determine the intensity of the respective spectral line, but their influence to the population of the initial state can be neglected. The correlation between all the coefficients occurs, because a higher value of a dominant Einstein coefficients leads to a lower population density, which requires increased coefficients of all other transitions to obtain the line intensities given by the data being reconstructed. The other way round, when the value of a weak coefficient is increased, the spectral line of the weak transition can be fitted by reducing the population density of the initial state via increased Einstein coefficients of the dominantly depopulating transitions.

This correlation is the reason, why the Einstein coefficients of transitions which are not subject to optical depth are overestimated: Due to the changed model, the 'true' value of the some Einstein coefficients are shifted to smaller values. (Accounting for the omitted Escape factors). The reconstruction of the model parameters is biased towards the original unshifted value by the informative priors used for the Einstein coefficients. This leads to an overestimation of the shifted value which, because of the correlation described above, is accompanied with an overestimation of the Einstein coefficient which are not subject to optical density, or only weakly, as e.g. the case for the  $3p_8 \rightarrow 3s_3$  transition.

#### 7.1.4. Convergence of the Monte-Carlo Sampling

As described in 3.1.8, the Metropolis-Hastings algorithm, that was used to characterize the probability distributions is a Markov-chain based algorithm and as such does not produce independent draws from the posterior distribution. Especially when sampling high dimensional distributions, like for the present analysis, a large number of samples may be necessary for a comprehensive characterization. In order to assess the number on required samples, the quality of the convergence has to be monitored for each parameter of the sampled distribution.

Convergence of EEDF Reconstruction Autocorrelation length of all parameters bad parameter

In Fig. 7.8 and Fig. 7.9, the result of a study of the convergence of the reconstruction of the parameters associated with the EEDF is shown. The plots on the left side of Fig. 7.8 and Fig. 7.9 show the result of a Monte-Carlo sampling using twelve chains with a length of 20000 samples, while the plots on the right side show the result of a longer sampling (eight chains with 120000 samples). It can be seen, that especially for the parameterization shown in Fig. 7.8, after a chain length of 20000 samples the uncertainty of the EEDF is still underestimated.

The two parameterization that were used for the product  $f(E) \times N_e$ , differ with respect to the normalization of the EEDF. Both are mathematically equivalent, in the sense that every functional form that can be described by the can first also be described by the second. For the upper plot, an EEDF was used, that is normalized to one (equation 5.6), and that is multiplied with the electron density, just as expected by physical intuition. It can be seen, though, that this parameterization has got an unfavorable influence on the convergence of the sampling: The uncertainty of the EEDF obtained by the Monte-Carlo chains with 20000 samples (left of Fig. 7.8) is still underestimated. Only in the much longer samplings shown on the right a better estimate of the uncertainty is revealed.

For the plots in Fig. 7.9, a parameterization was employed where the electron density is not implemented as sampling parameter, but set to a fixed value. In this case, the flexibility of the correcting spline is utilized to describe the quantity  $F_M(E) \times N_e$  at different electron densities.

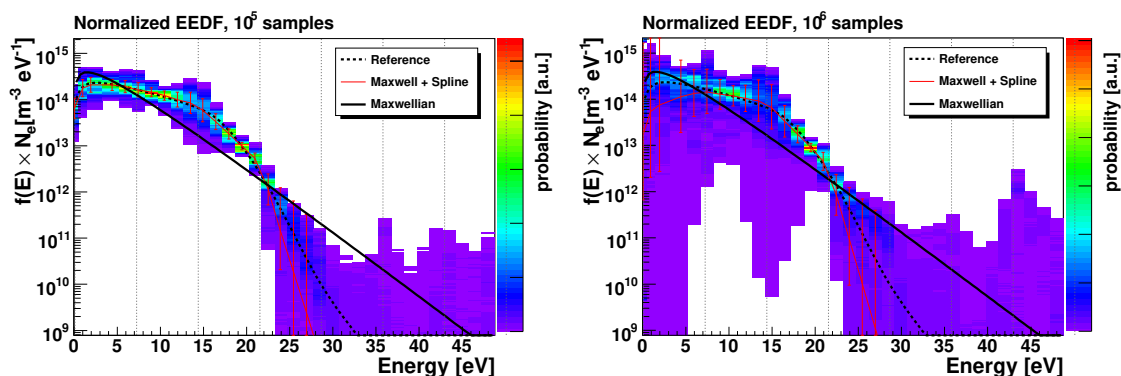


**Figure 7.8.:** Reconstruction of the EEDF using Monte-Carlo chains with a length of 20000 (left) and 120000 (right) samples. The analyzed data were simulated using the forward model (cf. 7.1.2). The result of the reconstruction (color coded histograms, summarized by the red graph with error bars), is shown together with the EEDF used for the simulation (black solid curve), see also caption of Fig. 7.3. Here the electron density was implemented directly as model parameter together with a *normalized* EEDF, see text for more details.

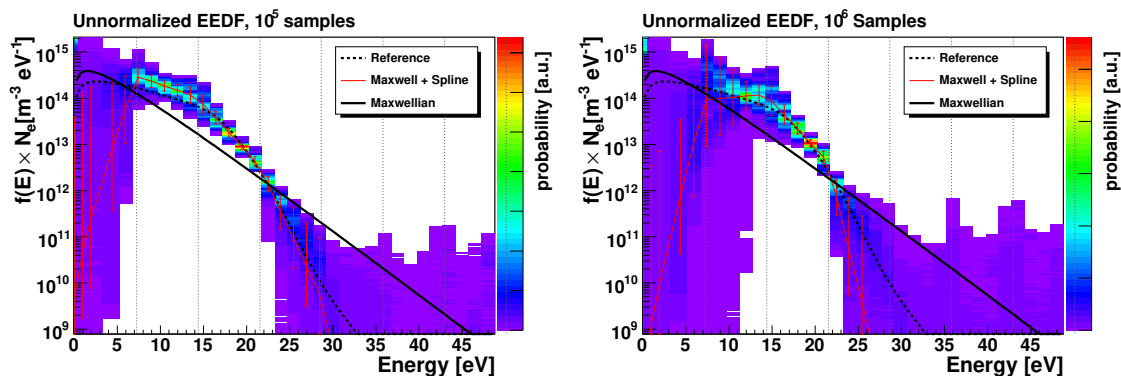


**Figure 7.9.:** Reconstruction of the EEDF using Monte-Carlo chains with a length of 20000 (left) and 120000 (right) samples, see Fig. 7.8 for a description of the depicted elements. Here, an implementation of the quantity  $f(E) \times N_e$ , was used, which can be sampled more efficiently and the EEDF is not normalized to one, see text for more details.

(cf. 5.4, equation 5.5). By using this parameterization a faster convergence of the Monte-Carlo is achieved. This can be seen when comparing the left and right plot of Fig. 7.8: The uncertainties obtained with short (20000) and long (120000) Monte-Carlo chains are more similar than in the normalized case below.

Note, that also after the long samplings, the uncertainty bands of the two parameterizations differ: The reconstruction using the normalized EEDF (Fig. 7.8) shows an increased uncertainty around 15 eV. This is consistent with the results discussed in 7.1.5: Electrons in the region between approximately 12 eV and 18 eV have a weak influence on the population of the excited states of the  $3p$  multiplet, as the cross-sections for excitation from the  $3s$  levels decreases at these energies, and the threshold for excitation from ground state is at 18.38 eV. Therefore the information of the spectral data does not constrain the electron population in this energy region. There uncertainty bands also differ at low energies: the unnormalized parameterization shows a completely flat distribution below approximately 8 eV, while the normalized one, though also quite broad in this region shows a clear preference for values of roughly  $10^{14}..10^{15} \text{ m}^{-3} \text{ eV}^{-1}$ . Also in this region, there is a very

**Table 7.3.:** Parameters with the largest  $\kappa$ .

Parameter		Autocorrelation length
4th knot of correction spline	(21.5 eV)	44978.2
3rd knot of correction spline	(14.1 eV)	35533.9
2nd knot of correction spline	(7.1 eV)	13786.6
5th knot of correction spline	(28.7 eV)	8211.16
electron temperature of Maxwellian		3315.67
scale factor of excitation cross-section	$2p_1 \rightarrow 3p_1$	2364.18
effective density for optical depth of $3s_4$		2253.08
scale factor of excitation cross-section	$3s_4 \rightarrow 3d_{10}$	1790.13
scale factor of excitation cross-section	$2p_1 \rightarrow 3s_4$	1722.27
scale factor of excitation cross-section	$2p_1 \rightarrow 3d_{11}$	1576.33
scale factor of excitation cross-section	$3s_4 \rightarrow 3d_{11}$	1528.56

weak, or no contribution at all to the excited state populations. Therefore no inference about the electron density at these energies can be made from the data. Consequently, the uncertainty in the regions around 15 and below 8 eV band mainly reflects the flexibility of the used parameterization (cf. 7.1.5) instead of the information content of the data.

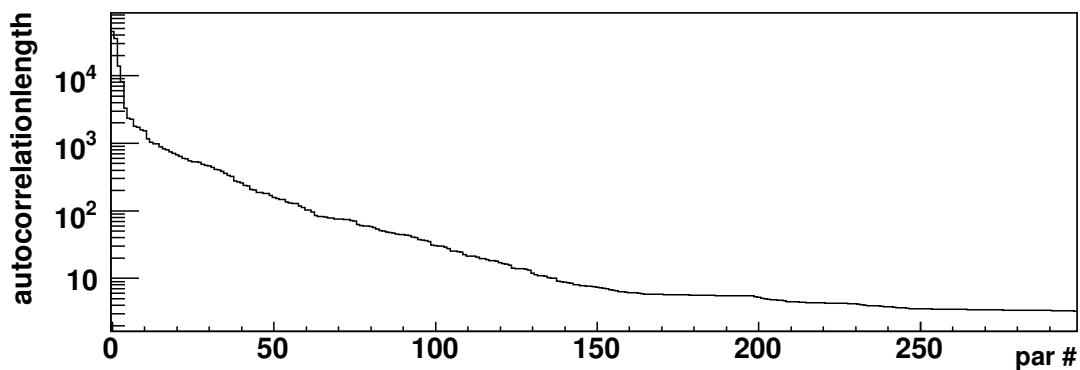


**Figure 7.10.:** The autocorrelation lengths of all parameters of the model. The parameters are sorted by autocorrelation length in descending order, see table 7.3 for the parameters with the largest autocorrelation lengths.

In order to assess the quality of the convergence for all model parameters, the autocorrelation length  $\kappa$  of the parameters is considered. As described in 3.1.8,  $\kappa$  quantifies the degree of statistical dependence of succeeding samples, a small autocorrelation length is an indication for fast convergence. A sample can be regarded as effectively statistically independent from another sample, when the separation of the both is at least  $\kappa$  samples.

In Fig. 7.10, the autocorrelation lengths of all parameters of the model are shown, as obtained with the model-configuration used to create the right part of Fig. 7.9. The parameters are sorted in order of descending autocorrelation length, a list of the parameters with the largest  $\kappa$  is given in table 7.3. The majority of parameters has a  $\kappa$ , which is smaller than  $\mathcal{O}(1000)$  samples. The distribution of these parameters is well converged, when several Monte-Carlo chains with a length of more than 10000 samples are used as in the preceding examples. This can be also seen in Fig. 7.11, where the sequence of samples of the parameter with the *tenth largest* autocorrelation length (1529 samples) is shown. The convergence criterion of Gelman<sup>50</sup>, given in equation 3.26

(section 3.1.8) has got a value of  $\sqrt{\widehat{R}} \approx 1.03$ , which is close enough to unity, to indicate reasonable convergence. All parameters with smaller  $\kappa$ , show an even better convergence.

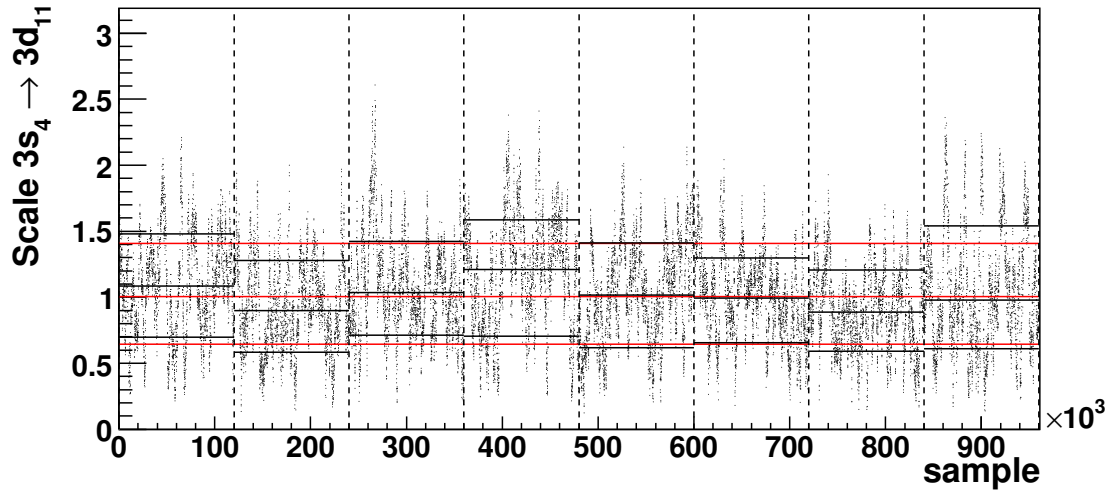


**Figure 7.11.:** Sequence of Monte-Carlo samples for a parameter with  $\kappa \sim 1529$  samples. The parameter that is shown (ordinate), is a scale factor of the cross-section of electron excitation from the  $3s_4$  to the  $3d_{11}$  state. Eight chains, each with  $1.2 \cdot 10^5$  samples were used for the MC run, the samples are numbered from 0 to  $9.6 \cdot 10^5$  throughout the different chains (abscissa), the vertical dashed lines showing the end of the individual chains. The horizontal black lines show the 0.16, 0.5 (median) and 0.84 quantile of distribution of each individual chain, the red horizontal lines, show the 0.16 and 0.84 quantile and the median of the combined result.

There are, however, a few parameters, which have a considerably larger autocorrelation length, rendering a length of the Monte-Carlo chains of several  $10^5$  samples or more desirable. Unfortunately, the upper limit for the sensible length of a single chain is around  $10^5$  samples, requiring about one week of computing time. In Fig. 7.12, the sequence of Monte-Carlo samples of the parameter with the largest autocorrelation length (44978 samples) is shown. The slow variation of the parameter value for subsequent samples reflects the slow convergence and long autocorrelation length of the Markov chains for this parameter. Also, the results of the different chains differ more strongly, than for the parameter shown in Fig. 7.11, as depicted by the horizontal black lines in Fig. 7.12. The initial value, which was used for the eight chains, lies close to the median of the sampled distribution. This is the case, because the result of a shorter, exploratory sampling was used as starting point for the long chains.

The time traces of all chains, except of the two last ones, change the direction of their overall trend at least once, giving an indication of the chains being close to convergence. The convergence criterion of Gelman<sup>50</sup> (cf. 3.1.8) has a value of  $\sqrt{\widehat{R}} \approx 1.57$  for this parameter. In table 7.4 the criterion of Gelman is shown for samplings of different lengths. For comparison, the criterion is also listed for the parameter with the longest autocorrelation length of the reconstruction using the normalized parameterization of the EEDF, as described above. It can be seen, that the  $\sqrt{\widehat{R}}$  gets closer to unity with increasing number of samples.

$\sqrt{\widehat{R}}$  quantifies the ratio between an upper and lower limit for the variance of the respective parameter (equation 3.26). As the increase of the number of samples beyond  $10^5$  per chain would be tedious, the ratio of  $\sqrt{\widehat{R}} \approx 1.57$  is only taken as an indication, that the actual uncertainty of the

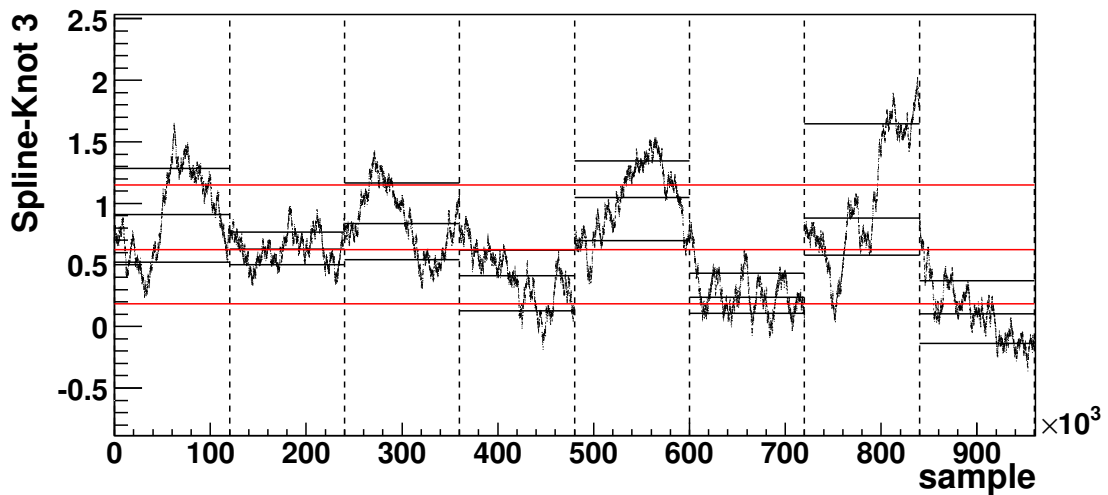


**Figure 7.12.:** Sequence of Monte-Carlo samples for the value of the correcting spline (ordinate) at a position of 21.5 eV,  $\kappa \sim 44978$  samples. See Fig. 7.11 for a description of ordinate and the horizontal lines.

parameters with the highest correlation lengths ( $>10000$  samples, see table 7.3) might be slightly larger than obtained from the Markov chain Monte-Carlo.

### 7.1.5. Influence of the Parameterization of the EEDF

The parameterization of the EEDF affects the result of the reconstruction by constraining the possible shapes of the EEDF. In order to allow the observation of deviations from a thermalized Maxwellian distribution, a so called *form-free* parameterization (equation 5.5), is used for the reconstruction (cf. 5.4). By form-free, the utilization of a spline-based parameterizations is denoted, which allows to describe a wide class of EEDFs with different shapes. The flexibility of the spline-based parameterization depends on the number of knots and the order of the employed spline function. The effect of parameterization with varying flexibility is examined in the present section.

In Fig. 7.13 the Reconstruction of 'synthetic' spectroscopic data is shown for different numbers of spline knots. Generally it can be observed, that the width of the error band of the reconstructed EEDF rises with increasing number of spline knots, reflecting the smaller amount of constraining information introduced by more flexible parameterizations. The reconstruction obtained using only three spline knots shows an almost Maxwellian shape of the distribution function and the uncertainty in the region just above 25 eV is indeed larger, than the uncertainty of the reconstruction obtained using four knots. This is not in contradiction to the smaller flexibility of the parameterization, as a model which is over-simplified and unable to reproduce the physical situation, frequently leads to an increased uncertainty of reconstructed model parameters. (The description of the data then usually is equally bad for a wider range of parameters.) The parameterizations with six and eight spline knots are able to reproduce the shape of the EEDF used to generate the data, well. When the number of spline knots is increased further, fine grained variations of the EEDF can be formed, which the data is not sensitive to. The result is an increased error band in the region below 6 eV and between 12 eV and 16 eV. The spectroscopic data seem to carry no information about the electron population in these regions of energy. In order to examine the physical plausibility of this

**Table 7.4.:** Convergence criterion of Gelman<sup>50</sup> (cf. 3.1.8) for samplings of different length. The samplings also depicted in Fig. 7.8 and Fig. 7.9 (see above) were used to obtain the numbers. In each case, the  $\sqrt{\widehat{R}}$  (equation 3.26) of the parameter with the longest autocorrelation length (2nd knot of correction spline for Fig. 7.8,  $\kappa \sim 88880$  samples, and 4th knot of correction spline for Fig. 7.9:  $\kappa \sim 44978$  samples) is given. For the shorter samplings subsets of the whole sequences were used.

---

Samples	$\sqrt{\widehat{R}}$	$\sqrt{\widehat{R}}$
	EEDF normalized $\kappa \sim 88880$ samples (Figure 7.8)	EEDF not normalized $\kappa \sim 44978$ samples (Figure 7.9)
8*6000	9.1	7.9
8*12000	7.6	4.58
8*30000	5.1	3.82
8*60000	4.6	2.81
8*90000	3.2	1.94
8*120000	2.1	1.57

---

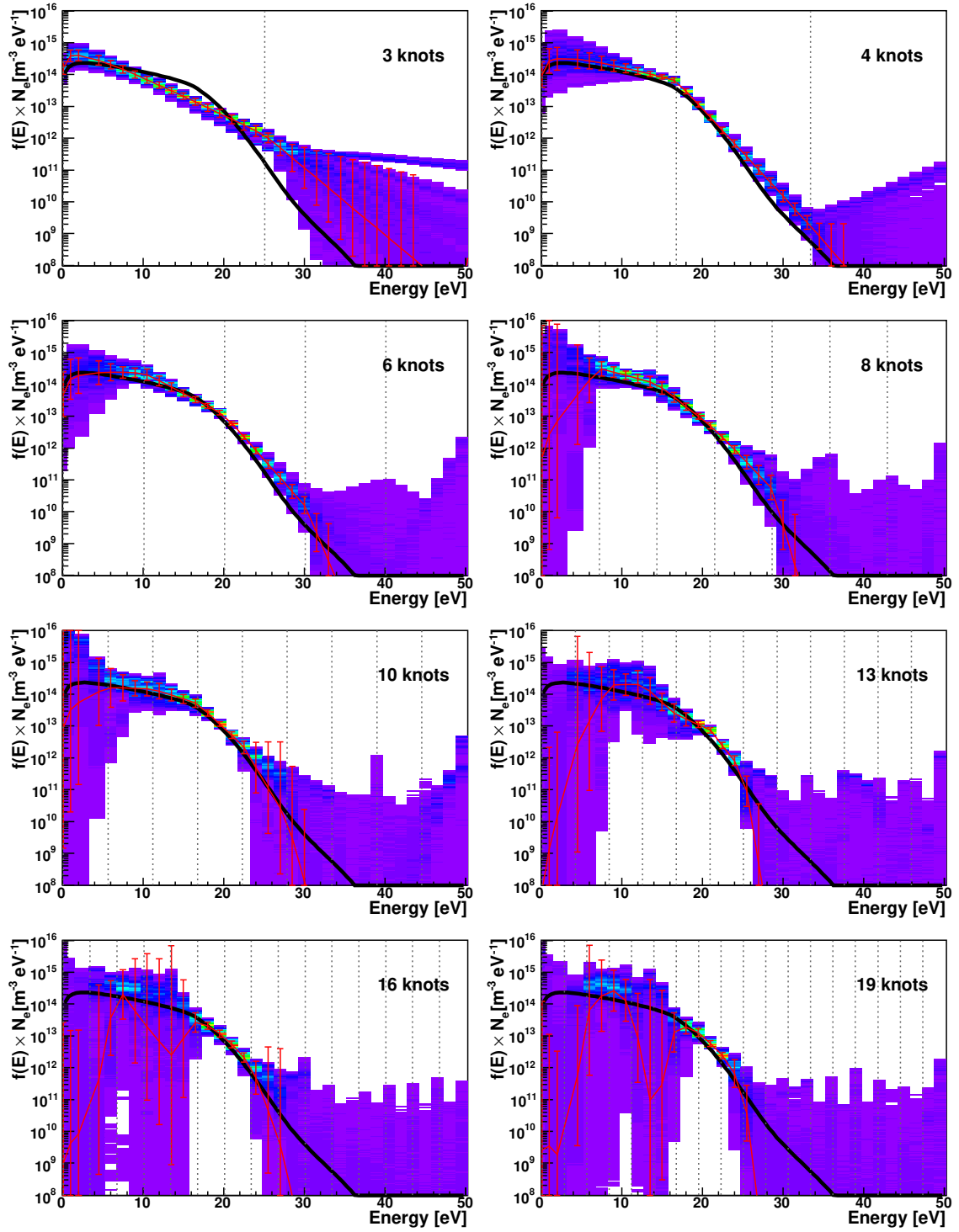


**Figure 7.13.:** Reconstruction of the EEDF from simulated data using different numbers of spline knots. The ordinates depict the number of electrons per energy interval per volume on a logarithmic scale. The black solid curve shows the EEDF used to generate the 'synthetic' data, while the red curve with error bars shows then expectation value and variance of the result of the reconstruction (cf. 7.1.2). The dotted vertical lines indicate the positions of the knots of the spline of the EEDF. The color coded histogram in the background shows the marginal probability distribution as obtained by the Monte-Carlo sampling. See also 7.1.2 for more details of this representation of the result of the reconstruction.

assertion, The variation of the population densities caused by a change of the EEDF at a given energy is considered.

### Energy Dependence of the Elementary Processes.

The effect of a change of the EEDF at different energies is assessed by considering a piecewise constant parameterization of the EEDF was used:

$$f_{\text{pw}}(E) = \begin{cases} f_1 & \text{for } E < E_1 \\ f_2 & \text{for } E_1 < E < E_2 \\ \vdots & \\ f_n & \text{for } E_{n-1} < E < E_n \end{cases}, \quad (7.1)$$

where each  $f_i$  is a constant. In order to obtain the relative change of the population density  $\Delta n_i/n_i(E)$ , a set of  $f_i$  was used, which replicates the EEDF from kinetic modelling<sup>13</sup>. Each  $f_i$  was sequentially increased by 10% and the resulting variations of the population densities were plotted versus the energy  $E_i$ , see Fig. ??

The thresholds for the different excitation and de-excitation channels can be observed clearly (direct excitation, stepwise excitation, and cascade contributions).

The reconstruction of the EEDF is expected to be well determined by the data in energy regions where two conditions are fulfilled: First, the variation of the population densities must not be small and second, there have to be differences in the shape of  $\Delta n_i/n_i(E)$  for some of the excited states. When the values of  $\Delta n_i/n_i(E)$  for all states are proportional to each other, a variation of the EEDF influences all line intensities in a similar way. In that case, the EEDF cannot be unambiguously reconstructed.

The uncertainty of the reconstructed EEDF reflects how well these conditions are fulfilled for different energy regions. The uncertainty of the reconstructed EEDF exhibits a minimum around 17 eV, where the spread in the variations is large. Above 30 eV, where the error band starts to increase considerably, the variation of the population densities also becomes small. In the region between 10 and 17 eV, the EEDF is constrained by the chosen parameterization with six spline knots. Samplings with more flexible parameterizations of the EEDF also show an increased error band in this region.



## 7.2. Results Obtained from the Emission Spectra of the Neon Discharge

In this chapter, the results obtained by the analysis of data from optical emission spectroscopy on a neon discharge are presented. The EEDF in the positive column is compared to the EEDF from independent kinetic modelling, and a good agreement is found. The results of the analysis of spectroscopic data collected for different discharge conditions are presented and compared to data from probe measurements<sup>11</sup> and kinetic modelling<sup>13</sup> where available.

The integrated data analysis approach allows to draw conclusions about the validity of the used set of atomic data. The results of this validation are given. The consistence of previously unmeasured Einstein coefficients could be verified. Correction factors for the rate coefficients for electron excitation of a part of the considered levels are extracted from the spectral data. The corrections verify the relevance of continuum coupling in the quantum mechanical models used to obtain the electron excitation cross-sections.

### 7.2.1. Reconstruction of the EEDF

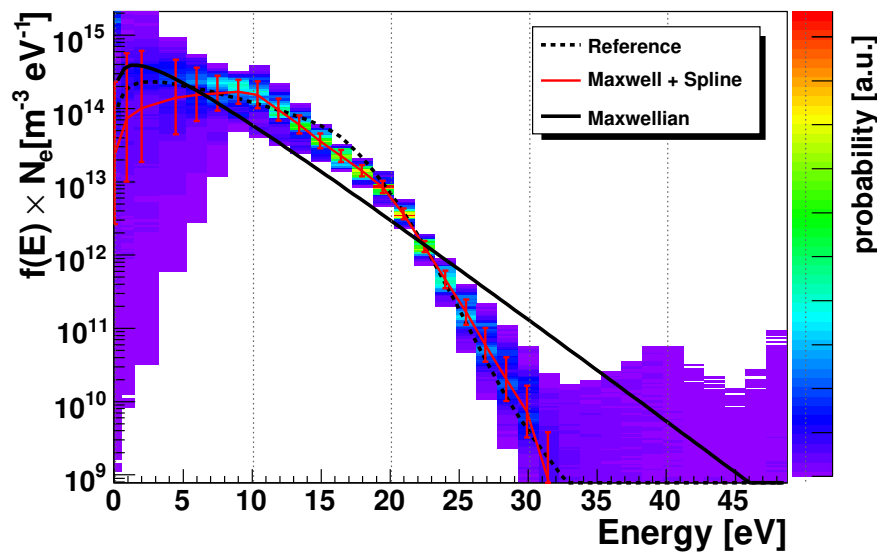


**Figure 7.15.:** Reconstruction of the EEDF in the positive column of the neon dc-discharge. The ordinate depicts the number of electrons per energy interval per volume on a logarithmic scale. The black dotted curve, showing the EEDF as obtained in independent kinetic modelling<sup>13</sup>, acts as a reference. The black solid curve shows a Maxwellian distribution. The red curve with error bars shows the expectation value and variance of the result of the reconstruction (cf. 7.1.2). The dotted vertical lines indicate the positions of the knots of the spline of the EEDF. The color coded histogram in the background shows the marginal probability distribution as obtained by the Monte-Carlo sampling (see also text).

In Fig. 7.15 the result of the reconstruction is shown for spectroscopic data obtained from the positive column of a neon discharge. The discharge (radius 1.5 cm, gas pressure 89 Pa) was operated without striation at a discharge current of  $I = 5$  mA. The uncertainty band of the reconstruction

(cf. 7.1.2 and 7.1.5) results from experimental errors: uncertainty of calibration procedure, apparatus function (cf. chapter 6) and from the uncertainty of the atomic data set.

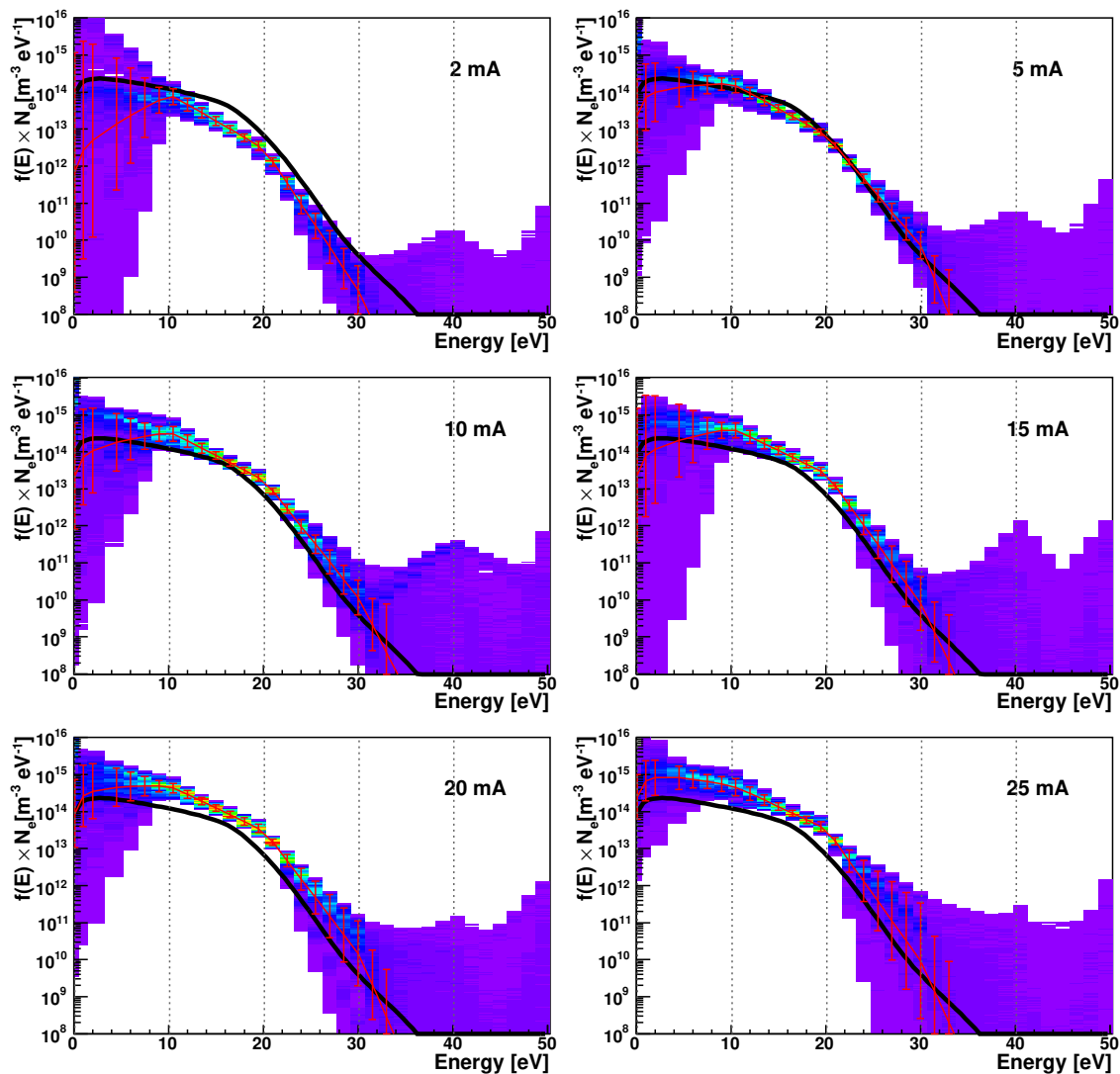


**Figure 7.16.:** Reconstruction of the EEDF in the positive column of the neon dc-discharge for different discharge currents. See caption of Fig. 7.15 for the description of the graphical representation. The respective discharge-current is given in the upper-right corner of each reconstruction. The black solid curve shows the result of independent kinetic modelling for a discharge current of 5mA. The result for the electron density is shown in Fig. 7.17.

For the reconstruction, the EEDF was described using the parameterization given in equation (5.5), which uses a spline to achieve a flexible description of non-thermal features of the distribution function. The positions of the spline knots were fixed, as indicated by the vertical dashed lines in Fig. 7.15. The Maxwellian distribution is shown to illustrate the non-thermal features of the reconstructed distribution.

The result of the reconstruction is compared to the EEDF obtained by independent kinetic models<sup>13</sup>. The model, which our results are compared to, describing a neon discharge with radius 1.5cm and a neon pressure of 90Pa, was validated in specific experiments<sup>13</sup>: The axial field strength and the radial variation of the space charge potential were verified using probe measure-

ments<sup>7</sup> and the absolute densities of the excited atoms were measured as a function of radius by measuring the longitudinally integrated optical depth with absorption spectroscopy<sup>10,12</sup>.

In Fig. 7.16, the result of the reconstruction is shown for different discharge currents. The EEDF from kinetic modelling, which is shown for comparison, was obtained for a discharge current of 5mA. It can be seen, that only the electron density (normalization of displayed function) varies for the different currents, while the reconstructed shape is very similar for all six currents.

It is known from modelling and probe measurements, see e.g. Ref. (66), that in the stable low-pressure glow discharge, the discharge current has a weak influence on the longitudinal electric field. The shape of the EEDF, which is the result of an equilibrium between the energy gain in the electric field and energy-loss processes, shows the same independence. In contrast, the electron density is expected to change proportional to the discharge current, because electrons are the strongly predominating charge carriers.

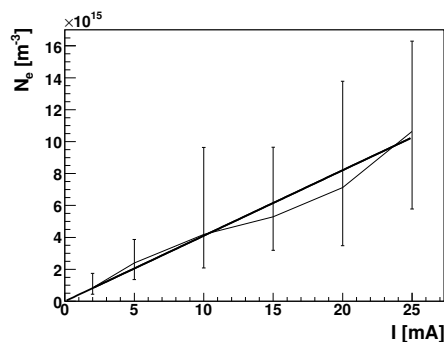


**Figure 7.17.:** Electron densities obtained from the reconstruction at different discharge currents (cf. Fig. 7.16). The asymmetric errors are obtained from the 0.16 and 0.84 quantile of the marginal distribution.

In Fig. 7.17 the electron density is shown as obtained by the Monte-Carlo sampling. Shown is the median of the marginal posterior of the integral  $\int f(E) \times N_e dE$  (cf. equation 5.5). The error bars, obtained from the 0.16 and 0.84 quantile of the marginal distribution include all uncertainties of the reconstruction (experimental, atomic data). The proportionality to the discharge current, also known from probe measurements<sup>11</sup>, is apparent by comparison with the straight line fitted to the data points (intercept 0, slope  $4.1 \cdot 10^{14}$  electrons [ $m^{-3}mA^{-1}$ ]).

The comparison of the EEDF in the positive column of the discharge with independent results from kinetic modelling shows good agreement. The electron density and the shape of the EEDF for energies below  $\sim 30$ eV can be obtained from the spectroscopic data. Above this energy, the population of electrons in the plasma is too small to be reflected in the spectroscopic data. Here, an upper limit can be stated for the electron population. Non-thermal features, the steepening of the EEDF in the region of the excitation threshold, are significantly reconstructed from the spectroscopic data.

### Axially Resolved Measurements

The plasma volume, which is imaged onto the optical fiber of the spectrometer, has the form of a double-cone with a diameter of  $\approx 1$  mm (cf. 5.7). By moving the discharge tube relative to the imaging optic, spatially resolved measurements are possible. In the following section, the results from axially resolved measurements of the anode- and cathode region of the discharge are presented. In these regions, the discharge current has to pass through the interface between

the plasma and the conducting surfaces of the electrodes, where a complicated, two-dimensional spatially inhomogeneous plasma is found.

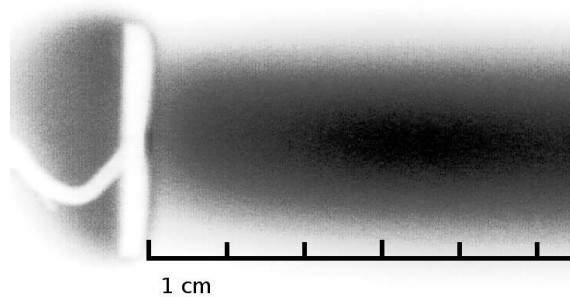


**Figure 7.18.:** Light emission in the anode region of a stable neon dc discharge. (discharge parameters:  $I = 10\text{ mA}$ ,  $p_0 = 120\text{ Pa}$ ,  $r_0 = 1.15\text{ cm}$ ) On the left, the anode can be seen, which is covered by a luminous layer. The emission is obtained from a digital photography (light emission is shown in dark). The approximate scale is given for orientation.

**Anode** The interaction between anode and plasma reaches a distance into the plasma given by roughly one electron energy relation length  $\lambda_e$ , which is the distance an electron has to travel along the electric field in the positive column of the plasma to gain the energy needed to excite a neutral atoms in the plasma. Close to the anode (roughly one Debye radius), the anode fall appears, where the potential drops from a value of a few electron Volts (depending on discharge parameters, a typical value is  $\sim -7\text{ eV}$ ) to the ground potential of the conducting anode. In Fig. 7.18, the light emission in the anode region of a stable neon dc-discharge is shown. The thin luminous layer in front of the anode on the left of the figure, shows the extension of the anode fall ( $< 2\text{ mm}$ ). The brightness reaches the full value of the positive column at a distance of  $2..3\text{ cm}$  from the anode. This behavior can also be identified in Fig. 7.21, where the relative axial variation of the intensity is shown. The right part of the figure shows results from literature<sup>8</sup>. Here, the anode-sheath can clearly be observed in the variation of the emission intensity, while the spectroscopic measurement in front of the anode does not show an increased intensity. The reason for this, is the spatial resolution of the used line-of-sight. The line-of-sight which is closest to the anode actually covers a part of the dark anode. The average energy (Fig. 7.20) reconstructed for this measurement, however, shows, that the anode sheath was clearly captured.

In Fig. 7.19, the result of the reconstruction at different axial positions in front of the anode is shown. The measurements were performed for a dc discharge in neon with a neutral gas pressure  $p_0 = 120\text{ Pa}$ , a discharge current of  $I = 10\text{ mA}$ , and a tube radius of  $r_0 = 1.15\text{ cm}$ . Although the axial distribution of the light intensity varies strongly (Fig. 7.21), the shape of the reconstructed EEDF does only shows subtle variations. The EEDF found next to the anode, however, shows a significantly different shape than the EEDF in the positive column, with a strongly increased average energy. In Fig. 7.20, the actual EEDF (normalized to one) is shown together with the average energy of the distribution.

In Fig 7.21, the axial distribution of average energy, electron density and light emission intensity are shown. The electron density starts to fall of at a larger distance to the anode, than the light emission. At distances between  $\sim 3$  and  $\sim 5\text{ cm}$  from the anode, the influence of the reduced electron density on the light emission is compensated by an increase of the average energy of the electrons. According to the result, shown in Fig. 7.21, the electron density falls to one third of the density in the positive column before the electrons enter the region of the anode fall, where it is decreased

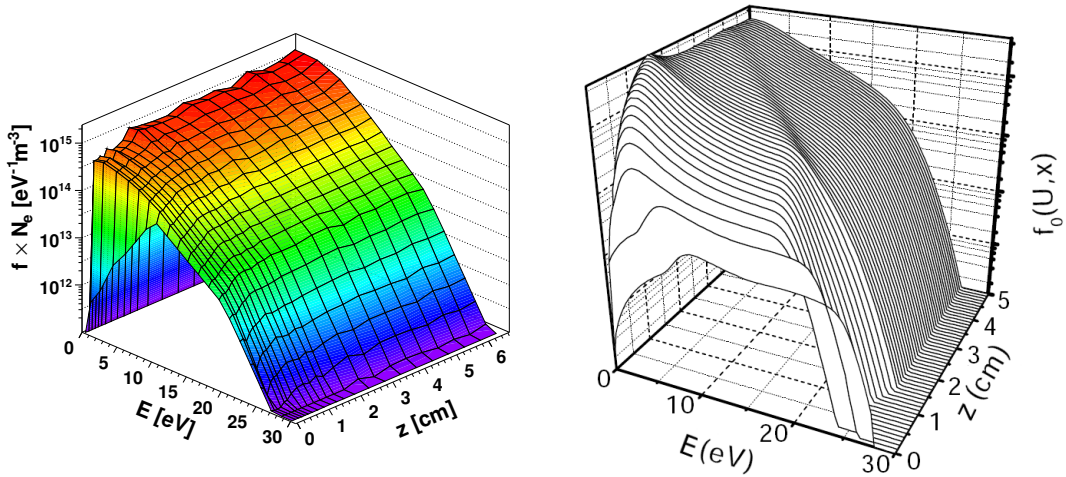


**Figure 7.19.:** Result of the reconstruction of the EEDF from spectroscopic data at different axial positions ( $z$ ) in front of the anode (left). The vertical axis depicts the number of electrons per energy interval per volume on a logarithmic scale, only the median of the marginal distribution is shown, for reasons of clarity. The right part of the figure shows results from kinetic modelling, (picture taken from Ref. <sup>8</sup>). The anode is located at  $z = 0$  cm in both cases.

to 5% of the value in the positive column. Notably, the early decrease of the electron density, accompanied by a slight increase in average energy, as known from probe measurements<sup>8,11</sup>, is near the limit of the significance of the reconstruction.

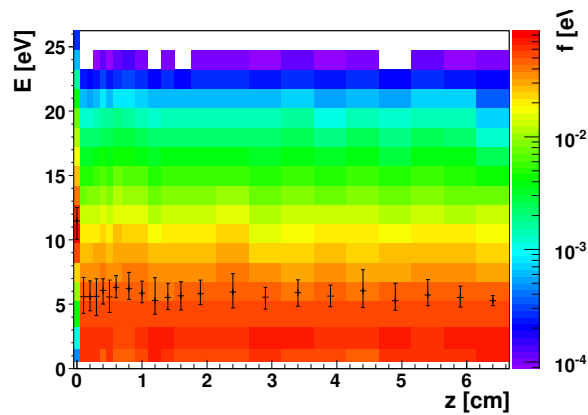


**Figure 7.20.:** The EEDF without electron density (normalized to one) for different axial positions  $z$  in front of the anode. The anode is located at  $z = 0$  cm. The value of the EEDF is shown by the color-code. The points with error bars, indicate the average energy (ordinate) as obtained by the MC sampling. The error of the average energy is obtained from the 0.16 and 0.84 quantile of the marginal distributions.

In general can be observed, that the decline of the light emission in front of the anode is mainly caused by a reduced electron density, rather than a change of the energy distribution of the electrons. Quite contrarily, a slightly increased average energy is found in front of the anode. The small variation of the energy distribution, as well as the decay of the electron density over a distance of a few centimeters, which is much longer than any considerable variation of the axial electric field<sup>8,14</sup>, indicate a diffusive transport of the electrons towards the anode, which absorbs electrons approximately independent from their energy. If the velocity distribution of the electrons

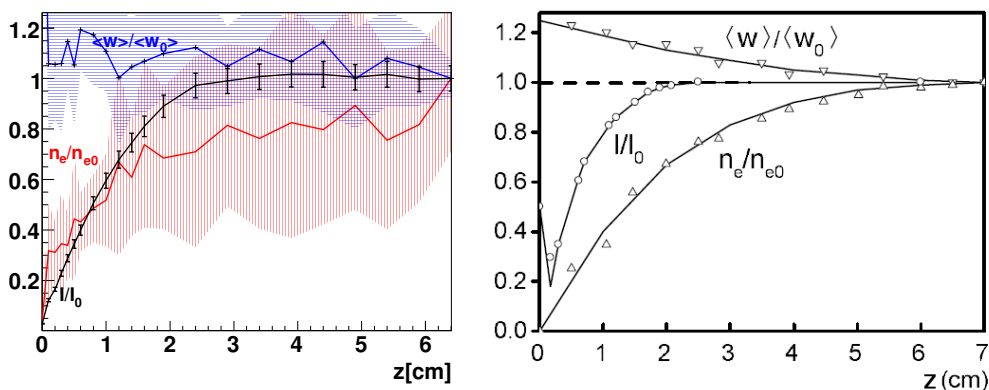


**Figure 7.21.:** Relative axial distributions of plasma parameters in the anode region. The values obtained from the reconstruction of spectroscopic data (left) are compared to results from kinetic modelling (picture taken from Ref.<sup>8</sup>). The average energy  $\langle w \rangle / \langle w_0 \rangle$ , the electron density  $n_e / n_{e0}$  and the intensity of the light emission  $I / I_0$  are shown normalized with respect to their values in the positive column. The shaded areas in the left plot show the uncertainty (experimental and atomic data set) as obtained by the MC sampling (0.16 and 0.84 quantile of marginal distributions). The average energy of the spectroscopic measurement closest to the anode is out of scale here, it can be seen in Fig. 7.20. The result from Ref. (<sup>8</sup>) refer to a neon discharge with  $I = 10$  mA,  $p = 133$  Pa,  $r_0 = 1.5$  cm, the spectroscopic data was obtained for the parameters:  $I = 10$  mA,  $p = 120$  Pa,  $r_0 = 1.15$  cm.

would have a strong anisotropy, corresponding to a flow-like transport, rather than diffusion, the electron density would not decrease in front of the anode (In the limit of a directed beam towards a perfect absorbing anode, the electron density is constant). The small variation of the shape of the EEDF favors an energy independent absorption of electrons at the anode. If there were preferred energies, at which electrons would be reflected from the anode and could escape from the anode fall region, the shape of the EEDF would be influenced. In consistence with this considerations, a finite value of the electron density is found in front of the anode fall by the reconstruction of the spectroscopic data. Unlike shown in the right part of Fig. 7.21, a finite electron density in front of the anode is observed in probe measurements<sup>11</sup> and modelling<sup>14</sup>. Assuming the validity of the the picture given above, the increased anisotropy<sup>14</sup> in the region of the anode fall, caused by the electric field next to the anode, leads to a flattening of the electron density distribution in the region of the anode fall ( $z \lesssim 2$  mm).

The average energy of the spectral measurement next to the anode shows an average energy, which is increased by 6 eV compared to the average energy of the next measurement. This is in agreement with the magnitude of the anode fall considered in Refs. (<sup>8,14</sup>), which is 5 to 6 eV, and to the increase in average energy next to the anode given in Ref. (<sup>14</sup>), which is 3 to 6 eV larger than in the positive column. The relative electron density of 0.05, which was reconstructed from the spectral measurement next to the anode, most probably underestimates the actual density, as the line-of-sight of the spectrometer must have covered a part of the anode, causing an overestimation of the emitting plasma volume. The values for the electron density observed in probe measurements<sup>11</sup> and modelling<sup>14</sup> of discharge in neon with similar parameters are in the region of 10% of the value of the positive column, which is in reasonable agreement with an interpolation of the axial distribution shown in the left part of Fig 7.21.

In Fig. 7.22, the axial distribution of the average energy obtained from probe measurements is shown. The behavior in front of the anode is similar to the result obtained from the analysis of the

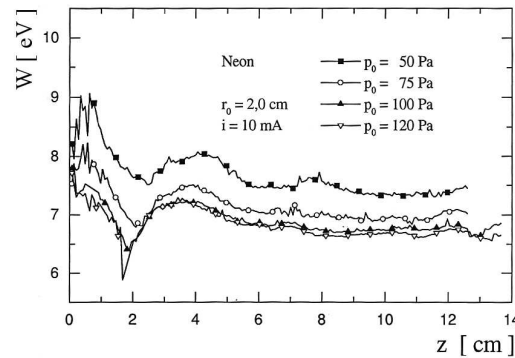


**Figure 7.22.:** Axial distribution of the average energy of the electrons in neon discharges at different pressures, obtained by probe measurements (picture taken from Ref. <sup>11</sup>). The average energy  $W$  (ordinate) is shown as function of the axial position, the anode is located at  $z = 0$  cm. The parameters of the discharges are indicated in the plot.

spectroscopic data. Starting from the positive column, the average energy first rises slowly, then a local minimum can be found between one and two centimeters distance from the anode. Finally, the average energy rises slowly before the anode fall is reached. Inside the anode fall, no probe measurements are possible, while the spectroscopic approach allows to see the strong increase of average energy.

The local minimum in front of the anode coincides with the peak of slow electrons that can be found in the EEDF from kinetic modelling<sup>8</sup> shown in the right part of Fig. 7.21. The appearance of a peak of slow electrons, is an indication for the flattening of the plasma potential in front of the anode, reflecting the accumulation of positively charged ions in front of the anode. In the calculations of Ref. (<sup>8</sup>), the position of the peak of electrons coincides with the position of the space charge, i.e. the position where the potential gradient changes its slope.

**Cathode** The plasma of the negative glow and in the vicinity of the cathode is, in comparison to the positive column, characterized by distinct spatially inhomogeneity and complex kinetic processes. The strong electric field next to the cathode lead to electron distributions far from thermodynamic equilibrium. A qualitative picture of the processes generally observed in the cathode region of a gas discharge is given in 2.2.1. In the following section, the results for the reconstruction of the electron energy distribution at different axial positions close to the cathode are presented. The measurements were made on a stable glow discharge in neon with a discharge current  $I = 10$  mA, a neon gas pressure of  $p_0 = 120$  Pa, and a tube radius of  $r_0 = 1.15$  cm. The discharge tube was equipped with a cylindrical hollow cathode with a diameter of 1 cm and a length of 3 cm.

In Fig. 7.23, an overview over the Result of the reconstruction is given. The reconstructed EEDF does not show a distinct acceleration and relaxation of the electrons, like observed e.g. in low pressure helium discharges<sup>11</sup>. The variations of the EEDF, reconstructed from the emission spectra of the neon discharge, are more subtle. A flattening of the low energy part of the distribution can be observed close to the cathode. Also, some of the reconstructed EEDF in this region show two maxima, one at low energies around 2 eV and a second one, at approximately 10 eV. A possible explanation for a second maximum in the electron distribution could be the observation of secondary electrons from ionization, which have not yet gained energy and fast electrons which already have gained energy in the strong field close to the cathode. The reconstructed electron density shows a

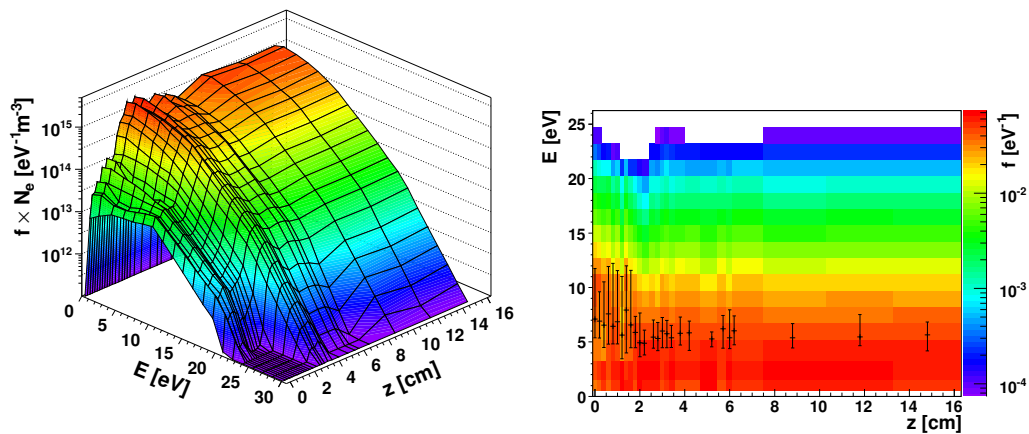


**Figure 7.23.:** Result of the reconstruction of the EEDF from spectroscopic data at different axial positions  $z$  in front of the Cathode. Left plot: The vertical axis depicts the number of electrons per energy interval per volume on a logarithmic scale, only the median of the marginal distribution is shown, for reasons of clarity. Right plot: The EEDF without electron density (normalized to one) for different axial positions  $z$  in front of the cathode. The value of the EEDF is shown by the color-code. The points with error bars, indicate the average energy (ordinate) as obtained by the MC sampling. The error of the average energy is obtained from the 0.16 and 0.84 quantile of the marginal distributions. The cathode is located at  $z = 0$  cm. The

strong variation of a factor of roughly 100 between the maximal density in the negative glow and the minimum close to the cathode.

In Fig. 7.24, the relative axial distributions of the light emission and the reconstructed electron density and average electron energy are shown. Like in the anode region, the variation of the light emission is closely connected to a variation of the electron density, while the reconstructed average energy only shows a slight variation.

In the right part of Fig. 7.24, the reconstructed average energy is compared to a line ratio obtained from the spectra that were reconstructed. The distribution of the light emission is shown for orientation. The line ratio, that is shown, is obtained from the intensity of the line at  $\lambda = 640.2$  nm (transition  $3p_9 \rightarrow 3s_4$ ) divided by the intensity of the line at  $\lambda = 607.43$  nm (transition  $3p_3 \rightarrow 3s_3$ ). As can be seen in Fig. ??, the  $3p_9$  state is only populated via excitation from ground state, while the  $3p_3$  also shows a significant contribution from stepwise excitation via the metastable  $3s$  states. Consequently, the line ratio of the two dominant decay channels of these states is sensitive to the ratio of the electrons populations in the region of  $\sim 8$  eV and 22 eV.

The axial variation of the line ratio reflects a behavior of the electrons, which is consistent with the picture of the processes in the discharge as described in 2.2.1: In the Aston dark space, the number of higher energetic electrons rises until a region is reached where strong ionization leads to a steep rise of the electron density and subsequent light emission (negative glow). The cathode glow and cathode darks space, which would be found in front of the region of high ionization cannot be distinguished in the discharge under consideration. In the vicinity of the negative glow, a large space-charge of positive ions builds up and shields the positive column from the strong fields of the cathode. The number of high energetic electrons is strongly reduced by the energy loss in ionization and excitation processes, which is compensated by the weak electric field behind the negative glow. The region of weak field is called the Faraday space. Here, the electric field and light emission gradually increase to their values in the positive column.



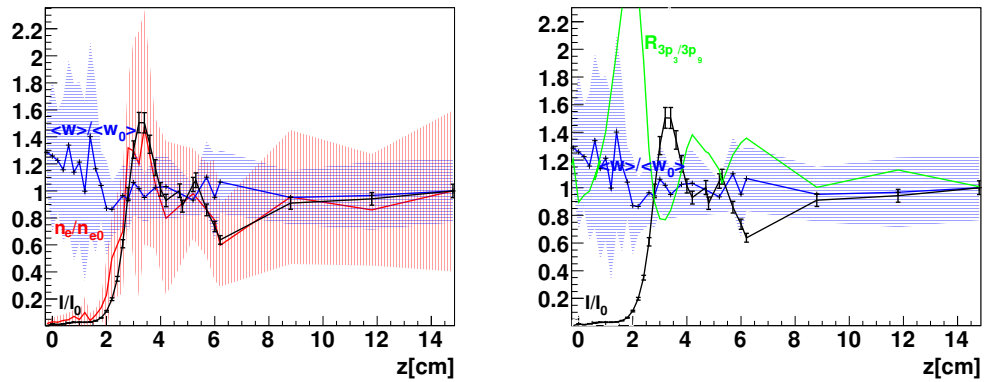


**Figure 7.24.:** Relative axial distribution of different plasma parameters in the cathode region. On the left, the average energy  $\langle w \rangle / \langle w_0 \rangle$ , the electron density  $n_e / n_{e0}$  and the intensity of the light emission  $I / I_0$  are shown normalized with respect to their values in the positive column. The shaded areas show the uncertainty (experimental and atomic data set) as obtained by the MC sampling (0.16 and 0.84 quantile of marginal distributions). On the right, the average energy is compared to the ratio  $R_{3p_0/3p_3}$  of two line intensities with two initial states in the 3p-multiplet showing a energy dependent population. Large values of the ratio correspond an increase of higher energetic electrons.

The average energy shown in Fig. 7.24, does not reflect the physical processes as discussed above and shown by the line ratio in the right part of the figure. The increase of energy in the Aston dark space can not be observed in the average energy. On the contrary, the average energy seems to decrease in the first two centimeters after the cathode. A possible explanation for this behavior is the division of the electron population in a low and high energy part, described above, as a multi-modal distribution cannot not be appropriately characterized by its first moment. On the other hand, the shape of the distributions (Fig. 7.23) does also not show a clear increase of high energetic electrons. The shape of the EEDF in the negative glow, showing a large fraction of low energy electrons, is consistent with the physical picture, again.

### 7.2.2. Validation of Atomic Data

The spectroscopic data contains information about the physical processes of the plasma. The rate coefficients for the electron excitation of the gas atoms depend on the EEDF, but also on the respective cross-section. The relative intensities of lines with the same initial state carry precise information about the branching ratios of the underlying transitions. It is a feature of the probabilistic data analysis, that the data model is not only inverted with respect to the parameters of primary interest, associated with EEDF of the plasma, but also concerning other parameters. The Monte-Carlo sampling automatically reveals the information that the spectral data contains about the other model parameters.

The atomic data used for the collisional-radiative model is a consistent set of cross-sections and transition probabilities from B-spline R-Matrix calculations<sup>38</sup> (cf. 2.3). In collaboration with the authors of these calculations, the uncertainties of the data were estimated (cf. 6.3.2). The proper treatment of the atomic data and its uncertainties is a crucial part of the analysis. Unavoidable errors in the atomic data needed as input for the plasma model lead to a failure of the form-free reconstruction of the EEDF, when the uncertainty is not identified correctly (cf. 6.3.2). As the experiments for the determination of excitation cross-sections require a considerable effort, only a

part of the atomic data base has been validated experimentally. Further validation of the theoretical results is very important for the practical application of the data, as well as for the development of theoretical models.

In section 7.1.2 the potential of the integrated data analysis approach for the validation of atomic data is discussed based on the reconstruction of 'synthetic' data. It was found, that the spectroscopic data is sensitive to the consistent incorporation of Einstein coefficients, for which no experimental data is available from NIST<sup>37</sup> and that information about rate coefficients of the electron excitation of a part of the higher excited states can be gained from the spectroscopic data.

### Influence of Continuum-Coupling

As mentioned in 2.3, the correct calculation of excitation cross-sections at intermediate energies (in the region of the ionization threshold) requires the description of coupling to high lying Rydberg states and the ionization continuum. A approximate description of the ionized continuum can be obtained by the introduction of a number of pseudo-states in the R-matrix approach. Unfortunately, the number of pseudo-states needed for the accurate description of a complex target like neon is large<sup>67</sup>, and no data set obtained from a converged pseudo-state expansion is available.

The authors of Ref. (67) have performed a series of R-matrix with pseudo-state calculations in  $LS$  coupling, neglecting the complex target structure of neon. This way, the magnitude of the effects of continuum coupling could be examined. The obtained cross-sections cannot be used for plasma modelling, as the excited state of neon are no pure  $LS$  states, but the approximate mapping of the  $LS$  to the physical  $jK$  states allows to assess the importance of continuum coupling for some of excited states.

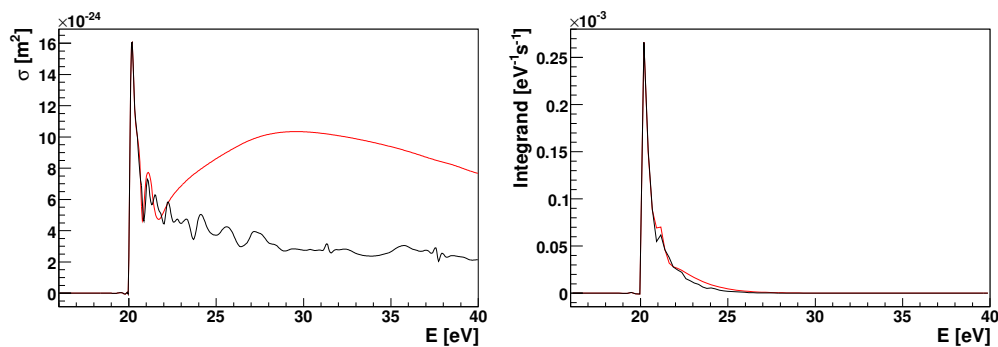


**Figure 7.25.:** Cross-section<sup>67</sup> [ $10^{-20}\text{m}^2$ ] for the excitation from the ground to the  $^3\text{P}_1$  state and the integrand entering the rate coefficient  $I(E)$  (equation 7.2). The red curve shows a 61 state R-Matrix calculation *without* pseudo-states, while the black curve depicts a 243 state RMPS calculation *with* pseudo-states. The rate coefficients obtained with the two integrands differ by a factor of 0.91.

In Fig. 7.25 and Fig. 7.25, the cross section for the  $^3\text{P}_1$  and the  $^1\text{P}_1$  state ( $LS$  coupling) are shown as obtained from R-Matrix calculation *with* and *without* inclusion of pseudo-states. The integrand of the rate coefficient (cf. 5.2) for both cross-sections is also shown in the figures:

$$I(E) = \sigma(E)f(E)\sqrt{2E/m}, \quad (7.2)$$

where the EEDF of the positive column of the discharge in neon is used. In Fig. 7.27, the factor  $f(E)\sqrt{2E/m}$  by which the cross-section is multiplied in the rate coefficient is shown. In the region above the threshold for the excitation of the 3d states, the weighting function has the shape of an

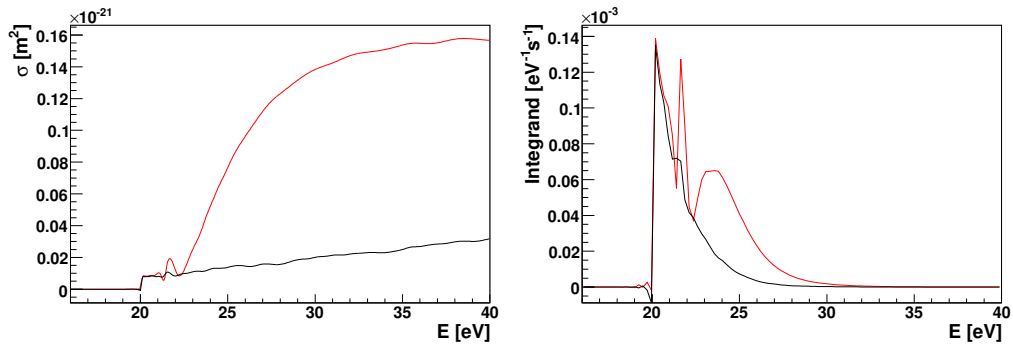


**Figure 7.26.:** Cross-section<sup>67</sup> [ $10^{-20} \text{m}^2$ ] for the excitation from the ground to the  $^1\text{P}_1$  state and the integrand entering the rate coefficient  $I(E)$  (equation 7.2). The red curve shows a 61 state R-Matrix calculation *without* pseudo-states, while the black curve depicts a 243 state RMPS calculation *with* pseudo-states. The rate coefficients obtained with the two integrands differ by a factor of 0.51.

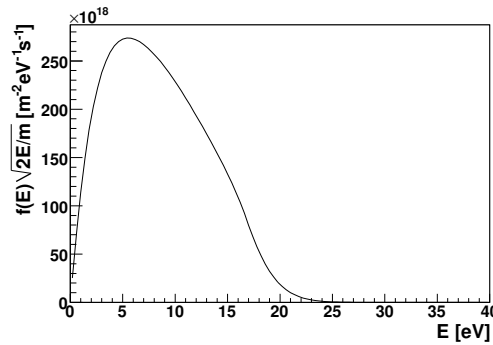


**Figure 7.27.:** Weighting function of the rate coefficient. The cross section is multiplied by this function  $f(E)\sqrt{2E/m}$  for the integration of the rate coefficient. The largest weight is at low energies where the considered cross-sections vanish. Above the threshold for the excitation of the 3d levels, the weighting function has the shape of exponentially decreasing function.

exponentially decreasing function. The correct consideration of continuum-coupling leads for the  $LS$  states to a reduction of the rate coefficient by a factor of 0.91 ( $^3\text{P}_1$ ) and 0.51 ( $^1\text{P}_1$ ), respectively.

In Fig. 7.28, the marginal distributions for the corrections of the excitation cross sections, as obtained from the analysis of the spectroscopic data from the positive column of a stable dc discharge in neon are shown (discharge parameters:  $p_0 = 89 \text{ Pa}$ ,  $I = 25 \text{ mA}$ ,  $r_0 = 1.5 \text{ cm}$ ). In table 7.5, numerical values are stated for some of the transitions. The reproducibility of the reconstructed values was verified with data obtained for different discharge parameters ( $p_0 = 120 \text{ Pa}$ ,  $I = 10 \text{ mA}$ ,  $r_0 = 1.15 \text{ cm}$  and with spectra from different axial positions and currents in both discharges. The robustness against modifications of the data model, that are within the scope of certain approximations (cf. 7.1.3) was checked. The median of the marginal distribution is given together with asymmetric error margins obtained from the 0.16 and the 0.84 quantile of the distribution. Note that for the transitions to the 3d multiplet a numerical value of roughly  $0.85^{+0.6}_{-0.35}$  corresponds to the pure prior information, i.e. scale factors for which the spectral data is not sensitive<sup>§</sup>.

<sup>§</sup>The asymmetric shape of the log-normal distribution leads to a median of 0.85 for log-normal with a mean of one and a standard deviation of 0.6, cf. Fig7.28. This asymmetry reduces the clarity of the presentation of the result, but has a small effect if the spectroscopic data is informative. Other priors might be used for future analysis.

The two large expected corrections for the  $3d_7$  and the  $3d_1$  level are clearly confirmed by the spectroscopic data, verifying the transferability of the results obtained by the *LS* coupling calculations of Ref. (67) to the actual excited states of the neon. Other large corrections are observed for the ground  $\rightarrow 3d_3$  and the  $3d_4 \rightarrow 3d_5$  transition. The other correction factors lie in the range of 0.6 to 1.3. This is not unexpected, as the relative uncertainty of the excitation cross-sections was estimated with 60%. For many of the excitations from the  $3s_4$  state, a reduction is preferred by the spectroscopic data.

For the excitation of the  $3d_{11}$  state, a more pronounced reduction of the rate coefficient was found by the analysis of the spectroscopic data, than expected by the convergence study of Ballance. Given the overall distribution of the correction factors, this is not necessarily an indication for a larger effect of the continuum-coupling, but could also be explained by the generally moderate accuracy of the calculations for the cross-sections for excitation of states in the 3d-multiplet.

### Einstein Coefficients

In Fig. 7.30 the marginal distributions of the Einstein coefficients, as obtained from the analysis of the spectroscopic data from the positive column of a stable dc discharge in neon are shown (discharge parameters:  $p_0 = 89$  Pa,  $I = 25$  mA,  $r_0 = 1.5$  cm.). The width of the distribution is generally smaller than for the scale factors. (See Fig. 6.1, for the prior uncertainties of the Einstein coefficients) This reflects the fact, that accuracy of the transition probabilities obtained from atomic structure calculations is higher than the accuracy of the excitation cross-sections. Also here, the reproducibility for different discharge conditions and the robustness against model approximations was studied (cf. 7.1.3).

In table 7.6, the numerical values for Einstein coefficients are given, which could be validated by the analysis of spectroscopic data. Overall, a good agreement between the spectroscopic data and the results from atomic structure calculations<sup>38</sup> could be found. Only for a small number of number of transitions, a slightly significant deviation is found by the spectroscopic measurement.

For the  $3d_1 \rightarrow 3p_7$  transition, the result from the spectroscopic data lies closer to the NIST value than the result from the structure calculations. For other transitions ( $3d_7 \rightarrow 3p_7$ ,  $3d_1 \rightarrow 3p_5$ ) the result of the BSRM calculations could be confirmed. The value obtained for the Einstein coefficient of the  $3d_2 \rightarrow 3p_4$  transition is lower than the result of the BSRM calculation, but coincides with the NIST value within errors.

In Fig. 7.29 the part of the emission spectrum is shown, where the lines from transitions with initial state in the 3d-multiplet are found. Although not all lines can be well resolved by the simple spectrometer, the precise knowledge about the apparatus function of the spectrometer allows the analysis of this part of the spectrum.

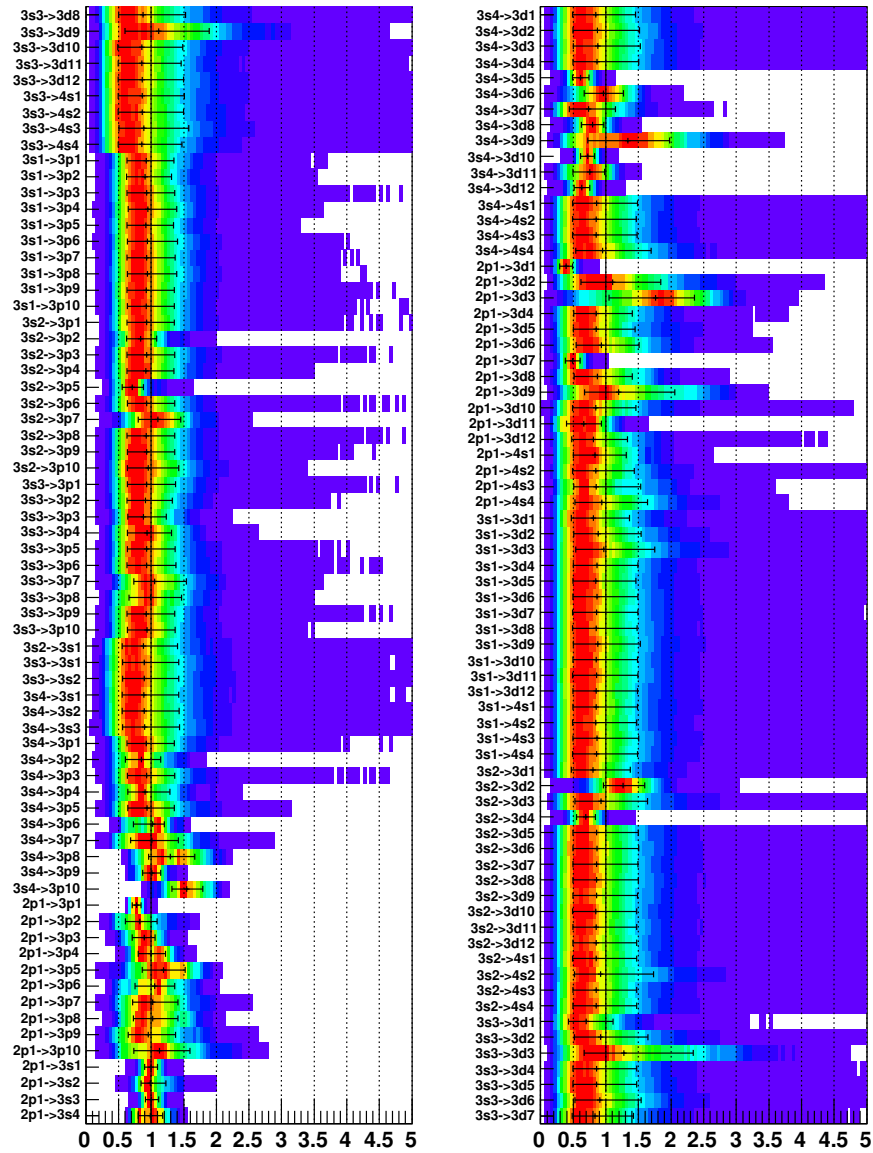


**Figure 7.28.:** Marginal probability distributions for correction factors for the cross sections entering the collisional radiative model obtained from the analysis of spectroscopic data. Each row in the plot corresponds to one correction factor. The respective transition is labelled on the left. A value of one corresponds to the original cross section. The error bars, which are also shown are obtained from the 0.16, the 0.5 (median) and 0.85 quantile of the distribution.

**Table 7.5.:** Experimentally determined correction factors for the cross-sections to the 3d and 3p levels. The corrections are given for cross-sections of excitation from the *ground* state and the *three lowest* 3s states. Where the inference from the spectroscopic data yields no additional information, the correction is shown in gray. In some cases the *sum* of the corrections for excitation from the ground plus and the excitation from the 3s<sub>4</sub> state is better determined than the individual corrections (cf. 7.1.2), in these cases the sum is given in the rightmost column. The results of the convergence study by Ballance<sup>67</sup> are given in the column labelled “RMPS” (cf. Fig.7.25 and Fig. 7.26), the numbers are directly comparable to the correction of the excitation from ground state, which is stated in the next column.

final-state	RMPS	ground	3s <sub>4</sub>	3s <sub>3</sub>	3s <sub>2</sub>	gr+3s <sub>4</sub>
3d <sub>12</sub>	1	0.81 <sup>+0.52</sup> <sub>-0.33</sub>	0.63 <sup>+0.12</sup> <sub>-0.12</sub>	0.85 <sup>+0.61</sup> <sub>-0.36</sub>	0.85 <sup>+0.6</sup> <sub>-0.35</sub>	1.5 <sup>+0.44</sup> <sub>-0.3</sub>
3d <sub>11</sub>	0.9	0.66 <sup>+0.27</sup> <sub>-0.26</sub>	0.75 <sup>+0.23</sup> <sub>-0.26</sub>	0.85 <sup>+0.59</sup> <sub>-0.36</sub>	0.85 <sup>+0.6</sup> <sub>-0.35</sub>	1.4 <sup>+0.16</sup> <sub>-0.15</sub>
3d <sub>10</sub>		0.84 <sup>+0.59</sup> <sub>-0.35</sub>	0.72 <sup>+0.11</sup> <sub>-0.1</sub>	0.85 <sup>+0.6</sup> <sub>-0.36</sub>	0.84 <sup>+0.6</sup> <sub>-0.35</sub>	
3d <sub>9</sub>		1.2 <sup>+0.84</sup> <sub>-0.52</sub>	1.3 <sup>+0.64</sup> <sub>-0.61</sub>	1.1 <sup>+0.73</sup> <sub>-0.5</sub>	0.85 <sup>+0.6</sup> <sub>-0.36</sub>	2.7 <sup>+0.54</sup> <sub>-0.51</sub>
3d <sub>8</sub>	1	0.87 <sup>+0.53</sup> <sub>-0.36</sub>	0.79 <sup>+0.17</sup> <sub>-0.17</sub>	0.87 <sup>+0.63</sup> <sub>-0.37</sub>	0.85 <sup>+0.61</sup> <sub>-0.36</sub>	1.7 <sup>+0.39</sup> <sub>-0.3</sub>
3d <sub>7</sub>	<b>0.5</b>	<b>0.49<sup>+0.11</sup></b> <sub>-0.11</sub>	0.73 <sup>+0.42</sup> <sub>-0.29</sub>	0.83 <sup>+0.58</sup> <sub>-0.35</sub>	0.85 <sup>+0.61</sup> <sub>-0.36</sub>	1.2 <sup>+0.33</sup> <sub>-0.25</sub>
3d <sub>6</sub>		0.93 <sup>+0.58</sup> <sub>-0.39</sub>	0.96 <sup>+0.3</sup> <sub>-0.3</sub>	0.9 <sup>+0.63</sup> <sub>-0.38</sub>	0.86 <sup>+0.62</sup> <sub>-0.36</sub>	2 <sup>+0.38</sup> <sub>-0.34</sub>
3d <sub>5</sub>		0.85 <sup>+0.6</sup> <sub>-0.35</sub>	0.61 <sup>+0.12</sup> <sub>-0.13</sub>	0.85 <sup>+0.6</sup> <sub>-0.36</sub>	0.85 <sup>+0.61</sup> <sub>-0.36</sub>	1.5 <sup>+0.51</sup> <sub>-0.31</sub>
3d <sub>4</sub>		0.85 <sup>+0.55</sup> <sub>-0.35</sub>	0.85 <sup>+0.61</sup> <sub>-0.36</sub>	0.85 <sup>+0.6</sup> <sub>-0.36</sub>	<b>0.69<sup>+0.15</sup></b> <sub>-0.14</sub>	
3d <sub>3</sub>		1.7 <sup>+0.58</sup> <sub>-0.71</sub>	0.87 <sup>+0.63</sup> <sub>-0.37</sub>	1.2 <sup>+0.92</sup> <sub>-0.57</sub>	0.91 <sup>+0.67</sup> <sub>-0.39</sub>	
3d <sub>2</sub>		1.1 <sup>+0.71</sup> <sub>-0.48</sub>	0.86 <sup>+0.61</sup> <sub>-0.37</sub>	0.91 <sup>+0.67</sup> <sub>-0.39</sub>	1.3 <sup>+0.34</sup> <sub>-0.3</sub>	
3d <sub>1</sub>	<b>0.5</b>	<b>0.39<sup>+0.1</sup></b> <sub>-0.094</sub>	0.84 <sup>+0.59</sup> <sub>-0.35</sub>	0.7 <sup>+0.42</sup> <sub>-0.27</sub>	0.8 <sup>+0.56</sup> <sub>-0.33</sub>	
3p <sub>10</sub>		1.1 <sup>+0.47</sup> <sub>-0.39</sub>	1.5 <sup>+0.25</sup> <sub>-0.23</sub>	0.94 <sup>+0.43</sup> <sub>-0.3</sub>	0.96 <sup>+0.46</sup> <sub>-0.32</sub>	
3p <sub>9</sub>		0.96 <sup>+0.41</sup> <sub>-0.31</sub>	1 <sup>+0.13</sup> <sub>-0.14</sub>	0.93 <sup>+0.43</sup> <sub>-0.3</sub>	0.93 <sup>+0.43</sup> <sub>-0.29</sub>	
3p <sub>8</sub>		1 <sup>+0.39</sup> <sub>-0.3</sub>	1.3 <sup>+0.37</sup> <sub>-0.33</sub>	0.99 <sup>+0.47</sup> <sub>-0.33</sub>	0.93 <sup>+0.43</sup> <sub>-0.3</sub>	
3p <sub>7</sub>		1 <sup>+0.39</sup> <sub>-0.31</sub>	1 <sup>+0.41</sup> <sub>-0.33</sub>	1.1 <sup>+0.48</sup> <sub>-0.32</sub>	1.1 <sup>+0.35</sup> <sub>-0.3</sub>	
3p <sub>6</sub>		1.1 <sup>+0.31</sup> <sub>-0.3</sub>	1 <sup>+0.18</sup> <sub>-0.3</sub>	0.93 <sup>+0.44</sup> <sub>-0.3</sub>	0.93 <sup>+0.43</sup> <sub>-0.3</sub>	2.1 <sup>+0.19</sup> <sub>-0.2</sub>
3p <sub>5</sub>		1.2 <sup>+0.33</sup> <sub>-0.33</sub>	0.94 <sup>+0.41</sup> <sub>-0.3</sub>	0.93 <sup>+0.43</sup> <sub>-0.3</sub>	0.71 <sup>+0.17</sup> <sub>-0.15</sub>	
3p <sub>4</sub>		1 <sup>+0.22</sup> <sub>-0.2</sub>	0.9 <sup>+0.38</sup> <sub>-0.26</sub>	0.94 <sup>+0.37</sup> <sub>-0.3</sub>	0.92 <sup>+0.43</sup> <sub>-0.29</sub>	1.9 <sup>+0.27</sup> <sub>-0.24</sub>
3p <sub>3</sub>		0.9 <sup>+0.17</sup> <sub>-0.18</sub>	0.93 <sup>+0.43</sup> <sub>-0.3</sub>	0.88 <sup>+0.35</sup> <sub>-0.24</sub>	0.93 <sup>+0.43</sup> <sub>-0.29</sub>	
3p <sub>2</sub>		0.82 <sup>+0.27</sup> <sub>-0.22</sub>	0.85 <sup>+0.29</sup> <sub>-0.24</sub>	0.91 <sup>+0.41</sup> <sub>-0.28</sub>	0.84 <sup>+0.24</sup> <sub>-0.22</sub>	
3p <sub>1</sub>		0.78 <sup>+0.069</sup> <sub>-0.065</sub>	0.92 <sup>+0.43</sup> <sub>-0.29</sub>	0.93 <sup>+0.44</sup> <sub>-0.29</sub>	0.93 <sup>+0.42</sup> <sub>-0.29</sub>	

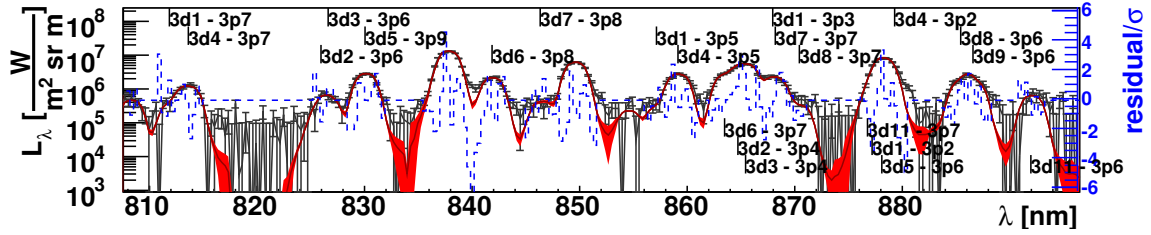


**Figure 7.29.:** Result of the model of the discharge in neon and the spectroscopic measurement. The part of the spectrum is shown, where the lines from transitions with initial state in the 3d-multiplet are found. The intensity is shown on a logarithmic scale. The red area is the result of the model and its uncertainty, the black points with error bars show the measured spectrum. The blue dashed curve shows the difference between model and measurement in units of standard deviations. The positions of the spectral lines are indicated by the labels.

**Table 7.6.:** Einstein coefficients for which inference can be made based on the spectral data, the errors are relative. In the second column, the value from the NIST<sup>37</sup> tables is given, where available. The column labels “BSRM” states the value from the atomic structure calculations<sup>38</sup> is given. Column “IDA” shows the results obtained by the analysis of the spectroscopic data. The relative errors are obtained from the 0.16 and 0.84 quantile of the distribution. The last row indicates significant deviations between “IDA” and “BSRM”.

Transition	NIST	BSRM (av)	IDA	significant
3d <sub>5</sub> → 3p <sub>9</sub>	—	1.46 · 10 <sup>7</sup> ± 0.11	1.6 · 10 <sup>7</sup> <sup>+0.09</sup> <sub>-0.08</sub>	yes
3d <sub>7</sub> → 3p <sub>8</sub>	—	3.4 · 10 <sup>6</sup> ± 0.14	3.34 · 10 <sup>6</sup> <sup>+0.11</sup> <sub>-0.1</sub>	
3d <sub>6</sub> → 3p <sub>8</sub>	—	1.62 · 10 <sup>7</sup> ± 0.10	1.73 · 10 <sup>7</sup> <sup>+0.08</sup> <sub>-0.07</sub>	
3d <sub>11</sub> → 3p <sub>7</sub>	1.1 · 10 <sup>5</sup> ± 0.5	9.2 · 10 <sup>4</sup> ± 0.21	8.94 · 10 <sup>4</sup> <sup>+0.21</sup> <sub>-0.17</sub>	
3d <sub>8</sub> → 3p <sub>7</sub>	—	1.76 · 10 <sup>6</sup> ± 0.15	1.97 · 10 <sup>6</sup> <sup>+0.15</sup> <sub>-0.13</sub>	
3d <sub>7</sub> → 3p <sub>7</sub>	2.1 · 10 <sup>7</sup> ± 0.5	1.4 · 10 <sup>7</sup> ± 0.11	1.37 · 10 <sup>7</sup> <sup>+0.09</sup> <sub>-0.08</sub>	
3d <sub>6</sub> → 3p <sub>7</sub>	—	2.36 · 10 <sup>7</sup> ± 0.1	2.23 · 10 <sup>7</sup> <sup>+0.08</sup> <sub>-0.07</sub>	
3d <sub>4</sub> → 3p <sub>7</sub>	—	1.14 · 10 <sup>7</sup> ± 0.11	1.2 · 10 <sup>7</sup> <sup>+0.08</sup> <sub>-0.07</sub>	
3d <sub>1</sub> → 3p <sub>7</sub>	4.9 · 10 <sup>6</sup> ± 0.5	3.88 · 10 <sup>6</sup> ± 0.13	4.68 · 10 <sup>6</sup> <sup>+0.13</sup> <sub>-0.11</sub>	yes
3d <sub>11</sub> → 3p <sub>6</sub>	—	5.69 · 10 <sup>6</sup> ± 0.13	6.31 · 10 <sup>6</sup> <sup>+0.11</sup> <sub>-0.10</sub>	
3d <sub>9</sub> → 3p <sub>6</sub>	—	6.25 · 10 <sup>6</sup> ± 0.12	6.34 · 10 <sup>6</sup> <sup>+0.11</sup> <sub>-0.10</sub>	
3d <sub>8</sub> → 3p <sub>6</sub>	—	1.66 · 10 <sup>7</sup> ± 0.10	1.64 · 10 <sup>7</sup> <sup>+0.07</sup> <sub>-0.07</sub>	
3d <sub>5</sub> → 3p <sub>6</sub>	—	3.08 · 10 <sup>7</sup> ± 0.1	2.78 · 10 <sup>7</sup> <sup>+0.08</sup> <sub>-0.08</sub>	yes
3d <sub>3</sub> → 3p <sub>6</sub>	—	2.98 · 10 <sup>6</sup> ± 0.14	2.91 · 10 <sup>6</sup> <sup>+0.12</sup> <sub>-0.10</sub>	
3d <sub>2</sub> → 3p <sub>6</sub>	2.03 · 10 <sup>6</sup> ± 0.25	2.05 · 10 <sup>6</sup> ± 0.15	2.14 · 10 <sup>6</sup> <sup>+0.12</sup> <sub>-0.10</sub>	
3d <sub>4</sub> → 3p <sub>5</sub>	—	3.24 · 10 <sup>7</sup> ± 0.1	3.03 · 10 <sup>7</sup> <sup>+0.08</sup> <sub>-0.07</sub>	
3d <sub>1</sub> → 3p <sub>5</sub>	5.5 · 10 <sup>6</sup> ± 0.5	3.92 · 10 <sup>6</sup> ± 0.13	4 · 10 <sup>6</sup> <sup>+0.13</sup> <sub>-0.1</sub>	
3d <sub>3</sub> → 3p <sub>4</sub>	4.45 · 10 <sup>7</sup> ± 0.25	4.22 · 10 <sup>7</sup> ± 0.1	4.17 · 10 <sup>7</sup> <sup>+0.08</sup> <sub>-0.07</sub>	
3d <sub>2</sub> → 3p <sub>4</sub>	3.91 · 10 <sup>6</sup> ± 0.25	4.03 · 10 <sup>6</sup> ± 0.13	3.4 · 10 <sup>6</sup> <sup>+0.11</sup> <sub>-0.10</sub>	yes
3d <sub>1</sub> → 3p <sub>3</sub>	—	1.5 · 10 <sup>7</sup> ± 0.11	1.42 · 10 <sup>7</sup> <sup>+0.10</sup> <sub>-0.10</sub>	
3d <sub>4</sub> → 3p <sub>2</sub>	—	5.94 · 10 <sup>4</sup> ± 0.22	5.82 · 10 <sup>4</sup> <sup>+0.24</sup> <sub>-0.20</sub>	
3d <sub>1</sub> → 3p <sub>2</sub>	1.6 · 10 <sup>7</sup> ± 0.5	1.1 · 10 <sup>7</sup> ± 0.11	9.76 · 10 <sup>6</sup> <sup>+0.11</sup> <sub>-0.10</sub>	yes

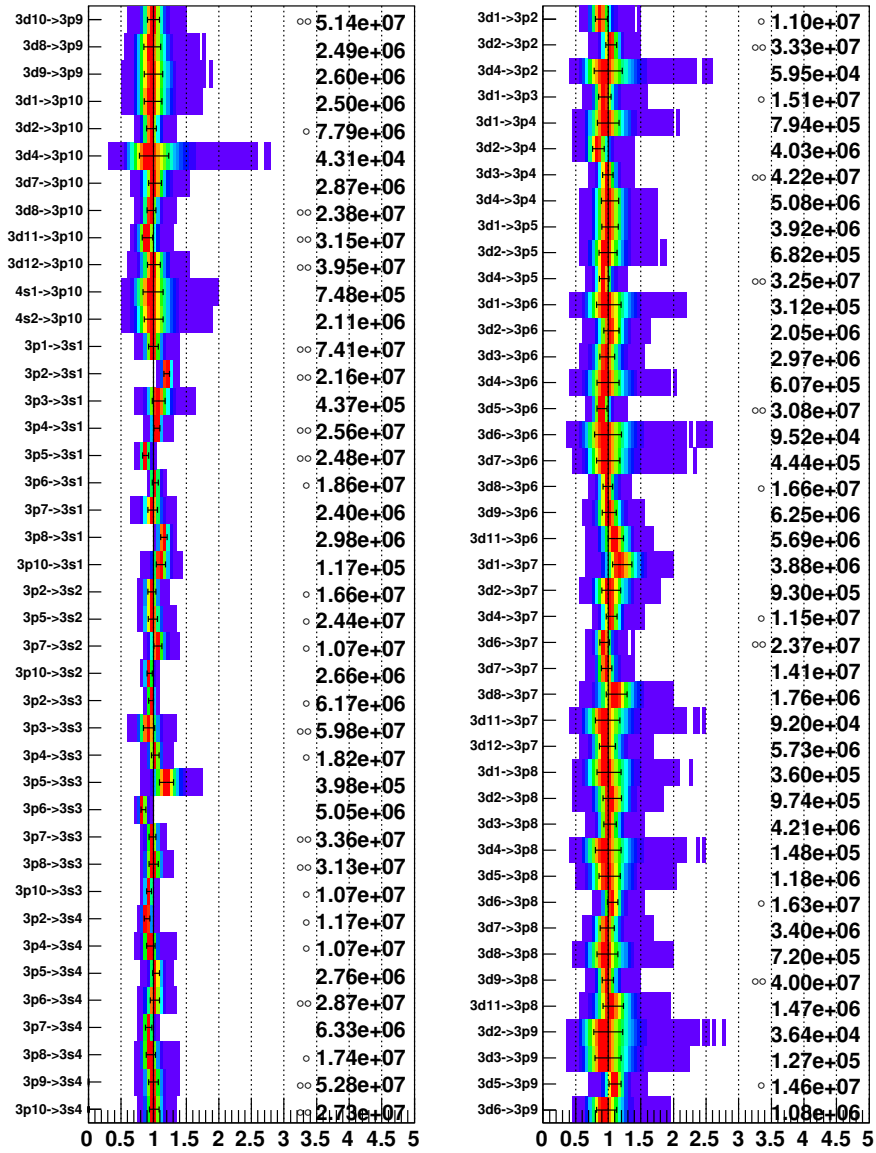


**Figure 7.30.:** Marginal probability distributions of the Einstein coefficients. Each column in the plot corresponds to a transition, which is labelled on the left. The values of the Einstein coefficients, depicted on the abscissa, are divided by the original value of the Einstein coefficient, which is also given on the right side of the plot. A value of one corresponds to the uncorrected Einstein coefficient. The error bars, which are also shown are obtained from the 0.16, the 0.5 (median) and 0.85 quantile of the distribution. Two circles in front of the value of the Einstein coefficient indicate the dominantly depopulating transition of the initial state. One circle indicates an Einstein coefficient which is greater than one fifth of the one of dominant depopulating transition.



## 8. Summary

The experimental determination of the electron energy distribution of a low pressure glow discharge in neon from emission spectroscopic data has been demonstrated<sup>68</sup>. The method extends an approach by Fischer and Dose<sup>5</sup>. The spectral data were obtained with a simple overview spectrometer and analyzed using a strict probabilistic, Bayesian data analysis. It is this *Integrated Data Analysis*<sup>2</sup> (IDA) approach, which allows the significant extraction of non-thermal properties of the electron energy distribution function (EEDF).

The results bear potential as a non-invasive alternative to probe measurements. This allows the investigation of spatially inhomogeneous plasmas (gradient length smaller than typical probe sheath dimensions) and plasmas with reactive constituents. The diagnostic of reactive plasmas is an important practical application, needed e.g. for the monitoring and control of process plasmas. Moreover, the experimental validation of probe theories for magnetized plasmas as a long-standing topic in plasma diagnostics could be addressed by the spectroscopic method.

The specific results of this thesis are:

1. The EEDF of a neon glow discharge can be reconstructed by a strict probabilistic modelling of spectroscopic data.<sup>68</sup>

The experimental and analytical effort for the demonstration of the reconstruction of the EEDF from spectroscopic data comprised the following steps:

- Experimental set-up of spectroscopic measurements (production and operation of discharges, optical setup).
- Absolute calibration of the spectral radiance and supplementary measurements for the determination of the apparatus function, effects of diffraction and reflection, linearity of the spectrometer.
- Development and implementation of a forward model<sup>69,70</sup>.
- Quantification of experimental- and model-uncertainties (with emphasis on atomic data)<sup>71</sup>.
- Implementation of Bayesian inversion techniques<sup>72</sup> (using Markov-Chain-Monte-Carlo) and parallelized computation.

The probabilistic model for the spectroscopic data consists of a stationary collisional-radiative model (CRM) describing the population densities of excited atoms in the plasma, and a description of the spectroscopic measurement. The radiation transport in the plasma is taken into account using effective lifetimes (escape factors) for the respective transitions. For transitions with a final state in the 3s multiplet, corrections for the non-homogeneity of the absorber density are included in the computation of the escape factors. The apparatus function of the spectrometer is obtained from measured spectra with high precision. The data model delivers a consistent and unbiased description of every feature of the measured spectrum in the wavelength range from 550 to 900nm. This has not been achieved before

and is possible due to the employment of an extensive and consistent data set of atomic data from B-Spline R-Matrix calculations<sup>38</sup>.

The high precision of the model allows the form-free reconstruction of the EEDF. The EEDF of the plasma is parameterized using a very flexible, spline based implementation, allowing the description of a wide class deviations from a thermalized distribution.

The form-free reconstruction<sup>73</sup> also requires a thorough incorporation of the uncertainties of the atomic data set. Unavoidable errors in the atomic data set lead to contradictions of the analysis concerning the electron distribution, which is over-determined by the large number of considered spectral lines. These contradictions are resolved, and an unbiased reconstruction is achieved, by quantifying the correct uncertainty of each element of the atomic data set for the probabilistic model.

In conclusion, the successful extension of a former study<sup>5</sup>, by applying the method on a complex atomic system, indicates the potential of the method for a wider range of applications.

2. The method is sensitive to non-thermal features of the EEDF.

The electron distribution obtained for the positive column of the plasma is in good agreement with results from self-consistent kinetic models<sup>13</sup> and probe measurements<sup>11</sup>. Non-thermal features of the EEDF, like the steepening at the excitation threshold are significantly reconstructed by the IDA approach.

3. The approach can be applied to spatially inhomogeneous plasmas.

The simulation of the full measured spectrum extends the work in Ref. (5) allowing for spatially resolved measurements. The reconstruction of the EEDF in the inhomogeneous anode- and cathode regions of a discharge in neon has been demonstrated. In the anode region, the increase of the electron energy in the narrow region of the anode fall (about 1 mm in front of the anode), which is not accessible by probe measurements<sup>11</sup>, could be observed for the first time. The obtained spatial variation of the EEDF and the electron density is consistent with the qualitative picture of the processes in front of the anode. Indications are found for a low energetic electron population, which is connected to the formation of a positive space-charge in front of the anode<sup>8</sup>.

In the cathode region, the increase of the electron density and the production of slow electrons in the vicinity of the negative glow can be observed. Indications are found for a division of the electron distribution in a high and low energetic part in the Aston dark space, which can possibly be attributed to secondary electrons from ionization and electrons that have been accelerated in the strong field close to the cathode.

4. Atomic data were validated and give in special cases evidence for atomic physics models.

An extensive study of errors in atomic data allowed conclusions on the validity of atomic physics models employed for the calculation of atomic data.

The set of electron excitation cross-sections and transition probabilities required for the implementation of the collisional-radiative model is taken from recent theoretic calculations. Presently, complete and detailed data sets are only available from theory. The direct validation of the excitation cross-sections requires sophisticated experiments and is only available

for a small fraction of the data. The uncertainties of the data were quantified in close collaboration with the authors<sup>38</sup> of the calculations. The probabilistic data analysis allows the validation of the model parameters with the information from the spectroscopic data. The consistence of previously unpublished transition probabilities could be confirmed experimentally. Experimental evidence on the magnitude of continuum-coupling effects in the calculation of the electron excitation cross-sections with final states in the 3d-multiplet was determined from the emission spectra.

In conclusion, the results of this thesis are an example of the benefit of advanced data analysis methods in low temperature plasma diagnostics. The use of a detailed data model allows the interpretation of experimental data obtained with a comparably low experimental effort. As an outlook, it is proposed to investigate spatial inhomogeneities in more detail, e.g., for the validation of probe theories. It is remarkable, that the increase in significance achieved by systematic Bayesian data modelling allowed to give relevant feed-back to atomic data providers. Hence, the presented approach provides a perspective for the validation of atomic physics results by simple spectroscopic experiments.



## A. Uncertainty of Transfer Function

The probabilistic model summarized in Fig. 5.8, is an example of an hierarchical model<sup>50</sup>: Formally, this manifests in the *hyper-parameters*  $s$  and  $\sigma_s$  not having a direct influence on the likelihood  $p(\vec{D}_s|\vec{s}, s, \sigma_s)$  of the data, but rather on the prior distribution of the parameters  $\vec{s}$  which enter the likelihood. In the following, the derivation of a probability distribution function for the (hyper-)parameters of interest  $s$  and  $\sigma_s$  is given according to the approach described in 6.2.

**Data Model** The data, which are considered for the estimation of the uncertainty of the apparatus function are the residuals  $\vec{D}_s = D_{s,1}, D_{s,1}, \dots, D_{s,n}$  from the superimposed spectral lines to the approximating spline as described in 5.8. As the apparatus function of the respective spectral line is measured directly, the data model is trivial here:  $D_{s,i,\text{sim}}(\vec{s}_i) = s_i$ , see also 5.8, for a description of the expression used below.

**Likelihood** The error statistics of the data are determined by the (rescaled) uncertainties of the spectral measurement, which are described in 4.2.1. This leads to a Gaussian likelihood with a width  $\sigma_{s,i}$ :

$$p(\vec{D}_s|\vec{s}, s, \sigma_s) = \prod_{i=1}^n \left\{ \frac{1}{\sigma_{s,i}\sqrt{2\pi}} \exp\left(-\frac{1}{2} \frac{(s_i - D_{s,i})^2}{\sigma_{s,i}^2}\right) \right\}. \quad (\text{A.1})$$

**Priors** The prior is composed of a part for the distribution of the different apparatus functions  $p(\vec{s}|s, \sigma_s)$  given the hyper-parameters  $s$  and  $\sigma_s$  as well as the prior distribution for the hyper-parameters  $p(s, \sigma_s)$ :

$$p(\vec{s}, s, \sigma_s) = p(\vec{s}|s, \sigma_s) \cdot p(s, \sigma_s) \quad (\text{A.2})$$

While  $p(s, \sigma_s)$  is assumed to be uniform in order to be determined by the data, the first part is a Gaussian distribution with mean  $s$  and standard deviation  $\sigma_s$ .

$$p(\vec{s}|s, \sigma_s) = \prod_{i=1}^n \left\{ \frac{1}{\sigma_s\sqrt{2\pi}} \exp\left(-\frac{1}{2} \frac{(s - s_i)^2}{\sigma_s^2}\right) \right\} \quad (\text{A.3})$$

Note, that the normalization constant is crucial here, since it contains a factor  $1/\sigma_s$ , which contains a free parameter of the posterior distribution (equation A.4).

**Posterior** Bayes' law is used to obtain the pdf for the from the given likelihood and prior distributions:

$$p(\vec{s}, s, \sigma_s|\vec{D}_s) \propto p(\vec{D}_s|\vec{s}, s, \sigma_s) \cdot p(\vec{s}, s, \sigma_s). \quad (\text{A.4})$$

**Summary** As the conditionality on the  $s_i$  is not of interest here, the posterior is marginalized over the  $s_i$  to obtain the posterior as a function of the parameters of interest  $s$  and  $\sigma_s$ :

$$\begin{aligned}
 p(s, \sigma_s | \vec{D}_s) &= \int p(\vec{s}, s, \sigma_s | \vec{D}_s) ds_1, ds_2, \dots, ds_n, \\
 p(s, \sigma_s | \vec{D}_s) &\propto \frac{1}{\sigma_s^n \cdot 2\pi} \prod_{i=1}^n \left\{ \int_{-\infty}^{\infty} \frac{1}{\sigma_{s,i}} \exp \left[ -\frac{1}{2} \left( \frac{(D_{s,i} - s_i)^2}{\sigma_{s,i}^2} + \frac{(s - s_i)^2}{\sigma_s^2} \right) \right] ds_i \right\} \\
 &= \frac{1}{(2\pi)^{n/2}} \prod_{i=1}^n \left\{ \frac{1}{\sqrt{\sigma_s^2 + \sigma_{s,i}^2}} \exp \left( -\frac{s^2 - s_i^2 - 2sD_{s,i}}{2(\sigma_{s,i}^2 + \sigma_s^2)} \right) \right\} \quad (\text{A.5})
 \end{aligned}$$

By maximizing this expression as a function of  $\sigma_s$ , for a given set of data  $\vec{D}_s$  and for  $s$  given from the approximating spline, an estimator for the variation of the apparatus function is obtained.

## B. Autocorrelation

The autocorrelation of the discrete time series  $\theta^t$  variable  $\theta$  (no index) time  $t$  lag  $k$  expectation value of stationary time series  $\theta$ , variance  $\text{Var}(\theta)$ .

$$R_k = \frac{1}{(n-k)\text{Var}(\theta)} \cdot \sum_{t=1}^n (\theta^t - \bar{\theta})(\theta^{t+k} - \bar{\theta}) \quad (\text{B.1})$$

### B.1. Non-Linear Least Squares Fit of the Autocorrelation Function

The autocorrelation as a function of the (discrete) time-lag  $k$  is fitted with an exponential decaying function  $R(k)$ :

$$R(k) = e^{-\kappa k} \quad (\text{B.2})$$

where  $1/\kappa$  is called the autocorrelation length. The residuals  $\Delta R_k$  of the fit are obtained by:

$$\Delta R_k = R_k - e^{-\kappa k}. \quad (\text{B.3})$$

The sum  $S$  of the squared residuals, which is to be minimized reads:

$$S = \sum_k (\Delta R_k)^2 \Rightarrow \frac{\partial S}{\partial \kappa} \stackrel{!}{=} 0 \quad (\text{B.4})$$

A Taylor expansion of  $R(k)$  as a function of  $\kappa$ , at the position  $\kappa^i$  (which is intended converge to the best fit value for  $\kappa$ ) is given by:

$$R(k) = R^i + R^{i'} \Delta \kappa^i + \dots, \quad (\text{B.5})$$

where the notation

$$R^i = R(k, \kappa^i) = e^{-\kappa^i k}, \quad \text{and} \quad R^{i'} = \frac{\partial R^i}{\partial \kappa} = -k e^{-\kappa^i k} \quad (\text{B.6})$$

is used. When inserting the Taylor series into the Gradient equations, these can be solved for the increment  $\Delta\kappa^i$ , which minimizes the least squares sum in the linear approximation of iteration  $i$ :

$$\begin{aligned}
 \frac{\partial S}{\partial \kappa} &= \sum_k \Delta R_k \cdot \underbrace{2 \frac{\partial(\Delta R_k)}{\partial \kappa}}_{=-R^{i'}} \stackrel{!}{=} 0 \\
 \Leftrightarrow \sum_k (R_k - R^i(k) - R^{i'} \Delta\kappa^i) \cdot (-2) &\stackrel{!}{=} 0 \\
 \Leftrightarrow \sum_k (R^{i'})^2 \Delta\kappa^i &= \sum_k (R_k - R^i(k)) \cdot R^{i'} \\
 \Leftrightarrow \Delta\kappa^i &= \frac{\sum_k (R_k - R^i(k)) \cdot R^{i'}}{\sum_k (R^{i'})^2} \\
 \Leftrightarrow \Delta\kappa^i &= \frac{\sum_k (R_k - e^{-\kappa k}) \cdot (-k)e^{-\kappa k}}{\sum_k (ke^{-\kappa k})^2} \tag{B.7}
 \end{aligned}$$





for  $\Delta \ll \pi$ :

$$\beta \approx \arcsin \left( \sin \delta_1 + \cos \left( \arcsin \left( \frac{n_{\text{luft}}}{n_{\text{glas}}} \sin \delta_1 \right) \right) \frac{d \cdot \arcsin \left( \frac{n_{\text{luft}}}{n_{\text{glas}}} \sin \delta_1 \right)}{R} \cdot \frac{n_{\text{glas}}}{n_{\text{luft}}} \right) \dots$$

$$\dots - \delta_1 - \frac{d \cdot \arcsin \left( \frac{n_{\text{luft}}}{n_{\text{glas}}} \sin \delta_1 \right)}{R} \quad (\text{C.1})$$

### C.1. Formulae for the Line-of-Sight Integration

For the line-of-sight integration (equation 5.14), the cross sectional area of the emitting plasma volume perpendicular to the line-of-sight  $A_{\perp}$  needs to be known. The formulae for its computation based on the position of the diffracted light rays enclosing the emitting volume as shown in Fig. C.2. The positions of the enclosing light rays  $g_1$  and  $g_2$  as well as the center of the line-of-

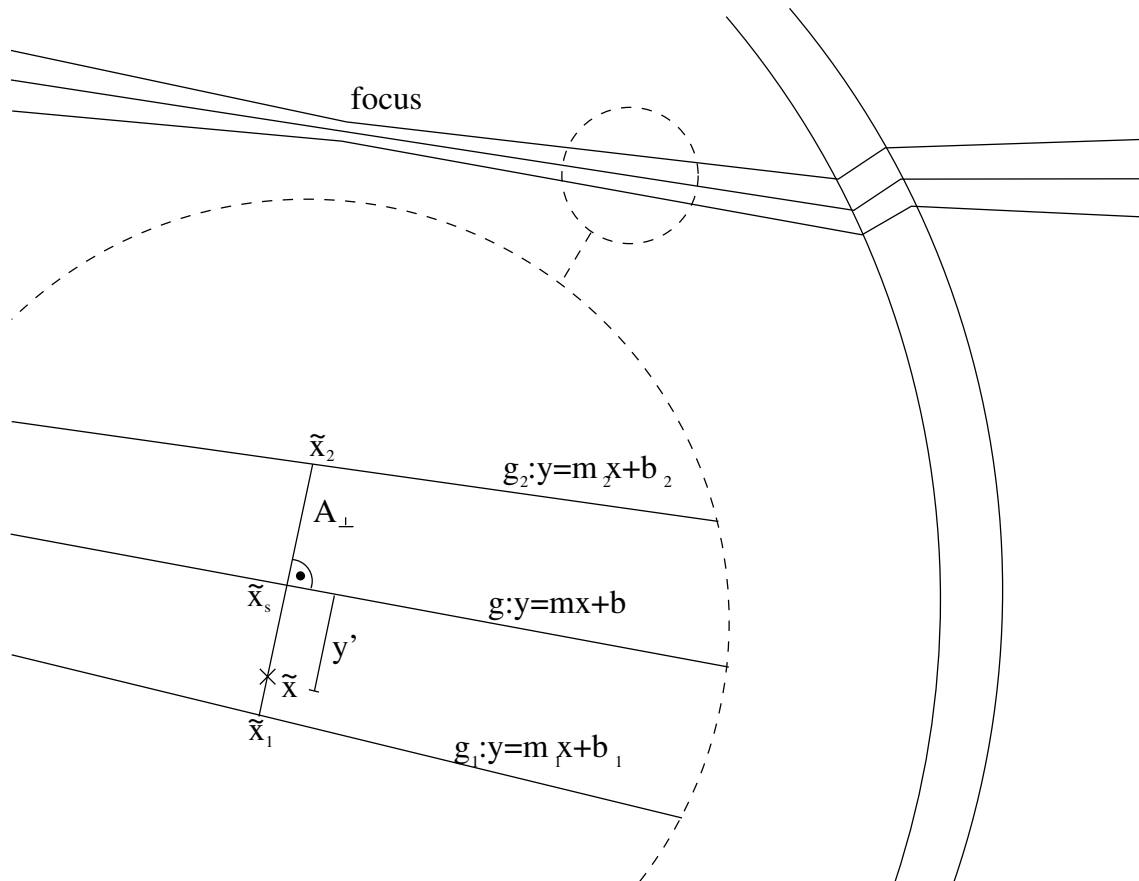


**Figure C.2.:** Influence of the refraction in the glass cylinder on the line-of-sight of the spectrometer.  $A_{\perp}$  is the area perpendicular to the central ray of the line of sight. The coordinates of the points in the sketch are:  $\tilde{x}_1 = (x_1, y_1)$ ,  $\tilde{x}_2 = (x_2, y_2)$ ,  $\tilde{x}_s = (x_s, y_s)$

sight  $g$  are determined by the geometrical dimensions of the imaging optic (Fig. C.2) and the effect of diffraction in the discharge tube. They are known in the form of line-equations in the  $x$ - $y$ -plane, from the calculations described above. For the limitation of the emitting volume in  $z$ -direction, the effect of diffraction does not need to be taken into account, because of the orientation of the line-of-sight perpendicular to the cylindrical glass tube. The minor radius of  $A_{\perp}$  is given by the

width along  $z$  of the emitting volume at the point  $\tilde{x}_s$ , where  $x_s$  is given by:

$$x_s(x, y) = \frac{|ym + x - bm|}{1 + m^2} \quad (\text{C.2})$$

The major radius of  $A_{\perp}$  is computed from the half distance between  $\tilde{x}_1$  and  $\tilde{x}_2$ :

$$R_b(x, y) = \sqrt{(x_2 - x_1)^2 + (y_2 - y_1)^2} \quad (\text{C.3})$$

$$= \frac{|(m_1(m(y - b_2) + x) - m_2(m(y - b_1) + x) + b_1 - b_2)| \sqrt{1.0 + m^2}}{2 \cdot (1 + m_1 m)(1 + m_2 m)} \quad (\text{C.4})$$

The limit of the  $z$ -Integration in equation (5.14) depends on the distance of  $\tilde{x}$  from the center of the line-of-sight, which is computed according to:

$$y'(x, y) = \frac{|y - b - mx|}{\sqrt{1 + m^2}}. \quad (\text{C.5})$$

The area of  $A_{\perp}$  is obtained from the radii:

$$A_{\perp}(x, y) = \pi R_a(x, y) \cdot R_b(x, y). \quad (\text{C.6})$$



## **D. Additional Figures**

In the following pages, additional figures are shown, giving further information supporting the consideration of chapter 7.

## D. Additional Figures

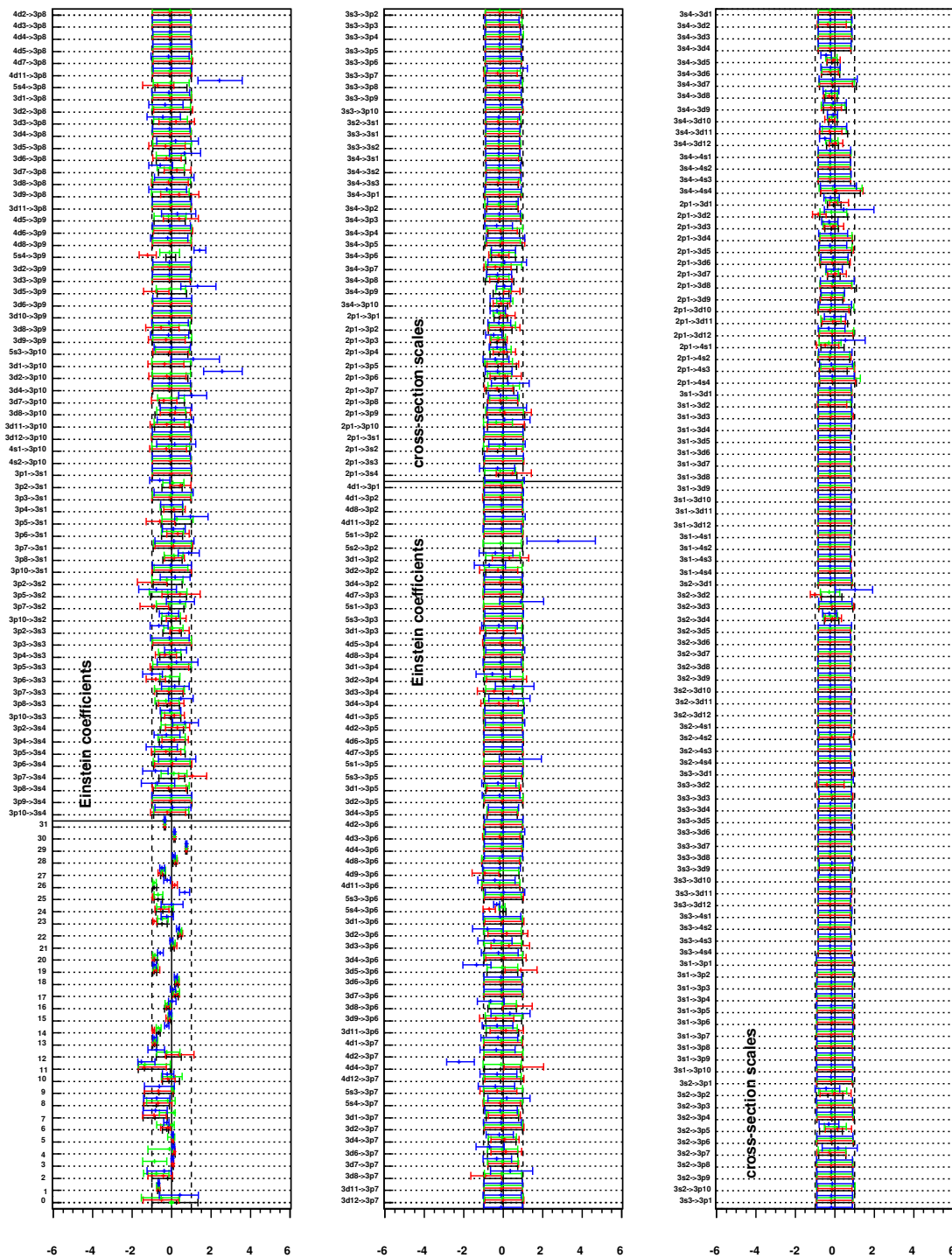
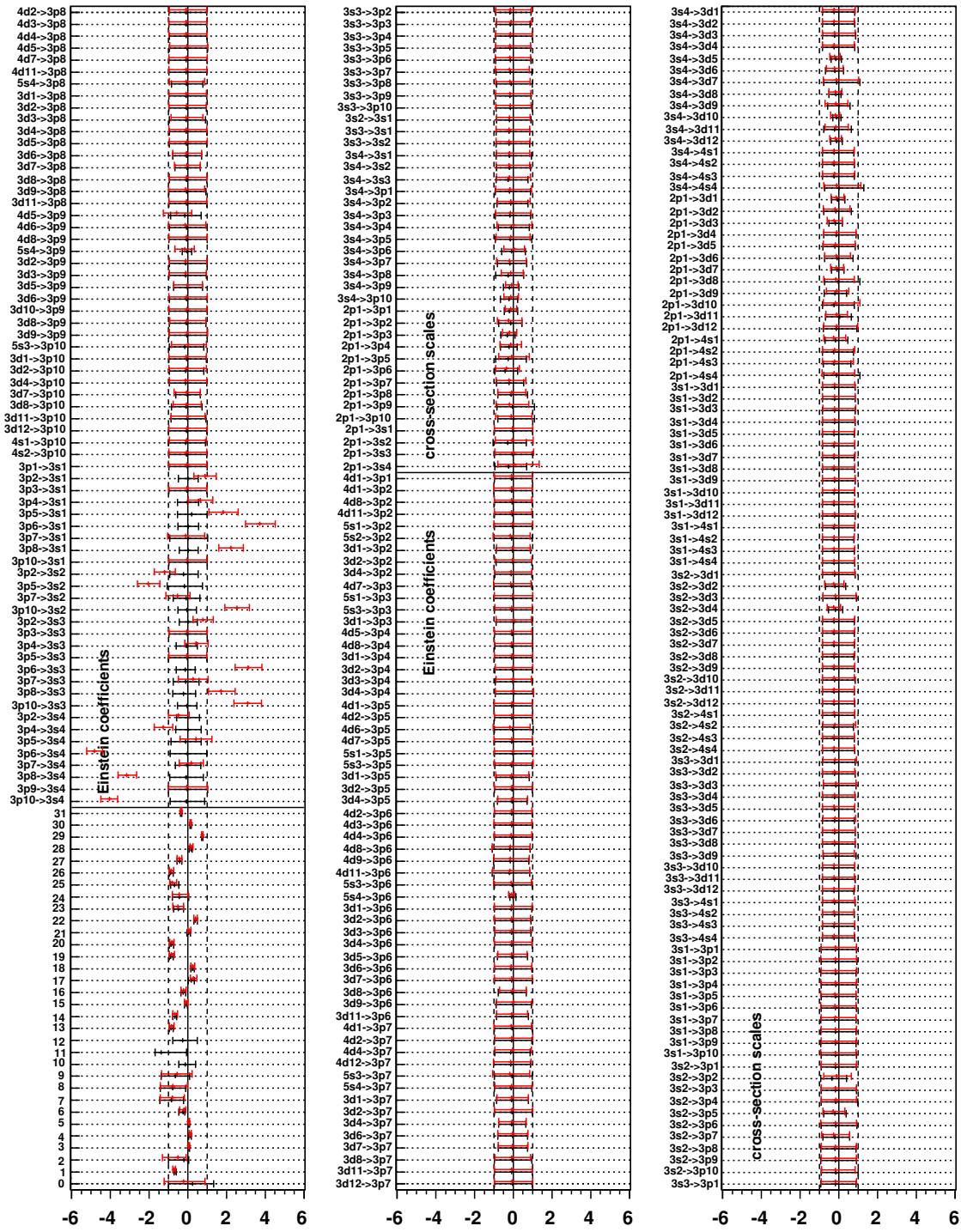


**Figure D.1.:** Influence of different model assumptions on the reconstruction of 'synthetic' data. In each row of the plot, the marginal posterior distributions of one parameter is shown, see table 7.2, in 7.1.2 for the names of the indexed parameters. The influence of different radial profiles of the densities of excited states (red), the influence of a parameterization of the EEDF with a large number of spline knots (green) and the influence of a different apparatus function (blue) are compared to the standard configuration (black). See 7.1.3 for more details of the used configurations.



— standard  
 — no 3s optical depth

Figure D.2.: Influence of different model assumptions on the reconstruction of 'synthetic' data. See also caption of Fig. D.1 The influence of a model configuration without incorporation of the escape factors of transition with a final state in the 3s-multiplet (red) is compared to the standard configuration (black), See 7.1.3, for more details.

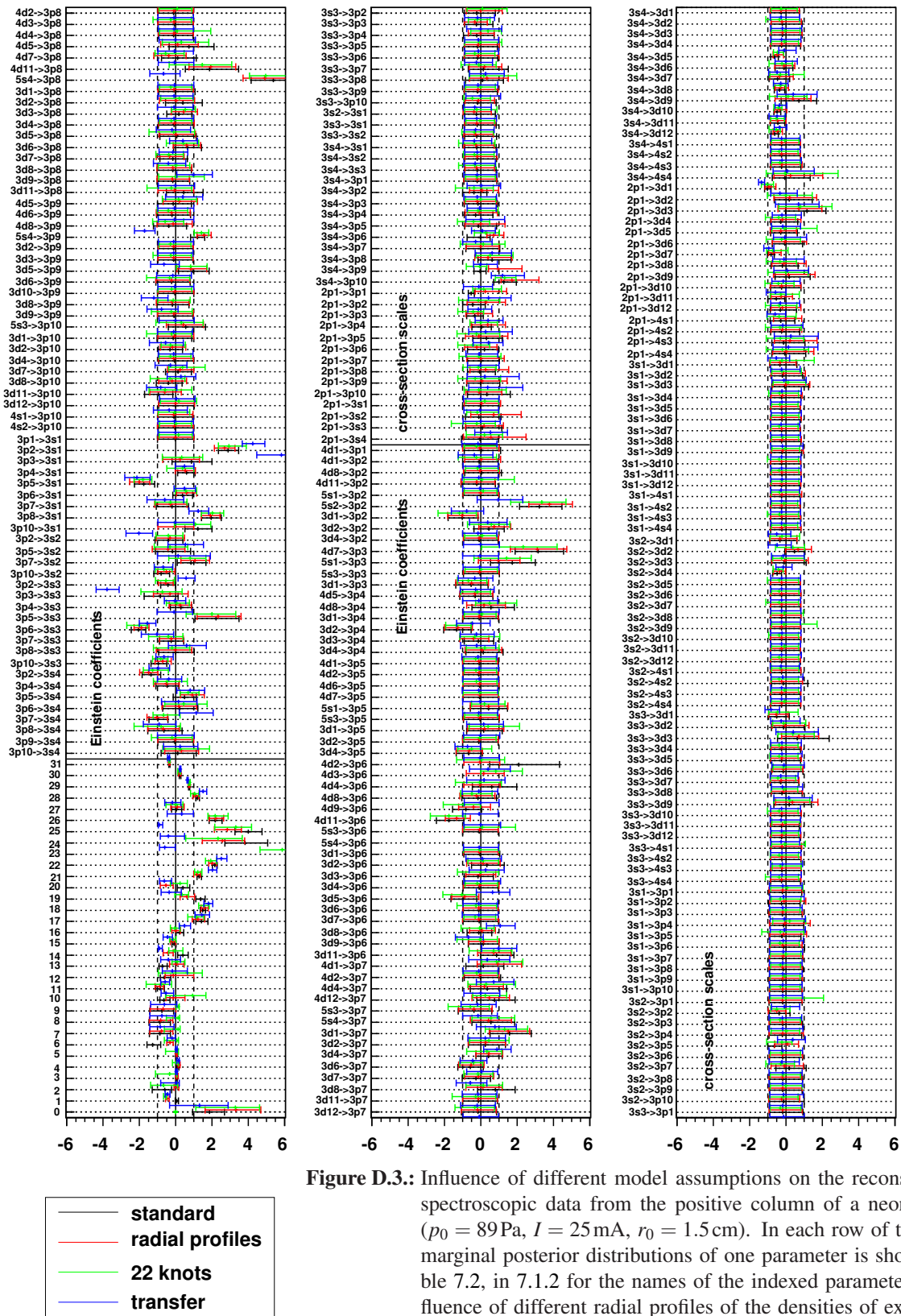
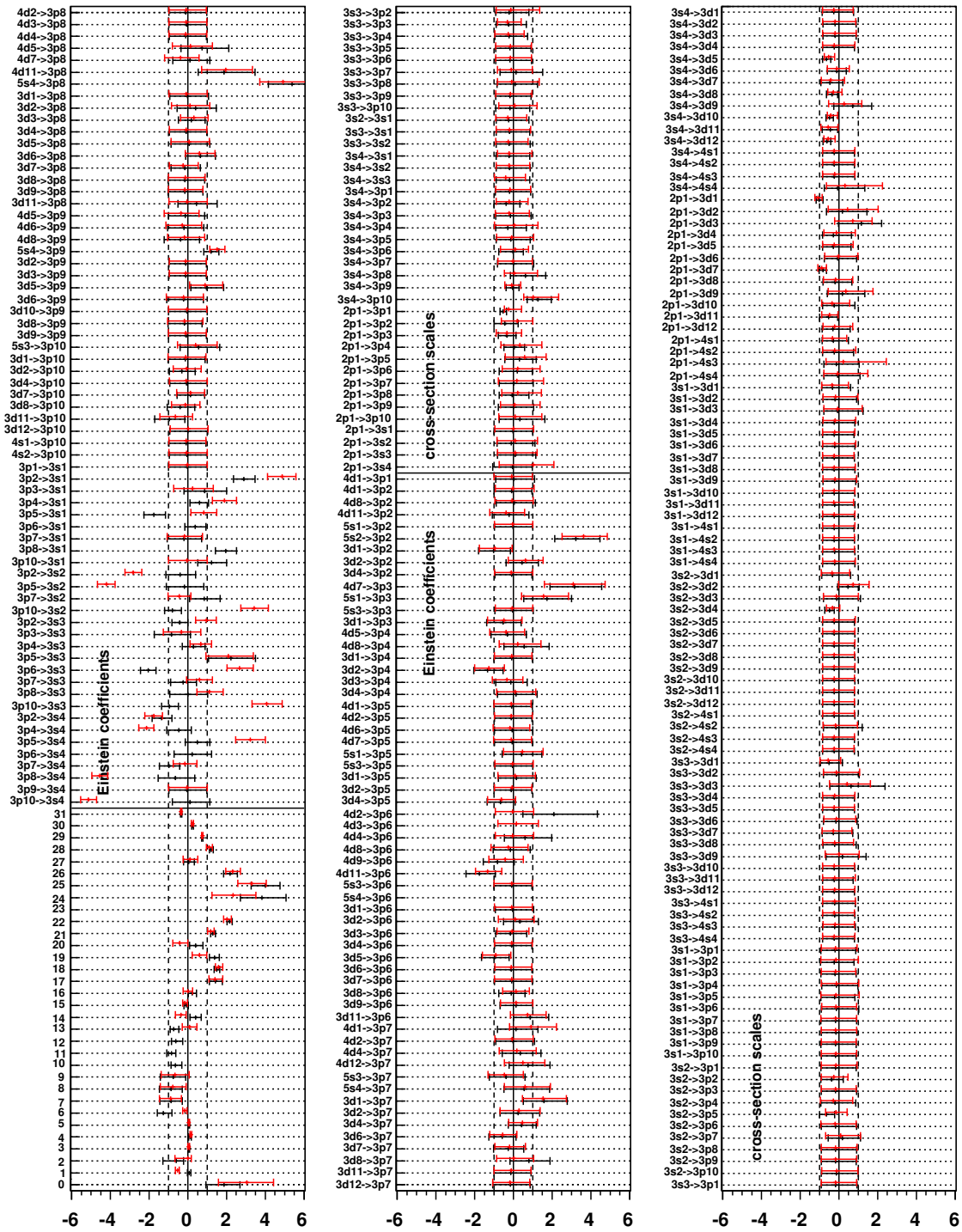


Figure D.3.: Influence of different model assumptions on the reconstruction of spectroscopic data from the positive column of a neon discharge ( $p_0 = 89\text{ Pa}$ ,  $I = 25\text{ mA}$ ,  $r_0 = 1.5\text{ cm}$ ). In each row of the plot, the marginal posterior distributions of one parameter is shown, see table 7.2, in 7.1.2 for the names of the indexed parameters. The influence of different radial profiles of the densities of excited states (red), the influence of a parameterization of the EEDF with a large number of spline knots (green) and the influence of a different apparatus function (blue) are compared to the standard configuration (black). See also 7.1.3 for more details of the used configurations.





— standard  
 — no 3s optical depth

Figure D.4.: Influence of different model assumptions on the reconstruction of spectroscopic data from the positive column of a neon discharge ( $p_0 = 89$  Pa,  $I = 25$  mA,  $r_0 = 1.5$  cm). See also caption of Fig. D.3 The influence of a model configuration without incorporation of the escape factors of transition with a final state in the 3s-multiplet (red) is compared to the standard configuration (black), See 7.1.3, for more details.

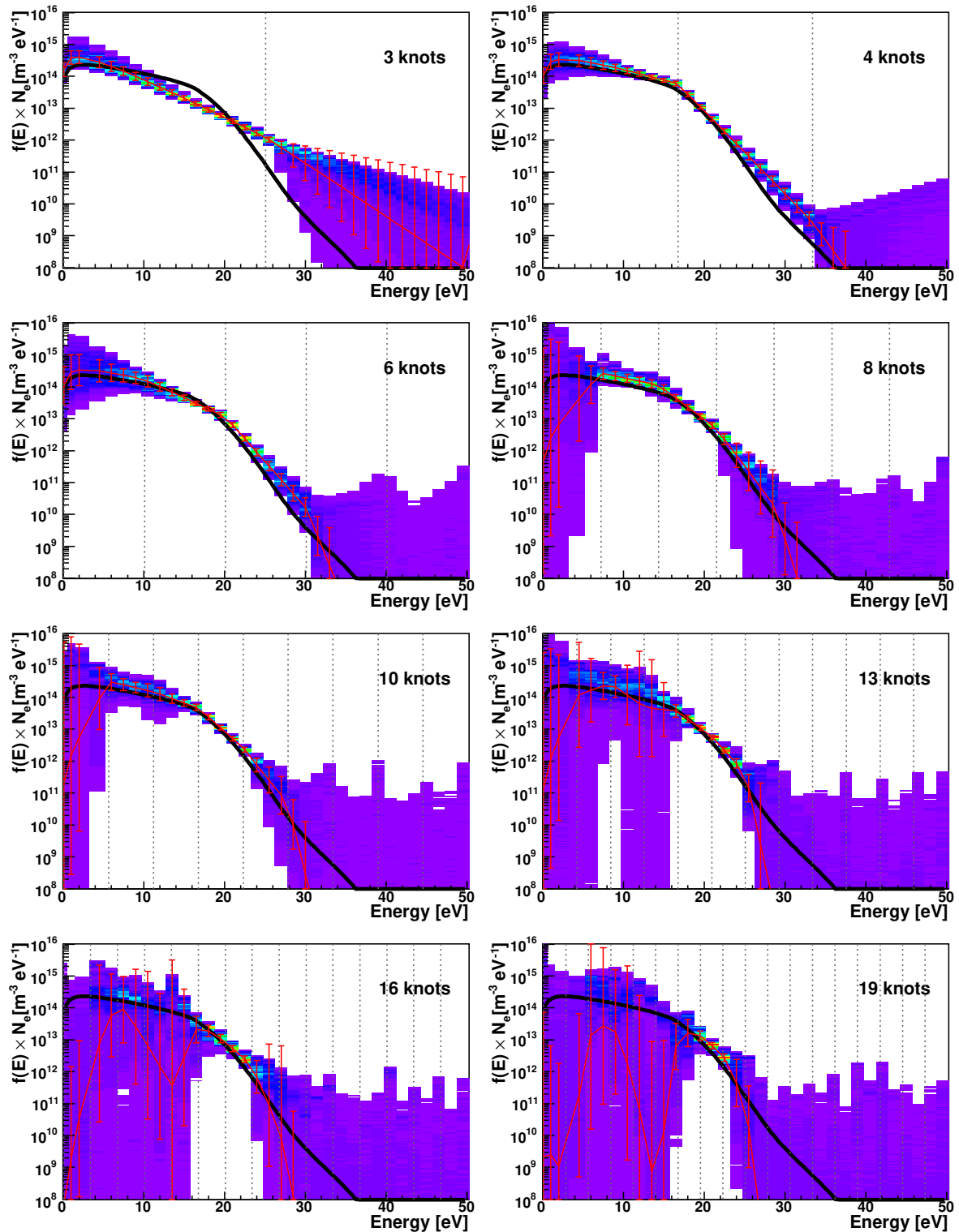


**Figure D.5.:** Reconstruction of the EEDF in the positive column of neon dc-discharge using different numbers of spline knots. The ordinates depict the number of electrons per energy interval per volume on a logarithmic scale. The black solid curves, showing the EEDF as obtained in independent kinetic modelling<sup>13</sup>, act as a reference. The red curve with error bars shows then expectation value and variance of the result of the reconstruction (cf. 7.1.2). The dotted vertical lines indicate the positions of the knots of the spline of the EEDF. The color coded histogram in the background shows the marginal probability distribution as obtained by the Monte-Carlo sampling. See also in 7.1.2 for more details of this representation of the result of the reconstruction.

## E. Labelling of Neon States

Index	Label	Paschen's notation	Configuration in $jK$	Configuration in $LS$	Energy [eV] (NIST)
0	2p <sub>1</sub>	1s <sub>1</sub>	2p <sup>6</sup> 1S <sub>0</sub>	2p <sup>6</sup> 1S <sub>0</sub>	0
1	3s <sub>4</sub>	1s <sub>5</sub>	2p <sup>5</sup> ( <sup>2</sup> P <sub>3/2</sub> <sup>o</sup> )3s 2 <sup>2</sup> [ $\frac{3}{2}$ ] <sup>o</sup> , $J = 2$	2p <sup>5</sup> 3s <sup>3</sup> P <sub>2</sub>	16.61907
2	3s <sub>3</sub>	1s <sub>4</sub>	2p <sup>5</sup> ( <sup>2</sup> P <sub>3/2</sub> <sup>o</sup> )3s 2 <sup>2</sup> [ $\frac{3}{2}$ ] <sup>o</sup> , $J = 1$	2p <sup>5</sup> 3s <sup>3</sup> P <sub>1</sub>	16.67083
3	3s <sub>2</sub>	1s <sub>3</sub>	2p <sup>5</sup> ( <sup>2</sup> P <sub>1/2</sub> <sup>o</sup> )3s 2 <sup>2</sup> [ $\frac{1}{2}$ ] <sup>o</sup> , $J = 0$	2p <sup>5</sup> 3s <sup>3</sup> P <sub>0</sub>	16.71538
4	3s <sub>1</sub>	1s <sub>2</sub>	2p <sup>5</sup> ( <sup>2</sup> P <sub>1/2</sub> <sup>o</sup> )3s 2 <sup>2</sup> [ $\frac{1}{2}$ ] <sup>o</sup> , $J = 1$	2p <sup>5</sup> 3s <sup>1</sup> P <sub>1</sub>	16.84805
5	3p <sub>10</sub>	2p <sub>10</sub>	2p <sup>5</sup> ( <sup>2</sup> P <sub>3/2</sub> <sup>o</sup> )3p 2 <sup>2</sup> [ $\frac{1}{2}$ ], $J = 1$	2p <sup>5</sup> 3p <sup>3</sup> S <sub>1</sub>	18.38162
6	3p <sub>9</sub>	2p <sub>9</sub>	2p <sup>5</sup> ( <sup>2</sup> P <sub>3/2</sub> <sup>o</sup> )3p 2 <sup>2</sup> [ $\frac{5}{2}$ ], $J = 3$	2p <sup>5</sup> 3p <sup>3</sup> D <sub>3</sub>	18.55511
7	3p <sub>8</sub>	2p <sub>8</sub>	2p <sup>5</sup> ( <sup>2</sup> P <sub>3/2</sub> <sup>o</sup> )3p 2 <sup>2</sup> [ $\frac{5}{2}$ ], $J = 2$	2p <sup>5</sup> 3p <sup>1</sup> D <sub>2</sub>	18.57583
8	3p <sub>7</sub>	2p <sub>7</sub>	2p <sup>5</sup> ( <sup>2</sup> P <sub>3/2</sub> <sup>o</sup> )3p 2 <sup>2</sup> [ $\frac{3}{2}$ ], $J = 1$	2p <sup>5</sup> 3p <sup>1</sup> P <sub>1</sub>	18.61270
9	3p <sub>6</sub>	2p <sub>6</sub>	2p <sup>5</sup> ( <sup>2</sup> P <sub>3/2</sub> <sup>o</sup> )3p 2 <sup>2</sup> [ $\frac{3}{2}$ ], $J = 2$	2p <sup>5</sup> 3p <sup>3</sup> P <sub>2</sub>	18.63679
10	3p <sub>5</sub>	2p <sub>5</sub>	2p <sup>5</sup> ( <sup>2</sup> P <sub>1/2</sub> <sup>o</sup> )3p 2 <sup>2</sup> [ $\frac{3}{2}$ ], $J = 1$	2p <sup>5</sup> 3p <sup>3</sup> D <sub>1</sub>	18.69336
11	3p <sub>4</sub>	2p <sub>4</sub>	2p <sup>5</sup> ( <sup>2</sup> P <sub>1/2</sub> <sup>o</sup> )3p 2 <sup>2</sup> [ $\frac{3}{2}$ ], $J = 2$	2p <sup>5</sup> 3p <sup>3</sup> D <sub>2</sub>	18.70407
12	3p <sub>3</sub>	2p <sub>3</sub>	2p <sup>5</sup> ( <sup>2</sup> P <sub>3/2</sub> <sup>o</sup> )3p 2 <sup>2</sup> [ $\frac{5}{2}$ ], $J = 0$	2p <sup>5</sup> 3p <sup>1</sup> S <sub>0</sub>	18.71138
13	3p <sub>2</sub>	2p <sub>2</sub>	2p <sup>5</sup> ( <sup>2</sup> P <sub>1/2</sub> <sup>o</sup> )3p 2 <sup>2</sup> [ $\frac{1}{2}$ ], $J = 1$	2p <sup>5</sup> 3p <sup>3</sup> P <sub>1</sub>	18.72638
14	3p <sub>1</sub>	2p <sub>1</sub>	2p <sup>5</sup> ( <sup>2</sup> P <sub>1/2</sub> <sup>o</sup> )3p 2 <sup>2</sup> [ $\frac{1}{2}$ ], $J = 0$	2p <sup>5</sup> 3p <sup>3</sup> P <sub>0</sub>	18.96595
15	4s <sub>4</sub>		2p <sup>5</sup> ( <sup>2</sup> P <sub>3/2</sub> <sup>o</sup> )4s 2 <sup>2</sup> [ $\frac{3}{2}$ ] <sup>o</sup> , $J = 2$	2p <sup>5</sup> 4s <sup>3</sup> P <sub>2</sub>	19.66403
16	4s <sub>3</sub>		2p <sup>5</sup> ( <sup>2</sup> P <sub>3/2</sub> <sup>o</sup> )4s 2 <sup>2</sup> [ $\frac{3}{2}$ ] <sup>o</sup> , $J = 1$	2p <sup>5</sup> 4s <sup>1</sup> P <sub>1</sub>	19.68819
17	4s <sub>2</sub>		2p <sup>5</sup> ( <sup>2</sup> P <sub>1/2</sub> <sup>o</sup> )4s 2 <sup>2</sup> [ $\frac{1}{2}$ ] <sup>o</sup> , $J = 0$	2p <sup>5</sup> 4s <sup>3</sup> P <sub>0</sub>	19.76060
18	4s <sub>1</sub>		2p <sup>5</sup> ( <sup>2</sup> P <sub>1/2</sub> <sup>o</sup> )4s 2 <sup>2</sup> [ $\frac{1}{2}$ ] <sup>o</sup> , $J = 1$	2p <sup>5</sup> 4s <sup>3</sup> P <sub>1</sub>	19.77978

E. Labelling of Neon States

Index	Label	Paschen's notation	Configuration in $jK$	Configuration in $LS$	Energy [eV] (NIST)
19	3d <sub>12</sub>		$2p^5(^2P_{3/2}^{\circ})3d^2[{}^1_{2}]^{\circ}, J = 0$	$2p^53d^3P_0$	20.02464
20	3d <sub>11</sub>		$2p^5(^2P_{3/2}^{\circ})3d^2[{}^1_{2}]^{\circ}, J = 1$	$2p^53d^3P_1$	20.02644
21	3d <sub>10</sub>		$2p^5(^2P_{3/2}^{\circ})3d^2[{}^7_{2}]^{\circ}, J = 4$	$2p^53d^3F_4$	20.03465
22	3d <sub>9</sub>		$2p^5(^2P_{3/2}^{\circ})3d^2[{}^7_{2}]^{\circ}, J = 3$	$2p^53d^1F_3$	20.03497
23	3d <sub>8</sub>		$2p^5(^2P_{3/2}^{\circ})3d^2[{}^3_{2}]^{\circ}, J = 2$	$2p^53d^3P_2$	20.03675
24	3d <sub>7</sub>		$2p^5(^2P_{3/2}^{\circ})3d^2[{}^3_{2}]^{\circ}, J = 1$	$2p^53d^3D_1$	20.04049
25	3d <sub>6</sub>		$2p^5(^2P_{3/2}^{\circ})3d^2[{}^5_{2}]^{\circ}, J = 2$	$2p^53d^1D_2$	20.04820
26	3d <sub>5</sub>		$2p^5(^2P_{3/2}^{\circ})3d^2[{}^5_{2}]^{\circ}, J = 3$	$2p^53d^3D_3$	20.04842
27	3d <sub>4</sub>		$2p^5(^2P_{1/2}^{\circ})3d^2[{}^5_{2}]^{\circ}, J = 2$	$2p^53d^3F_2$	20.13611
28	3d <sub>3</sub>		$2p^5(^2P_{1/2}^{\circ})3d^2[{}^5_{2}]^{\circ}, J = 3$	$2p^53d^3F_3$	20.13639
29	3d <sub>2</sub>		$2p^5(^2P_{1/2}^{\circ})3d^2[{}^3_{2}]^{\circ}, J = 2$	$2p^53d^3D_2$	20.13751
30	3d <sub>1</sub>		$2p^5(^2P_{1/2}^{\circ})3d^2[{}^3_{2}]^{\circ}, J = 1$	$2p^53d^1P_1$	20.13956
-	4p <sub>10</sub>		$2p^5(^2P_{3/2}^{\circ})4p^2[{}^1_{2}]^{\circ}, J = 1$		20.14965
-	4p <sub>9</sub>		$2p^5(^2P_{3/2}^{\circ})4p^2[{}^5_{2}]^{\circ}, J = 3$		20.18843
-	4p <sub>8</sub>		$2p^5(^2P_{3/2}^{\circ})4p^2[{}^5_{2}]^{\circ}, J = 2$		20.19692
-	4p <sub>7</sub>		$2p^5(^2P_{3/2}^{\circ})4p^2[{}^3_{2}]^{\circ}, J = 1$		20.21099
-	4p <sub>6</sub>		$2p^5(^2P_{3/2}^{\circ})4p^2[{}^3_{2}]^{\circ}, J = 2$		20.21418
-	4p <sub>5</sub>		$2p^5(^2P_{3/2}^{\circ})4p^2[{}^1_{2}]^{\circ}, J = 0$		20.25918
-	4p <sub>4</sub>		$2p^5(^2P_{1/2}^{\circ})4p^2[{}^3_{2}]^{\circ}, J = 1$		20.29091
-	4p <sub>3</sub>		$2p^5(^2P_{1/2}^{\circ})4p^2[{}^1_{2}]^{\circ}, J = 1$		20.29717
-	4p <sub>2</sub>		$2p^5(^2P_{1/2}^{\circ})4p^2[{}^3_{2}]^{\circ}, J = 2$		20.29728
-	4p <sub>1</sub>		$2p^5(^2P_{1/2}^{\circ})4p^2[{}^1_{2}]^{\circ}, J = 0$		20.36885
-	5s <sub>4</sub>		$2p^5(^2P_{3/2}^{\circ})5s^2[{}^3_{2}]^{\circ}, J = 2$		20.56007
-	5s <sub>3</sub>		$2p^5(^2P_{3/2}^{\circ})5s^2[{}^3_{2}]^{\circ}, J = 1$		20.57056
-	5s <sub>2</sub>		$2p^5(^2P_{1/2}^{\circ})5s^2[{}^1_{2}]^{\circ}, J = 0$		20.65655
-	5s <sub>1</sub>		$2p^5(^2P_{1/2}^{\circ})5s^2[{}^1_{2}]^{\circ}, J = 1$		20.66277
-	4d <sub>12</sub>		$2p^5(^2P_{3/2}^{\circ})4d^2[{}^1_{2}]^{\circ}, J = 0$		20.70135
-	4d <sub>11</sub>		$2p^5(^2P_{3/2}^{\circ})4d^2[{}^1_{2}]^{\circ}, J = 1$		20.70230
-	4d <sub>10</sub>		$2p^5(^2P_{3/2}^{\circ})4d^2[{}^7_{2}]^{\circ}, J = 4$		20.70536
-	4d <sub>9</sub>		$2p^5(^2P_{3/2}^{\circ})4d^2[{}^7_{2}]^{\circ}, J = 3$		20.70550
-	4d <sub>8</sub>		$2p^5(^2P_{3/2}^{\circ})4d^2[{}^3_{2}]^{\circ}, J = 2$		20.70679
-	4d <sub>7</sub>		$2p^5(^2P_{3/2}^{\circ})4d^2[{}^3_{2}]^{\circ}, J = 1$		20.70871
-	4d <sub>6</sub>		$2p^5(^2P_{3/2}^{\circ})4d^2[{}^5_{2}]^{\circ}, J = 2$		20.71126
-	4d <sub>5</sub>		$2p^5(^2P_{3/2}^{\circ})4d^2[{}^5_{2}]^{\circ}, J = 3$		20.71139
-			(...)		
-	4d <sub>4</sub>		$2p^5(^2P_{1/2}^{\circ})4d^2[{}^5_{2}]^{\circ}, J = 2$		20.80392
-	4d <sub>3</sub>		$2p^5(^2P_{1/2}^{\circ})4d^2[{}^5_{2}]^{\circ}, J = 3$		20.80404
-	4d <sub>2</sub>		$2p^5(^2P_{1/2}^{\circ})4d^2[{}^3_{2}]^{\circ}, J = 2$		20.80417
-	4d <sub>1</sub>		$2p^5(^2P_{1/2}^{\circ})4d^2[{}^3_{2}]^{\circ}, J = 1$		20.80551

## Bibliography

- [1] R. Fischer, A. Dinklage, and E. Pasch, Bayesian modelling of fusion diagnostics, *Plasma Phys. Contr. Fusion* **45**(7), 1095–1111 (2003).
- [2] A. Dinklage, R. Fischer, and J. Svensson, Topics and methods for data validation by means of Bayesian probability theory, *Fusion Science and Technology* **46**(2), 355–364 (2004).
- [3] N. Brenning, An appendix to the paper 'Te determination in low-density plasmas from the He I 3889 Å and 5016 Å line intensities', *Journal of Physics D: Applied Physics* **15**(1), L1–L2 (1982).
- [4] B. Schweer, Electron-Temperature and Electron-Density Profiles Measured with a Thermal He-Beam in the Plasma Boundary of Textor, *Journal of nuclear materials* **196**, 174–178 (1992).
- [5] R. Fischer and V. Dose, Electron energy distribution reconstruction in low-pressure helium plasmas from optical measurements, *Plasma Phys. Contr. Fusion* **41**(9), 1109–1123 (1999).
- [6] S. Pfau, A. Rutscher, and K. Wojacek, Das Ähnlichkeitsgesetz für quasineutrale, anisotherme Entladungssäulen, *Beitr. Plasmaphysik* **9**(4) (1969).
- [7] S. Pfau, J. Rohmann, D. Uhrlandt, and R. Winkler, Experimental and Theoretical Study of the Inhomogeneous Electron Kinetics in the dc Column Plasma, *Contrib. Plasma Phys.* **36**(4), 449–469 (1996).
- [8] I. A. Porokhova, Y. B. Golubovskii, C. Wilke, and A. Dinklage, Electron Distribution Function in the Anode Region of Inert Gas Discharges at Low Pressures and Currents, *J. Phys. D: Appl. Phys.* **32**(23), 3025–3031 (1999).
- [9] D. Uhrlandt, M. Schmidt, J. F. Behnke, and T. Bindemann, Self-consistent Description of the dc Column Plasma Including Wall Interaction, *J. Phys. D: Appl. Phys.* **33**(19), 2475–2482 (2000).
- [10] S. Franke, H. Deutsch, A. Dinklage, S. Solyman, and C. Wilke, Power Loss by Resonance Radiation From a dc Neon Glow Discharge at Low Pressures and Low Currents, *J. Phys. D: Appl. Phys.* **34**(3), 340–346 (2001).
- [11] M. Otte, *Experimentelle Untersuchungen der Elektronenkinetik schwach ionisierter stoßbestimmter Plasmen unter räumlich inhomogenen Bedingungen*, PhD thesis, Ernst-Moritz-Arndt-Universität, Greifswald, 2000.
- [12] A. Dinklage, S. Franke, S. Solyman, H. Deutsch, H. Scheibner, and C. Wilke, 74 nm Radiative Efficiency of a DC Neon Glow Discharge, *Contrib. Plasma Phys.* **40**(1-2), 96–100 (2000).
- [13] D. Uhrlandt and S. Franke, Study of a Neon dc Column Plasma by a Hybrid Method, *J. Phys. D: Appl. Phys.* **35**(7), 680–688 (2002).

- [14] D. Loffhagen, F. Sigeneger, and R. Winkler, Study of the electron kinetics in the anode region of a glow discharge by a multiterm approach and Monte Carlo simulations, *J. Phys. D: Appl. Phys.* **35**(14), 1768–1776 (2002).
- [15] F. F. Chen, *Introduction to Plasma Physics*, Plenum Press, New York, 1988.
- [16] K. Wieseemann, *Einführung in die Gaselektronik*, Teubner, Stuttgart, 1976.
- [17] Y. P. Raizer, *Gas Discharge Physics*, Springer-Verlag Berlin Heidelberg, 1991.
- [18] L. Tonks and I. Langmuir, Oscillations in Ionized Gases, *Phys. Rev.* **33**(2), 195–210 (Feb 1929).
- [19] S. Ichimaru, *Statistical Plasma Physics*, Frontiers in Physics, Westview Press, Boulder, Colorado, 2004.
- [20] S. Weinberg, *The Discovery of Subatomic Particles*, Cambridge: At the University Press, Cambridge, 2003.
- [21] R. Schneider and R. Kleiber, Computational Plasma Physics, in *Plasma Physics: Confinement, Transport and Collective Effects*, edited by A. Dinklage, T. Klinger, G. Marx, and L. Schweikhard, volume 670 of *Lecture Notes in Physics*, Springer-Verlag Berlin Heidelberg, 2005.
- [22] U. Schumacher, Basics of Plasma Physics, in *Plasma Physics: Confinement, Transport and Collective Effects*, edited by A. Dinklage, T. Klinger, G. Marx, and L. Schweikhard, volume 670 of *Lecture Notes in Physics*, Springer-Verlag Berlin Heidelberg, 2005.
- [23] H. Bernstein, Maxwell, J. Clerk on the History of the Kinetic-Theory of Gases, 1871, *Isis* **54**(176), 206–216 (1963).
- [24] R. Balescu, *Statistical Dynamics: Matter Out of Equilibrium*, Imperial College Press, London, 1997.
- [25] O. W. Richardson, *The Electron Theory of Matter*, Cambridge: At the University Press, Cambridge, 1914.
- [26] I. Langmuir and K. T. Compton, Electrical Discharges in Gases Part I. Survey of Fundamental Processes, *Rev. Mod. Phys.* **2**(2), 123–242 (Apr 1930).
- [27] A. Vlasov, The Vibrational Properties of the Electron Gas, *Zh. Eksp. Teor. Fiz.* **8**, 291 (1938).
- [28] L. D. Landau, Kinetic equation for the Coulomb effect, *Phys. Z. Sowjetunion* **10**, 154 (1936).
- [29] R. Balescu, Irreversible Processes in Ionized Gases, *Physics of Fluids* **3**(1), 52–63 (1960).
- [30] P. Debye and E. Hückel, The theory of electrolytes I. The lowering of the freezing point and related occurrences, *Physikalische Zeitschrift* **24**, 185–206 (1923).
- [31] A. Rutscher, *Beiträge zur positiven Säule der Niederdruckglimmentladung*, Ernst-Moritz-Arndt-Universität Greifswald, 1964, habilitation thesis.
- [32] H.-J. Kunze, Plasma Diagnostics, in *Plasma Physics: Confinement, Transport and Collective Effects*, edited by A. Dinklage, T. Klinger, G. Marx, and L. Schweikhard, volume 670 of *Lecture Notes in Physics*, Springer-Verlag Berlin Heidelberg, 2005.

- 
- [33] A. F. Molisch and B. P. Oehry, *Radiation Trapping in Atomic Vapours*, Oxford University Press, Oxford, 1998.
- [34] J. E. Lawler and J. J. Curry, Analytical formula for radiation trapping with partial frequency redistribution, *J. Phys. D: Appl. Phys.* **31**(22), 3235–3242 (1998).
- [35] D. Uhrlandt and R. Winkler, Radial structure of the kinetics and production of electrons in the dc column plasma, *Plasma Chem. Plasma Process.* **16**(4), 517–545 (1996).
- [36] V. I. Kolobov and V. A. Godyak, Nonlocal Electron Kinetics in Collisional-Gas Discharge Plasma, *IEEE Trans. Plasma Sci.* **23**(4), 503–531 (Aug 1995).
- [37] K. Bartschat, Electron Scattering by Atoms, Ions and Molecules, *Encyclopedia of Applied Physics* (2008), to be published.
- [38] O. Zatsarinny and K. Bartschat, Relativistic B-spline R-matrix method for electron collisions with atoms and ions: Application to low-energy electron scattering from Cs, *Phys. Rev. A* **77**(6) (2008).
- [39] J. J. Sakurai, *Modern Quantum Mechanics*, Addison-Wesley, 1994.
- [40] Y.-K. Kim, Scaling of plane-wave Born cross sections for electron-impact excitation of neutral atoms, *Phys. Rev. A* **64**(3), 032713 (Aug 2001).
- [41] I. Bray and A. T. Stelbovics, Convergent-close-coupling calculations of electron-hydrogen scattering, *Phys. Rev. A* **46**(11), 6995–7011 (1992).
- [42] K. Bartschat, E. T. Hudson, M. P. Scott, P. G. Burke, and V. M. Burke, Convergent  $R$  matrix with pseudostates calculation for  $e^-$ -He collisions, *Phys. Rev. A* **54**(2), R998 (Aug 1996).
- [43] O. Zatsarinny, BSR: B-spline atomic R-matrix codes, *Computer physics communications* **174**(4), 273–356 (2006).
- [44] C. P. Ballance and D. C. Griffin, Electron-Impact Excitation of Neon: a Pseudo-State Convergence Study, *Journal of Physics B: Atomic, Molecular and Optical Physics* **37**(14), 2943–2957 (2004).
- [45] A. Messiah, *Quantenmechanik*, volume 2, de Gruyter, 1985.
- [46] Y. Ralchenko, A. E. Kramida, J. Reader, and NIST ASD Team, NIST Atomic Spectra Database (version 3.1.5), published online <http://physics.nist.gov/asd3>, National Institute of Standards and Technology (NIST), Gaithersburg, MD, USA, 2008.
- [47] O. Zatsarinny and K. Bartschat, B-spline Breit-Pauli R-matrix calculations for electron collisions with neon atoms, *J. Phys. B* **37**(10), 2173–2189 (2004).
- [48] E. T. Jaynes, *Probability Theory: the Logic of Science*, Cambridge University Press, Cambridge, 2005.
- [49] P. Gregory, *Bayesian Logical Data Analysis for the Physical Sciences*, Cambridge University Press, Cambridge, 2005.
- [50] D. Sivia and J. Skilling, *Data Analysis: A Bayesian Tutorial Second Edition*, Oxford University Press, Oxford, 2006.

- [51] W.-M. Yao et al., Review of Particle Physics, *Journal of physics* **33**(1), 1–1232 (2006).
- [52] C. E. Shannon, A Mathematical Theory of Communication, *The Bell System Technical Journal* **27**, 379–423 (1948).
- [53] E. T. Jaynes, Prior Probabilities, *IEEE Transactions On Systems Science and Cybernetics* **sec-4**(3), 227–241 (1968).
- [54] H. Jeffreys, An Invariant Form for the Prior Probability in Estimation Problems, *Proceedings of the Royal Society of London. Series A, Mathematical and Physical Sciences* **186**(1007), 453–461 (1946).
- [55] G. J. Erickson and Y. Zhai, editors, *Entropic Priors*, volume 707, AIP, 2004.
- [56] K. H. Knuth, A. Caticha, J. L. Center, A. Giffin, and C. C. Rodríguez, editors, *Updating Probabilities with Data and Moments*, volume 954, AIP, 2007.
- [57] K. H. Knuth, A. Caticha, J. L. Center, A. Giffin, and C. C. Rodríguez, editors, *Foundations*, volume 954, AIP, 2007.
- [58] N. Metropolis, The Beginning of the Monte Carlo Method, *Los Alamos Science* **15**, 125–130 (1987).
- [59] D. J. C. MacKay, Introduction to Monte Carlo Methods, in *Learning in Graphical Models*, edited by M. I. Jordan, NATO Science Series, pages 175–204, Kluwer Academic Press, 1998.
- [60] W. Gilks, S. Richardson, and D. Spiegelhalter, editors, *Markov Chain Monte Carlo in Practice*, Chapman & Hall/CRC, 1995.
- [61] A. Gelman, J. B. Carlin, H. S. Stern, and D. B. Rubin, *Bayesian data analysis*, Texts in statistical science, Chapman & Hall/CRC, Boca Raton, Fla., 1995.
- [62] R. M. Neal, Probabilistic inference using Markov chain Monte Carlo methods, Technical Report CRG-TR-93-1, Dept. of Computer Science, Univ. of Toronto, 1993.
- [63] H. L. Anderson, Metropolis, Monte Carlo and the MANIAC, *Los Alamos Science* **14**, 96–108 (1986).
- [64] N. Metropolis, A. W. Rosenbluth, M. N. Rosenbluth, A. H. Teller, and E. Teller, Equation of State Calculations by Fast Computing Machines, *The Journal of Chemical Physics* **21**(6), 1087–1092 (1953).
- [65] W. K. Hastings, Monte Carlo sampling methods using Markov chains and their applications, *Biometrika* **57**(1), 97–109 (1970).
- [66] M. K. Cowles and B. P. Carlin, Markov Chain Monte Carlo Convergence Diagnostics: A Comparative Review, *Journal of the American Statistical Association* **91**, 883–904 (1996).
- [67] G. O. Roberts and J. S. Rosenthal, General State Space Markov Chains and MCMC Algorithms, *Probab. Surveys* **1**, 20–71 (2004).
- [68] Ocean Optics, Spectroscopy Equipment, <http://www.oceanoptics.com>.
- [69] D. F. Gray, *The Observation and Analysis of Stellar Photospheres, Second edition*, Cambridge University Press, Bristol, 1992.



- 
- [70] L. W. G. Steenhuijsen, Investigations on Afterglows of Neon Gas Discharges, *Beiträge aus der Plasmaphysik* **21**(5), 301–328 (1981).
- [71] R. C. Wetzel, F. A. Baiocchi, T. R. Hayes, and R. S. Freund, Absolute cross sections for electron-impact ionization of the rare-gas atoms by the fast-neutral-beam method, *Phys. Rev. A* **35**(2), 559–577 (Jan 1987).
- [72] L. Vriens and A. H. M. Smeets, Cross-section and rate formulas for electron-impact ionization, excitation, deexcitation, and total depopulation of excited atoms, *Phys. Rev. A* **22**(3), 940–951 (Sep 1980).
- [73] P. Jonas, B. Bruhn, B.-P. Koch, and A. Dinklage, Numerical investigations on strong pattern selecting Eckhaus instabilities in neon glow discharges, *Physics of Plasmas* **7**(2), 729–739 (2000).
- [74] W. H. Press, S. A. Teukolsky, W. T. Vetterling, and B. P. Flannery, *Numerical Recipes in C++: The Art of Scientific Computing*, Cambridge University Press, Cambridge, February 2002.
- [75] R. Brun, F. Rademakers, P. Canal, V. Fine, and S. Panacek, ROOT an Object Oriented Data Analysis Framework, published online <http://root.cern.ch>, centre européen pour la recherche nucléaire (CERN), Geneva, Switzerland, 1995.
- [76] V. Dose, R. Fischer, and W. von der Linden, Deconvolution Based on Experimentally Determined Apparatus Functions, in *MAXIMUM ENTROPY AND BAYESIAN METHODS*, edited by Erickson, GJ and Rychert, JT and Smith, CR, volume 98 of *FUNDAMENTAL THEORIES OF PHYSICS*, pages 147–152, 1998, 17th International Workshop on Maximum Entropy and Bayesian Methods of Statistical Analysis, BOISE, ID, AUG 04-08, 1997.
- [77] M. Allan, K. Franz, H. Hotop, O. Zatsarinny, and K. Bartschat, Absolute angle - Differential cross sections for excitation of neon atoms by electrons of energy 16.6-19.2 eV, in *Photonic, Electronic and Atomic Collisions*, edited by Fainstein, PD and Lima, MAP and Miraglia, JE and Montenegro, EC and Rivarola, RD, pages 261–264, 2006, 24th International Conference on Photonic, Electronic and Atomic Collisions, Rosario, ARGENTINA, JUL 20-26, 2005.
- [78] S. K. Crow EL, *Log-normal Distributions: Theory and Application*, Dekker, New York, 1988.
- [79] J. Chilton, J. Stewart, M.D., and C. Lin, Electron-impact excitation cross sections of neon, *J. Phys. A* **61**(5), 052708/1–12 (2000).
- [80] K. A. Berrington, W. B. Eissner, and P. Norrington, RMATRIX1 - Belfast Atomic R-Matrix Codes, *Copmputer Physics Communications* **92**(2-3), 290–420 (1995).
- [81] S. Franke, Bilanzgleichungen zur Modellierung der Dynamik einer Neon-Glimmentladung, Master's thesis, Ernst-Moritz-Arndt-Universität, Greifswald, 1996.
- [82] D. Dodt, A. Dinklage, R. Fischer, K. Bartschat, O. Zatsarinny, and D. Loffhagen, Reconstruction of an electron energy distribution function using integrated data analysis, *J. Phys. D: Appl. Phys.* **41**(20), 205207 (2008).
- [83] M. Krychowiak, D. Dodt, H. Dreier, R. König, and R. Wolf, Development of a virtual  $Z_{\text{eff}}$  diagnostic for the W7-X stellarator, *Rev. Sci. Instrum.* **79**(10), 10F512 (2008).

- [84] D. Dodt, A. Dinklage, R. Fischer, and D. Loffhagen, Analysis of Optical Emission Spectroscopy on Discharges, *AIP Conference Proceedings* **872**(1), 264–271 (2006).
- [85] D. Dodt, A. Dinklage, R. Fischer, K. Bartschat, and O. Zatsarinny, Integrated Data Analysis of Spectroscopic Data, *NIFS Proceedings* **69**, 841 (2007).
- [86] D. Dodt, A. Dinklage, R. Fischer, K. Bartschat, and O. Zatsarinny, Form-Free Reconstruction of an Electron Energy Distribution Function from Optical Emission Spectroscopy, *AIP Conference Proceedings* **993**(1), 203–210 (2008).
- [87] D. Dodt, A. Dinklage, R. Fischer, K. Bartschat, and O. Zatsarinny, Form-Free Reconstruction of an Electron Energy Distribution Function from Optical Emission Spectroscopy, *AIP Conference Proceedings* **993**(1), 203–210 (2008).

## F. Curriculum Vitae

### Persönliche Angaben

Name: Dirk Dodt  
Geboren: am 2.3.1979 in Iserlohn  
Eltern: Gertrud Teworte und Helmut Dodt  
Anschrift: Franz-Mehring-Str 22, 17489 Greifswald  
Email: ddodt@ipp.mpg.de

### Berufserfahrung und Praktika

08.2005 - 01.2009 Promotion am Max-Planck-Institut für Plasma Physics, Greifswald, Thema "Reconstruction of Electron Energy Distribution Functions from Emission Spectroscopic Data"

10.2003 - 12.2004 Studentische Hilfskraft bei der Universität Dortmund, (Lehraufgaben während der Diplomarbeit: Betreuung von Übungen und experimenteller Praktika)

06.2003 - 08.2003 Teilnahme am Sommerstudentenprogramm des "Centre Européen pour la Recherche Nucleaire" (CERN), Genf

07.2002 - 09.2002 Teilnahme am Sommerstudentenprogramm des "Deutschen Elektronen Synchrotron" (DESY), Hamburg

08.1998 - 09.1999 Zivildienst bei der "evangelischen Jugendhilfe", Iserlohn

### Ausbildung

10.2003 - 04.2005 Diplomarbeit, am "Deutschen Elektronen Synchrotron" (DESY), Hamburg über das Thema "Analysis of the Data Quality of the FTT"

10.1999 - 04.2005 Studium der Physik an der Universität Dortmund, Abschluss: Diplom Physiker

08.1989 - 06.1998 Besuch der Schule "Gymnasium an der Stenner", Iserlohn, Abschluss: Fachhochschulreife

08.1985 - 06.1989 Besuch der Grundschule am Wiesengrund, Iserlohn



## G. Publication List

A current version of this list can be found at <http://www.ipp.mpg.de/~ddodt>.

### Papers in Refereed Journals

- Dirk Dodt, Andreas Dinklage, Rainer Fischer, Klaus Bartschat, Oleg Zatsarinny, and Detlef Loffhagen *Reconstruction of an Electron Energy Distribution Function Using Integrated Data Analysis*  
J. Phys. D: Appl. Phys. **41** 205207 (2008)
- Maciej Krychowiak, Dirk Dodt, Heiko Dreier, Ralf König, and Robert Wolf *Development of a virtual Zeff diagnostic for the W7-X stellarator*  
Rev. Sci. Instrum. **79**, 10F512 (2008)

### Peer Reviewed Contributions to International Conferences

- PLASMA 2007 Greifswald, Germany  
Dirk Dodt, Andreas Dinklage, Rainer Fischer, Klaus Bartschat, and Oleg Zatsarinny *Form-Free Reconstruction of an Electron Energy Distribution Function from Optical Emission Spectroscopy*  
AIP Conference Proceedings Volume **993**, pp. 203 (2008)
- MaxEnt 2007, Albany, USA  
Dirk Dodt, Andreas Dinklage, Rainer Fischer, and Roland Preuss *Assessment of Electron Energy Distributions in Discharges by Optical Emission Spectroscopy*  
AIP Conference Proceedings **954**, pp. 468 (2007)
- MaxEnt 2006, Paris, France  
Dirk Dodt, Andreas Dinklage, Rainer Fischer, and Detlef Loffhagen *Analysis of Optical Emission Spectroscopy on Discharges*  
AIP Conference Proceedings **872**, pp. 264-271 (2006)

### Contributions to International Conferences

- MaxEnt 2008, São Sebastião, São Paulo, Brasil:  
Dirk Dodt, Andreas Dinklage, Rainer Fischer, Klaus Bartschat, and Oleg Zatsarinny *Influence of Uncertain Atomic Data on The Reconstruction of EEDFs From Optical Emission Spectroscopy* (Talk)
- 5th Workshop on Fusion Data Processing, Analysis and Validation, Culham, UK  
Dirk Dodt, Andreas Dinklage, Rainer Fischer, Klaus Bartschat, and Oleg Zatsarinny *Reconstruction of Electron Energy Distribution Functions from Optical Emission Spectroscopy* (Talk)

- Jung, A. W., Baird, A., Baldinger, R., Baumgartner, S., Beneckenstein, D., Berger, N., Boenig, M. -O., Caminada, L., Dodt, D., Elsen, E., Kolander, M., Kolya, S., Krueger, K., Lohwasser, K., Meer, D., Mercer, D., Michels, V., Mueller, D., Mueller, J., Naumann, J., Newman, P. R., Sankey, D., Sauter, M., Schning, A., Schultz-Coulon, H. -C., Wessels, M., Wissing, Ch., Yan, W. *First Results from the Third Level of the H1 Fast Track Trigger* Real Time Conference, 2007. **15th** IEEE-NPSS, 676-682 (2007)
- ITC-18, Toki, Japan  
Dirk Dodt, Andreas Dinkluge, Rainer Fischer, Klaus Bartschat, and Oleg Zatsarinny *Integrated Data Analysis of Spectroscopic Data* NIFS Proc. **69**, pp. 841 (2007)
- Wissing, C. Baird, A. Baldinger, R. Baumgartner, S. Berger, N. Boenig, M.-O. Brown, D. Dodt, D. Fleming, Y.H. Jung, A.W. Kleinwort, C. Kolander, M. Kolya, S. Krueger, K. Meer, D. Mercer, D. Michels, V. Muller, D. Muller, J. Naumann, J. Newman, P.R. Sankey, D.P.C. Schoning, A. Schultz-Coulon, H.-C. Weber, R. Wenbiao Yan Wessels, M. *Performance of the H1 fast track trigger - operation and commissioning results* Real Time Conference, 2005. **14th** IEEE-NPSS, pp. 4 (2005)
- Berger, N. Baird, A. Baldinger, R. Baumgartner, S. Boenig, M.-O. Brown, D.P. Dodt, D. Fleming, Y.H. Jung, A.W. Kolander, M. Kolya, S. Krueger, K. Meer, D. Mercer, D. Muller, D. Muller, J. Naumann, J. Newman, P.R. Sankey, D.P.C. Schoning, A. Schultz-Coulon, H.-C. Weber, R. Wissing, C. Yan, W. *First results from the first level of the H1 fast track trigger* 2004 IEEE Nuclear Science Symposium Conference Record (IEEE Cat. No. 04CH37604), Volume **3**, 1976-9 (2004)

### Contributions to the Spring Meeting of the “Deutschen Physikalischen Gesellschaft”

- DPG Frühjahrstagung 2008, Darmstadt, Deutschland  
Dirk Dodt, Andreas Dinkluge, Rainer Fischer, Klaus Bartschat, and Oleg Zatsarinny *Rekonstruktion von Elektronenenergieverteilungsfunktionen aus emissionsspektroskopischen Daten* (Talk)
- DPG Frühjahrstagung 2007, Duesseldorf, Deutschland  
Dirk Dodt, and Andreas Dinkluge *Rekonstruktion von Elektronen-Energie-Verteilungen aus emissionspektroskopischen Daten* (Poster)
- DPG Frühjahrstagung 2006, Augsburg, Deutschland  
Dirk Dodt, Andreas Dinkluge, and Rainer Fischer *Assessment of Emission Spectroscopy for the Reconstruction of the Electron Temperature* (Poster)
- DPG Frühjahrstagung 2005, Berlin, Deutschland  
Dirk Dodt, Christoph Wissing, Kleinwort, C., Schoning, A. *Kalibration der Eingangsdaten des schnellen Spurtriggers von H1*

# Danksagung

Zuallererst möchte ich mich bei meiner lieben Mutter danken, die das Stipendium die ersten 25 1/2 Jahre bezahlt hat, und meiner ganzen Familie, meinen Brüdern Jens und Jörn, und Maria, die immer da sind, wenn es darauf ankommt, oder auch, wenn es etwas zu bejammern oder zum prahlen gibt.

Meinem Chef, Andreas Dinklage, möchte ich für die Gelegenheit danken, mit dieser Doktorarbeit den Einstieg in die Fusionsforschung und schwarze Magie der Bayesschen Zahlendreherei zu finden und für seine Unterstützung, auf die man sich verlassen konnte und die auch ihren Teil dazu beigetragen hat, dass der Ball im Tor landet.

Mein Dank gilt Holger Testrich, Robert Mrotzek und Herrn Rudolph für die Hilfe beim präparieren der Entladungsröhren und Ralf König und Maciej für die Hilfe beim Einstieg in die Welt der optischen Spektroskopie. Dank auch an Ekkehard Pasch, der mit seinem guten Draht zur Elektrowerkstatt und viel Rennerei die defekte Standardlichtquelle für das gute Gefühl im Zweifel noch messen zu können repariert hat. Bedanken möchte ich mich auch bei den Koautoren des Papiers für ihre schnellen und konkreten Verbesserungsvorschläge, insbesondere Klaus Bartschat, für die fruchtbare Zusammenarbeit und die objektive Einschätzung der Unsicherheiten seiner Rechnungen. Roland Preuss danke ich für für meinen ersten Markov-Chain Monte-Carlo Algorithmus. Rainer Fischer gilt mein Dank für das Teilen seines Erfahrungsschatzes in der Bayesschen Datenanalyse und die immer konstruktive Kritik auch in Detailfragen. Udo von Toussaint verdient meinen Dank für interessante Anregungen und unkomplizierte Hilfe zum Thema Rechenleistung. Volker Dose danke ich für inspirierende Diskussionen und die Berechnung eines analytischen Schätzers. Aus der Vorabversion des Plasmaspektroskopie Skriptes von Herrn Professor Kunze konnte ich hilfreiche Ideen ziehen, vielen Dank. Mein großer Dank gilt auch den beiden guten Seelen des Bereichs, Maria und Anja, ich glaube ich werde nie wieder so unbesorgt umsorgt auf Dienstreisen gehen.

Das Büroklima war eine große Bereicherung meiner Zeit in Greifswald. Dazu beigetragen haben anfangs die willkommenen Videoabende, gesponsort von Herrn (inzwischen Dr.) Dreier und der stets zu einem Witzchen aufgelegte Maciej, dem ich auch für Geduld in angeregten Diskussion und erfolgreiche Zusammenarbeit dankbar bin. Auch die stets nervigen und unqualifizierten Zwischenfrage von Herrn Dr.  $\frac{N}{W}er\frac{v}{n}$ er ließen nichts unversucht um die Hölle des Alltags aufs höchste unerträglich zu gestalten. Vielen Dank dafür. Die interessant exzessiven Abende mit der Vine-taggruppe haben leider im Laufe der Zeit etwas Seltenheitswert gewonnen, aber liefern Anlass für einige kopfschüttelnd mit schmerzverzerrtem Gesicht gedachte Erinnerungen, danke Crishy. Mein besonderer Dank gilt auch dem verzottelten Yeti für stete Bemühungen um die Hochhaltung der Moral auf dem sinkenden Schiff, und dem Sicherheitsfanatiker meines Vertrauens, dem ein Kaffemaschinen-verursachter Brand im Brandschutzbeauftragtenbüro gerade noch erspart blieb. Die Liste mit Themen, die bei einem Bier zu diskutieren wären (warum sind eigentlich in dem Laden alle Abstinenzler?) muss später mit dem Peter abgearbeitet werden, vielen Dank für physikalisch stimulierende Diskussionen bis hierhin. Frank, dem Elektro-niker gilt mein Dank für technische Dokumentation und partytechnische Inspiration. Auch nicht vergessen werden soll der Torsten, der Autoflüsterer, dessen Nase was Nepumuk anging doch nicht getrogen hat, vielen Dank für diese Hilfe!

Für warmherzige Aufnahme danke ich meinen verschiedenen Mitbewohnern und Mitbewohnerinnen, für herzliche Willkommensflüche schon an der Tür dem Lutz, für leckere Kochabende der Anne, für Surfträumereien dem Seb, für Hilfe aus der Verlegenheit und leckere Nudeln dem Stefan und der Dani und für Musik die das Herz bewegt, tiefsinnige Gespräche und anderes der Anne-Marie. Nicht unerwähnt bleiben dürfen auch meine persönlichen Windberater Moritz, charming Dave, Olaf, und insbesondere mein eisenbeißender surf-instructor Manu, der mir keine Zimperlichkeit durchgehen ließ, ich hoffe wir rippen bald die Welle in Südafrika (Moritz!): life begins at 30 knots! Weitere Quellen der Freude assoziiere ich mit meinem Radkraftsportler-Kumpel Richard, mit dem dreimaliger Kickerturnier-Sieger zu werden ich die Ehre hatte, der alten Bockwurst, und dem guten Jon Hansen, mit dem mal immer wieder bei einem Hauptstadtbier die Lage analysieren konnte. Der Jule danke ich für Einladungen zu wundervollen geselligen Runden mit leckerem Essen. Eine schöne Zeit verbinde ich auch mit Mietze und ihrem Moppel, Dumm und immer in Aktion werd ich nicht vergessen. Danke dafür und alles Gute.



### **Eidesstattliche Erklärung**

Hiermit erkläre ich, daß diese Arbeit bisher von mir weder an der Mathematisch-Naturwissenschaftlichen Fakultät der Ernst-Moritz-Arndt-Universität Greifswald noch einer anderen wissenschaftlichen Einrichtung zum Zwecke der Promotion eingereicht wurde. Ferner erkläre ich, daß ich diese Arbeit selbständig verfaßt und keine anderen als die darin angegebenen Hilfsmittel benutzt habe.

---

(Dirk Dodt)